Ph. D. Dissertation

Study on topological insulator BiSb and CoFeB with perpendicular magnetic anisotropy for spin-orbit torque magnetoresistive random access memory

Zhang Ruixian

Thesis supervisor

Professor Pham Nam Hai

Department of Electrical and Electronic Engineering
School of Engineering

Institute of Science Tokyo

December 2025

Thesis Defense Committee:

Professor Pham Nam Hai (Chair)

(Department of Electrical and Electronic Engineering, Institute of Science Tokyo)

Professor Shigeki Nakagawa

(Department of Electrical and Electronic Engineering, Institute of Science Tokyo)

Professor Takaaki Manaka

(Department of Electrical and Electronic Engineering, Institute of Science Tokyo)

Professor Akira Yamada

(Department of Electrical and Electronic Engineering, Institute of Science Tokyo)

Associate Professor Shinsuke Miyajima

(Department of Electrical and Electronic Engineering, Institute of Science Tokyo)

Professor Shinobu Ohya

(Department of Electrical Engineering and Information Systems, The University of Tokyo)

Copyright 2025 by Zhang Ruixian

ABSTRACT

In this dissertation, we demonstrate 2 researches around the prerequisite technology of SOT-MRAM:

1. Integrate high performance BiSb topological insulator and perpendicularly magnetized CoFeB/MgO heterostructure to realize ultralow power SOT-MRAM in the future.

2. Improving the PMA of CoFeB after 400°C annealing, for further scaling beyond the 16 nm CMOS process.

Basing on the two results from this study, it is possible to realize the thermal-robust SOT-MRAM with low switching current and scalability in the future.

In Chapter 1, we overview the evolution of computing technology alongside the advent of memory technologies. We then discuss why STT-MRAM is insufficient to reduce the switching current and switching time. Then, we introduce the potential of SOT-MRAM as the next-generation MRAM technology.

In Chapter 2, we overview important magnetic properties with focus on magnetic anisotropies. Then, we introduce the spin Hall effect, topological insulator, and BiSb as a conductive topological insulator with a giant spin Hall angle.

In Chapter 3, we introduced the sputtering technique and the Hall bar patterning process for device fabrication in this dissertation. We also explain the second harmonic measurement for evaluating the effective spin Hall angle $\theta_{\mathrm{SH}}^{\mathrm{eff}}$. Then we explain the SQUID, XRR and AES measurements that will be used to characterize the samples.

In Chapter 4, we study the PMA and SOT characteristics in $Bi_{0.85}Sb_{0.15}$ (001) (10 nm)/Ru(Ti) (1∼4 nm)/Ta (0.8 nm)/$Co_{20}Fe_{60}B_{20}$ (1 nm)/MgO (2.5 nm)/Ta (1 nm) deposited by magnetron sputtering on c-plane sapphire substrates. We show that the highest $\theta_{\mathrm{SH}}^{\mathrm{eff}}$ is obtained when Ru(Ti) buffer layer thickness is 3 nm. Furthermore, by depositing BiSb with a low power, we achieved $\theta_{\mathrm{SH}}^{\mathrm{eff}} = 6.0 \pm 0.1$, which is higher than that of MBE-grown $(BiSb)_2Te_3$. We then demonstrated the full SOT magnetization switching with a small zero Kelvin threshold switching current density of $1.5 \times 10^6\ \mathrm{A \cdot cm^{-2}}$.

In Chapter 5, by using B-rich $Co_{19}Fe_{56}B_{25}$ in $Mo/CoFeB/MgAl_2O_4$, we realize giant PMA with H_k of $17.5 \sim 19.5$ kOe, and K_{eff} of $6.9 \times 10^6 \sim 9.4 \times 10^6$ $erg \cdot cm^{-3}$. We also demonstrate double CoFeB layers with giant PMA for use in more advanced CMOS process.

In Chapter 6, we conclude this thesis.

List of Abbreviations (in chronological order)

Abbreviation	Description
CPU	center processing unit
LLC	last-level cache
RAM	random access memory
SRAM	static random access memory
DRAM	dynamic random access memory
CMOS	Complementary Metal-Oxide-Semiconductor
WL	wordline
BL	bitline
AI	artificial intelligence
HDD	hard disk drive
SSD	solid state drive
GMR	giant magnetoresistance
NM	non-magnetic
FM	ferromagnetic
CPP	current-perpendicular-to-plane
TMR	tunnel magnetoresistance
MTJ	magnetic tunnel junction
MRAM	magnetoresistive random access memory
AFM	anti-ferromagnetic
STT	spin transfer torque
SNR	signal-to-noise ratio
SOT	spin orbit torque
SHE	spin Hall effect
ISHE	Inverse spin Hall effect
SHA	spin Hall angle

SEM	scanning electron microscopy
HM	heavy metal
SOC	spin-orbit coupling
SOI	spin-orbit interaction
TI	topological insulator
REE	Rashba-Edelstein effect
AHE	anomalous Hall effect
PMA	perpendicular magnetic anisotropy
TSS	topological surface state
TRS	time-reversal symmetry
MBE	molecular beam epitaxy
BEOL	back-end-of-line
RP	rotary pump
TMP	turbo-molecular pump
GV	gate valve
DC	direct current
RF	radio frequency
XRD	X-ray diffraction
XRR	X-ray reflectivity
SQUID	superconducting quantum interference device
TEM	transmission electron microscopy
IMA	in-plane magnetic anisotropy
AC	alternating current
ONE	ordinary Nernst effect
ANE	anomalous Nernst effect
SSE	spin Seebeck effect
p-MTJ	perpendicular magnetic anisotropy magnetic tunnel juntion
FWHM	full width at half maximum

List of Symbol

Symbol	Description
$\hbar$	reduced Planck constant
k_{B}	Boltzmann constant
μ_{B}	Bohr magneton
g	Landé g factor
e	electron charge
μ_0	the vacuum permittivity
α	damping constant
γ	gyromagnetic constant
v_{F}	Fermi velocity
$\vec{s}$	spin polarity vector
P	spin polarization
M_{s}	saturation magnetization
V_{X}	volume of X layer
w_{X}	width for X layer
t_{X}	thickness for X layer
J_{X}	charge current density for X layer
ρ_{X}	resistivity for X layer
σ_{X}	conductivity for X layer
$R_{\mathrm{sheet}}^{\mathrm{BiSb}}$	BiSb sheet resistance
$t_{\mathrm{surface}}^{\mathrm{BiSb}}$	BiSb surface state thickness
$J_{\mathrm{th}}^{\mathrm{BiSb}}$	threshold current density for BiSb layer
$\sigma_{\mathrm{bulk}}^{\mathrm{BiSb}}$	bulk states conductivity of BiSb
$\sigma_{\mathrm{surface}}^{\mathrm{BiSb}}$	surface states conductivity of BiSb
$J_{\mathrm{th}}^{\mathrm{BiSb}}\big\rvert_0$	threshold current density for BiSb layer at 0 K
E_{g}	band gap

Δ	thermal stability factor
$1/\tau_{\mathrm{D}}$	attempt switching frequency
$t_{\mathrm{retention}}$	bit retention
f	bandwidth
T	temperature
λ_{sf}	spin diffusion length
H_{bias}	the bias field from the magnetic bias layer
c	the amplifier noise constant
θ_{SH}	spin Hall angle
σ_{SH}	spin Hall conductivity
$R_{\mathrm{H}}^{1\omega}$	first harmonic Hall resistance
$R_{\mathrm{H}}^{2\omega}$	second harmonic Hall resistance
$V_{\mathrm{H}}^{1\omega}$	first harmonic Hall voltage
$V_{\mathrm{H}}^{2\omega}$	second harmonic Hall voltage
R_{ISH}	inverse spin Hall resistance
V_{ISH}	inverse spin Hall voltage
R_{AHE}	anomalous Hall resistance
$R_{\mathrm{ANE/SSE}}$	ANE/SSE resistance
R_{ONE}	ONE resistance
H_{z}	out-of-plane external magnetic field
H_{x}	in-plane external magnetic field
H_{k}	effective magnetic anisotropy field
H_{AD}	damping-like SOT effective field
I	bias current
I_{s}	spin current
J	bias current density
J_{s}	spin current density

Contents

Abstract **2**

List of Abbreviations **4**

List of Symbol **6**

Table of Contents **8**

1 Introduction to Memory Technologies **11**

1.1 The Von-Neumann Architecture 12
1.2 Present Memory Technologies 14
1.2.1 Static Random Access Memory 16
1.2.2 Dynamic Random Access Memory 18
1.2.3 NAND Flash 22
1.2.4 Hard Disk Drive 24
1.3 Technological Development of MRAM 28
1.3.1 Giant Magnetoresistance 28
1.3.2 Tunneling Magnetoresistance 30
1.3.3 Spin Transfer Torque MRAM 32
1.3.4 Spin Orbit Torque MRAM 36
1.4 Research Motivations and Objectives 38

2 Fundamental physics for next generation MRAM **41**

2.1 Basic Magnetic Phenomenons and Properties in MRAM 41
2.1.1 Ferromagnet and Antiferromagnet 42
2.1.2 Demagnetizing Field and Shape Magnetic Anisotropy . . 43
2.1.3 Magnetocrystalline Anisotropy and Interface Magnetic Anisotropy 45

2.1.4 Interlayer Exchange Coupling and Synthetic Antiferromagnetic Structure . . . 47
2.1.5 Thermal Stability Factor, Relationship between Magnetic anisotropic energy and Retention time . . . 49
2.2 Spin Hall effect . . . 53
2.2.1 Topological Insulator . . . 57
2.2.2 The Conductive Topological Insulator BiSb . . . 59

3 Chapter 3: Sample preparation and characterization techniques 61
3.1 Sample preparation . . . 61
3.1.1 Magnetron sputter . . . 61
3.1.2 Hallbar fabrication process . . . 63
3.2 Magnetization measurement . . . 64
3.3 Characterization techniques . . . 68
3.3.1 X-ray reflectivity . . . 68
3.3.2 Auger electron spectroscopy . . . 71

4 High spin Hall angle in BiSb topological insulator and perpendicularly magnetized CoFeB/MgO multilayers with metallic interfacial layers 75
4.1 Introduction . . . 75
4.2 Sample preparation . . . 77
4.3 PMA and Effective Spin Hall Angle $\theta_{\mathrm{SH}}^{\mathrm{eff}}$ Evaluation . . . 78
4.4 SOT Switching Evaluation . . . 79
4.5 Conclusion . . . 82

5 Giant perpendicular magnetic anisotropy in Mo/Boron-rich CoFeB/$MgAl_2O_4$ structure 91
5.1 Background . . . 91
5.1.1 Quantification of Magnetic anisotropy . . . 91
5.1.2 Motivation . . . 93
5.2 Film Stacks Deposition and Strategy for PMA enhancement . . 94
5.3 PMA Evaluation . . . 95
5.4 Auger Electron Spectroscopy (AES) Evaluation . . . 97

5.5 Discussion 100
5.6 Conclusion 100

6 Conclusions **111**

Bibliography **113**

List of publication **134**

Acknowledgements **139**

Chapter 1

Introduction to Memory Technologies

As a next-generation form of Random Access Memory (RAM), magnetoresistive random access memory (MRAM) underpins advancements in consumer electronics and the broader digital infrastructure.The global MRAM Market size is estimated at USD 3.26 billion in 2025, and is expected to reach USD 27.31 billion by 2030, at a compound annual growth rate (CAGR) of 36.5% during the forecast period (2025-2030)[1] as shown at the Fig. 1.1 for the U.S. market, and other countries like Japan and China are also heavily invested in the MRAM sector, driven by strong technological expertise. The successful deployment of MRAM creates new investment opportunities and reinforces a robust electronics industry. Samsung, TSMC, and GlobalFoundries have increased their production of embedded MRAM (eMRAM) technologies. In 2024, Samsung is broadening its eMRAM use cases to include automotive, wearable devices, graphic memory, and edge AI applications. These foundries are actively working on advanced process nodes, with GlobalFoundries concentrating on 12 nm technology and TSMC providing 22 nm eMRAM as an alternative to embedded flash memory. The development of the manufacturing ecosystem has played a key role in meeting the rising need for high-performance, energy-efficient semiconductor memory solutions.

For better understanding the positioning of MRAM as a very important part of memory hierarchy, it is necessary to introduce its background: the world of storage and computing architecture's history, operating principle and

development trend before detailing MRAM itself.

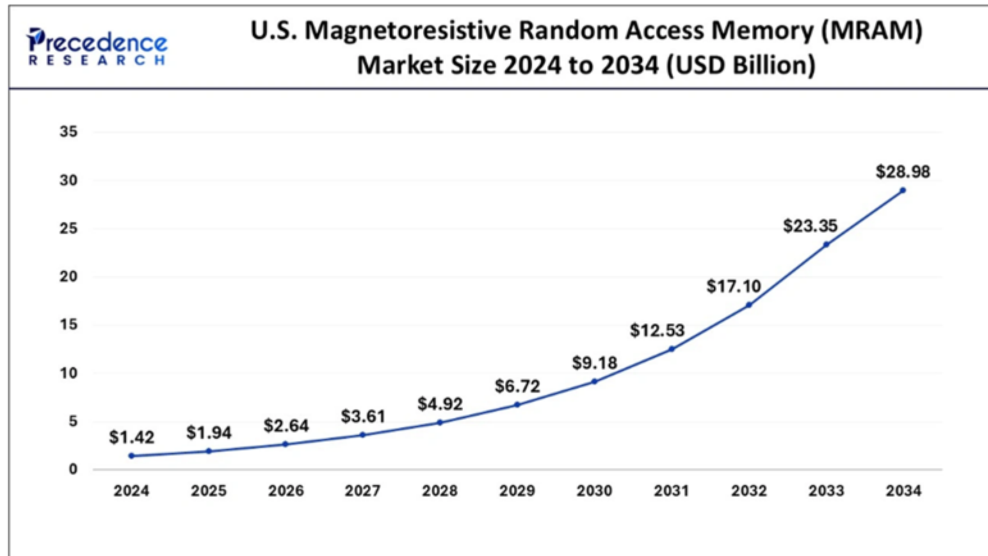

Figure 1.1: CAGR of MRAM Market size for the U.S., Source: Precedence Research

1.1 The Von-Neumann Architecture

The history of storage and computing hardware spans a development from simple calculating tools to today's sophisticated systems. At the core of this evolution is the Von-Neumann architecture, which has shaped modern computing.

The Von-Neumann architecture is the foundational computer design where a single processing unit accesses a single, unified memory device. Since its proposal, the Von-Neumann architecture has become the foundation for nearly all modern general-purpose computers, including desktop PCs, laptops, and servers, demonstrating its enduring utility and significance. The architecture, largely conceived by John von Neumann, emerged after World War II as a solution to developing an electronic computer. Its core operating principle is the stored-program concept, meaning that both data and instructions are stored in the same memory and accessed in a similar manner. This innovation dramatically simplified programming and hardware design compared to

earlier machines. Von Neumann's ideas were crucial in the design and development of early electronic computers like the Electronic Numerical Integrator and Computer (ENIAC) and its successor, the Electronic Discrete Variable Automatic Computer (EDVAC)[2]. From that, both Von Neumann and Alan Turing viewed the development of the electronic computer as fundamentally a problem in logic, linking computing to theoretical foundations. In this architecture, the computational unit such as center processing unit (CPU) is designed to be physically separating from the memory unit, enabling re-programmable logical and computational operations as shown in Fig. 1.2. So the CPU plays as the sole component responsible for computation, while other components such as memory are dedicated to data storage. The defining feature of the von-Neumann architecture is the stored-program concept, where both instructions and data reside in the same memory space, allowing the CPU to fetch instructions and data from memory for execution, where the control unit (CU) acts as the manager and director of the computer's operations.

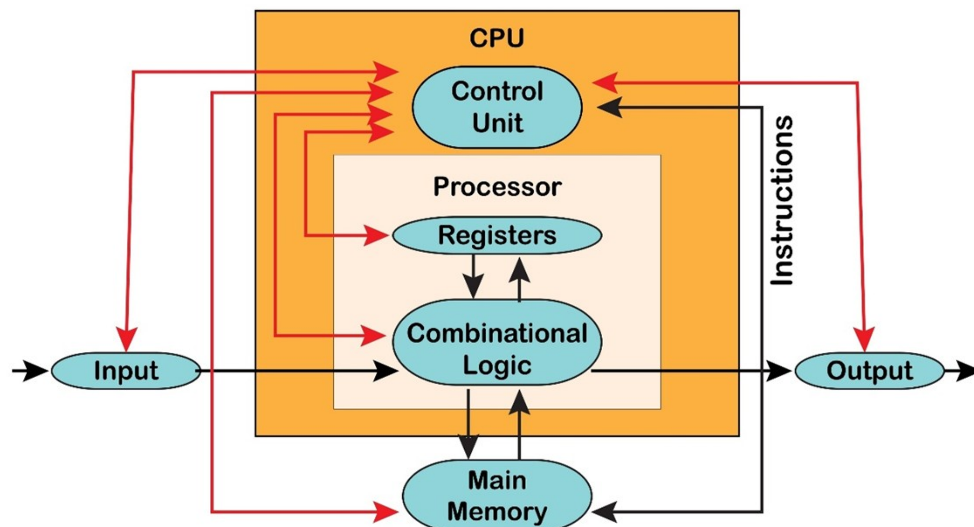

Figure 1.2: von-neumann architecture

1.2 Present Memory Technologies

In the von Neumann architecture, the memory hierarchy is essential to organize memory in a way that reduces access time. Due to its reliability and efficiency, all mainstream memory technologies are part of this von Neumann memory hierarchy. This hierarchy was created based on a program behavior called locality of reference, which means that the same or nearby data is likely to be accessed repeatedly. The diagram below illustrates the various levels of the memory hierarchy. In this section, we provide an overview of memory in the von Neumann architecture.

The memory hierarchy helps optimize the computer's available memory. It consists of multiple levels, each differing in size, cost, and other characteristics. Some types of memory, such as cache and main memory, are faster but smaller in size and more expensive, while others offer larger storage capacity but operate more slowly. Data access speeds vary across these memory types, with some providing quicker access and others slower.

This memory hierarchy design is divided into 2 main types: the External Memory or Secondary Memory and the Internal Memory or Primary Memory. External Memory consist of Magnetic Hard Disk Drives (HDD), solid-state drives (SSD), Optical Disks, and Magnetic Tapes. These peripheral storage devices can be accessed by the processor through an I/O Module as shown at the bottom 3 layers of the pyramid in Fig. 1.3. As for the internal Memory, it consists of Main Memory, Cache Memory and CPU registers. They are directly accessible by the processor. They correspond to register, L1 Cache, L2 Cache and Main Memory at the top 4 layers of the pyramid in the Fig. 1.3.

For the details of CPU registers, Cache Memory and Main Memory, they are responsible for tasks at different levels and have a close working relationship in the Internal Memory.

For Registers:

Registers are discrete, ultra-high-speed memory units embedded directly within the Central Processing Unit (CPU). They serve as the pinnacle of the computer's memory hierarchy, designed to temporarily hold the specific data, addresses, and instructions that are currently being executed by the processor.

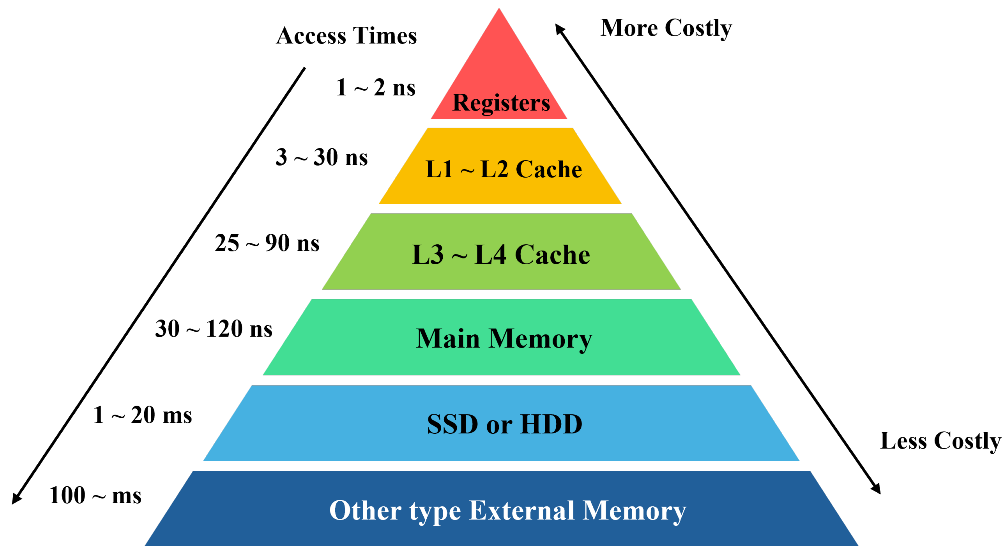

Figure 1.3: Memory hierarchy of Von-Neumann architecture

Because they physically sit on the CPU die, registers offer the fastest possible access times-significantly quicker than cache or main RAM-eliminating latency during critical processing tasks. However, this speed comes with a trade-off in size; registers have a very limited storage capacity, with data widths typically corresponding to the processor's architecture, such as 32-bit or 64-bit (and historically 16-bit) systems.

For Cache Memory:

Cache memory is a small, high-speed memory unit situated near the CPU. It stores data and instructions that are frequently used and have been recently retrieved from the main memory. The purpose of cache memory is to reduce data access time by enabling the CPU to quickly retrieve commonly used information. Cache memory serves two primary functions: it keeps pace with the CPU as it fetches and executes instructions, and it identifies the data stored in the cache line, which loads information from slower memory sources.

Cache memory is typically organized into three levels: on-chip L1 and L2 caches, and off-chip lower-level caches (LLC), such as L3 and L4. The lower the cache level, the slower its speed but the larger its capacity. Larger caches tend to store more relevant data, reducing miss rates, but they operate more slowly compared to smaller caches. The process of retrieving data from cache

memory can be likened to a water fountain, which reduces the average time needed to fetch data. Initially, the system searches for the data in the L1 cache. If it is not found there (a miss), the search proceeds to the L2 cache, then to L3, and finally to the main memory until the required data is found.

For Main Memory:

Main memory, commonly referred to as RAM (Random Access Memory), serves as the primary storage in a computer system. It offers a larger capacity than cache memory but operates at a slower speed. This memory holds the data and instructions that the CPU is actively using. In contrast to cache, which has limited capacity, main memory provides greater storage space, allowing the system to handle multiple processes simultaneously. The versatility of main memory makes it an essential component in the memory hierarchy, balancing the need for both speed and capacity in modern computing. Typically, the size of main memory ranges from several hundred megabytes to several tens of gigabytes.

As for the external memory, it is mainly consisted by HDD and SSD device, and we will introduce them at section 1.3.3 and 1.3.4 later.

In the next part of this section ,we will introduce the present memory technologies with access time from fast to slow.

1.2.1 Static Random Access Memory

Static random-access memory (SRAM) is a form of RAM that stores each bit using latching circuits called flip-flops. Although SRAM is volatile memory-meaning it loses data when power is turned off-it offers very fast access times. A standard SRAM cell typically consists of six metal-oxide-semiconductor field-effect transistors (MOSFETs), commonly referred to as a 6T SRAM cell, as illustrated in Figure 1.4 (a). Within this cell, four transistors (M1, M2, M3, M4) create two cross-coupled inverters that hold each bit, representing binary states 0 and 1. Two additional access transistors manage reading from and writing to the cell. The 6T SRAM design is the most widely used type of SRAM[3].

In contrast, four-transistor SRAM cells are frequently found in standalone

SRAM devices rather than those used in CPU caches. These are fabricated using specialized processes that include an extra polysilicon layer, enabling very high-resistance pull-up resistors, as shown in Figure 1.4 (b). However, a major disadvantage of 4T SRAM is its higher static power consumption, caused by continuous current flow through one of the pull-down transistors (M1 or M2).

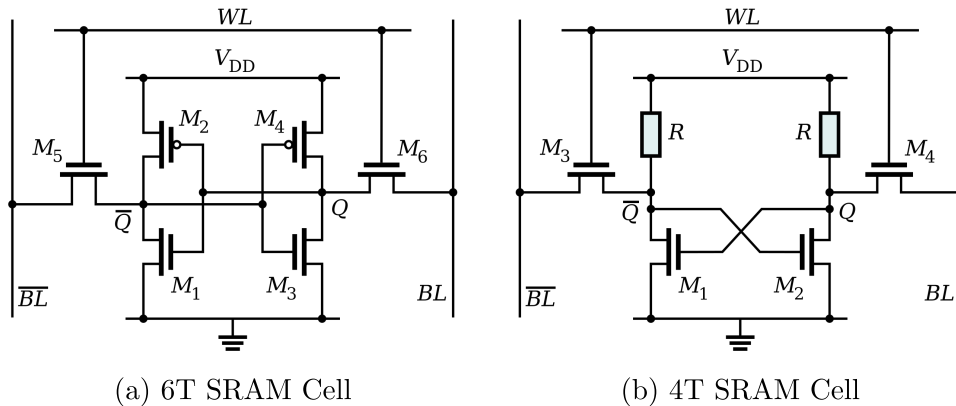

(a) 6T SRAM Cell (b) 4T SRAM Cell

Figure 1.4: 2 kinds of SRAM structure[3][4]. Reprinted, with permission, from IEEE.

To read from and write to 6T SRAM inverters, the wordline (WL) is driven high to activate the gates of transistors M5 and M6, connecting them to the bitline (BL) and its complement $\overline{\text{BL}}$. When idle, the WL is held low, which closes M5 and M6, isolating the cell and preserving its stored data. For reading, both BL and $\overline{\text{BL}}$ are first pre-charged to V_{DD} and then left floating. Next, the decoder raises a specific WL to open M5 and M6, linking the SRAM cells to the bitlines. Depending on the stored value, the activated cells gradually discharge one of the bitlines toward ground. The resulting voltage difference between BL and $\overline{\text{BL}}$ is sensed and amplified by a sense amplifier, which determines whether a 1 or 0 is stored. To write data, the bitline drivers first set BL and $\overline{\text{BL}}$ to the desired logic levels representing 0 or 1. Then, the decoder sets the corresponding WL high to connect the SRAM cell to these bitlines. Because the bitlines have stronger drive capability than the CMOS inverters, they overwrite the cell's current state, flipping the bistable circuit to the new data. Finally, the decoder deactivates the WL, securing the data within the cell. Over years of development, SRAM has achieved latencies on the order of

tens of picoseconds and power consumption in the nanowatt range[5].

1.2.2 Dynamic Random Access Memory

SRAM is used at the highest level of the memory hierarchy as cache memory. It is faster than other types of memory, operates using flip-flops, and does not need to be refreshed. However, it is more costly and occupies more space compared to other memory types. Moving down the hierarchy, Dynamic Random Access Memory (DRAM) uses fewer transistors per cell than SRAM, which is advantageous for bit density. Typically, DRAM consists of a gate transistor and a capacitor (1T+1C) that stores data as an electrical charge, as illustrated in Figure 1.6.

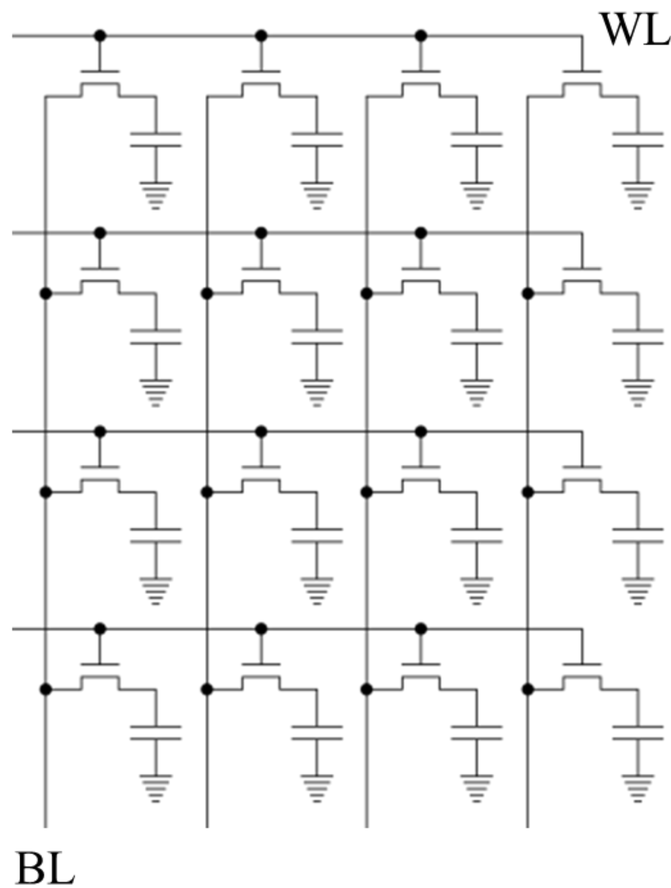

Figure 1.5: A schematic structure of a 4x4 array of 1T+1C-DRAM cells.

To read the data, there are 5 basic steps for DRAM:

1. Activate Row: A memory controller sends a command to activate a specific wordline (row).

2. Connect Cells: Activating the wordline turns on the transistors for that row, connecting all capacitors to their respective bitlines.

3. Sense Data: Sense amplifiers detect the charge on the bitlines, determining if each cell is a '1' (charged) or '0' (discharged).

4. Refresh: The sensed data is immediately written back to the capacitors, restoring their full charge.

5. Deactivate: The wordline is turned off, isolating the cells and completing the read.

To store data, a row is activated and the sense amplifier of a specific column is temporarily driven to the desired high or low voltage level, which causes the bit-line to either charge or discharge the cell's storage capacitor to that level. Because the sense amplifier uses positive feedback, it maintains the bit-line at a stable voltage even after the external voltage is removed. When writing to a particular cell, all columns in the row are sensed at the same time, just like during a read operation. As a result, although only one column's storage capacitor is altered, the entire row is refreshed by being written back.

This functional specialization allows the computer system to keep the most frequently accessed data close to the CPU in the fast, expensive SRAM cache, while the bulk of the program data resides in the larger, cheaper DRAM main memory. Some cache designs even utilize SRAM or eDRAM to implement a cache hierarchy with different regions for low write latency.

For the future development of SRAM, DRAM, and the overall storage structure, there are currently two main approaches to optimizing in terms of energy consumption, performance, and speed called Complementary Field Effect Transistor (CFET) for transistor architecture improving and High Bandwidth Memory (HBM) for memory hierarchy interconnection improving.

Complementary Field Effect Transistor:

As illustrated in Figure 1.5, showing cross-sectional views progressing from FinFET to Gate-All-Around FET (GAAFET), Forksheet, and CFET designs.

The FinFET design was a major leap over planar transistors, but as scaling continued, the GAAFET architecture emerged as a superior solution. GAAFETs, which include Multi-Bridge Channel FET (MBCFET) devices, generally perform better than FinFETs. This improved performance is a result of a device architecture that differs from FinFETs, particularly in how the channel is surrounded by the gate, which impacts leakage mechanisms[6].

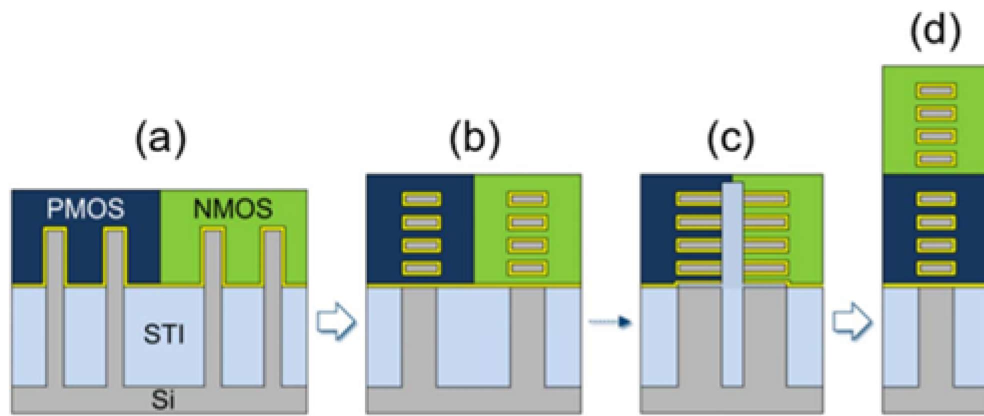

Figure 1.6: Development of MOSFET device designs (cross-sectional perspective). (a) Triple-gate finFETs are being succeeded by (b) GAA vertically stacked lateral nano-sheet FETs, which may further advance into (c) the forksheet design, where adjacent devices are divided by a dielectric barrier. Looking ahead, (d) the vertical stacking of N-type and P-type MOS devices in a CFET structure is currently under investigation as a promising approach for achieving the next level of CMOS miniaturization. Copyright © imec.

Looking ahead to advanced technology nodes, the industry is shifting towards designs that offer even greater density. The Forksheet architecture is seen as an advancement derived from the stacked nanosheet structure, pushing the limits of scaling further. Finally, the CFET developed jointly by TSMC, Intel, Samsung, imec, represents the pinnacle of current scaling strategies. The CFET architecture achieves maximum area efficiency by vertically stacking the pFET and nFET components, building upon the advances made in nanosheet and forksheet devices to be able to achieve 55% higher dense, 7.3% lower power

compared to standard CMOS[7].

High Bandwidth Memory:

As computing races toward higher speeds and greater efficiency, memory bandwidth has emerged as a major bottleneck for workloads like AI, high-performance computing, and data analytics. High Bandwidth Memory (HBM) with 3D stacking of multiple DRAM dies, interconnected by Through-Silicon Vias (TSVs) on a base die, has been designed to operate with significantly higher bandwidth (data transfer rates) than traditional memory solutions like Double Data Rate (DDR).

Instead of laying out all the memory chips side-by-side on a flat board, HBM stacks them like a multi-story building as shown in the Fig. 1.7. This vertical integration, combined with sophisticated electrical connections, creates a superhighway for data, enabling much faster and more efficient communication with the processor.

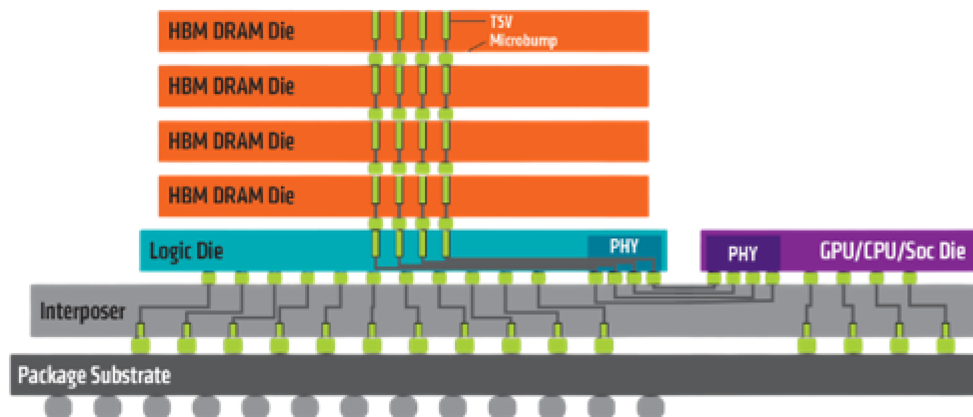

Figure 1.7: A schematic diagram of a HBM architecture. Copyright © PC Perspective.

In Fig. 1.8 and its table, as an example, in terms of bandwidth = Memory Bus Width × Data Rate (Speed), HBM3 offers tremendous over 3500 GBps which is several times faster than other type DRAM, because of the huge Memory Bus Width = # I/F × I/F Width constructed physically by TSVs. Now HBM technology is still moving forward by simply increasing the bandwidth with more advanced TSVs technology[8].

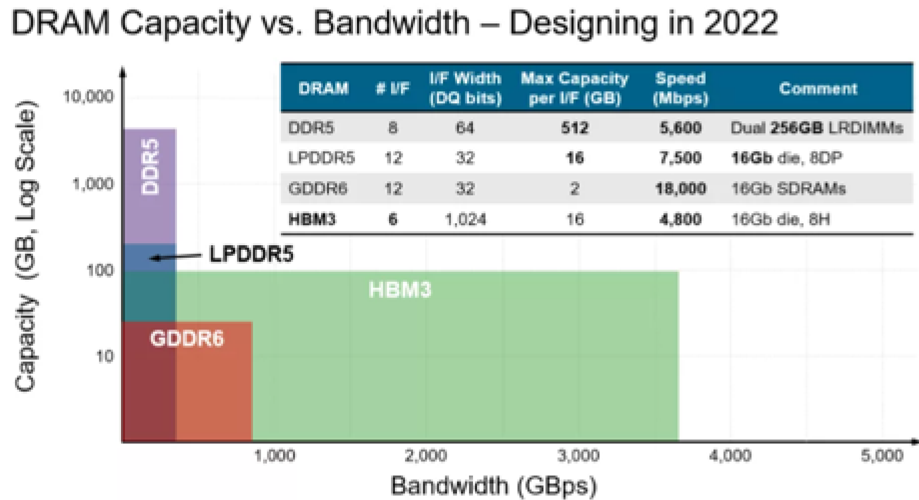

DRAM	# I/F	I/F Width (DQ bits)	Max Capacity per I/F (GB)	Speed (Mbps)	Comment
DDR5	8	64	512	5,600	Dual 256GB LRDIMMs
LPDDR5	12	32	16	7,500	16Gb die, 8DP
GDDR6	12	32	2	18,000	16Gb SDRAMs
HBM3	6	1,024	16	4,800	16Gb die, 8H

Figure 1.8: Performance comparison of DDR5, LPDDR5, GDDR6 and HBM3. Copyright © Synopsys

In contrast, DDR5, low power DDR5 (LPDDR5) and graphic DDR6 (GDDR6) focuses on large-storage, low power storage and graphic processing region separately as shown at Fig 1.8.

1.2.3 NAND Flash

Below the high access speed, volatile memory which locate at the top half position of the memory hierarchy shown in the Fig. 1.3, like SRAM and DRAM, non-volatile technologies, which can preserve data for a substantial period, dominate the bottom half of the memory hierarchy.

NAND flash is a common type of non-volatile storage. The name "NAND" comes from combining "NOT" and "AND," which refers to the logic gate that shapes the internal design of a NAND cell.

In addition to its high storage capacity and non-volatility, NAND flash memory is known for its fast data transfer rates (4.8 Gbps, KIOXIA/SanDisk NAND, 2025), durability, and low power usage. These features have made NAND flash the ideal storage for mobile devices such as smartphones, digital cameras, gaming consoles, and tablets. NAND also has a large market share in data centers, embedded automotive systems, medical imaging devices, and telecommunications networks.

NAND flash stores data using special components called floating-gate transistors. These transistors are connected in series to form a NAND logic gate, a basic digital circuit that processes binary data (ones and zeros) through "NOT" and "AND" operations.

Each NAND memory cell has two main parts: a control gate and a floating gate, separated by a thin oxide layer. This setup acts like a tiny container that can hold an electrical charge.

Writing data to NAND cells starts by storing an electrical charge on the floating gate through a method known as Fowler-Nordheim tunneling. A high voltage applied on the control gate forces electrons into the floating gate, where they become trapped and represent a binary value. To erase data, the charge is removed, freeing the trapped electrons.

NAND flash is efficient because of its block-based design. Instead of writing or erasing data bit by bit, it handles data in large blocks, making it well-suited for sequential tasks and large storage needs.

Pioneered by KIOXIA/SanDisk in 2007, as the most important milestone, NAND memory was started to evolve from 2D to 3D, which revolutionized storage by stacking memory cells vertically.

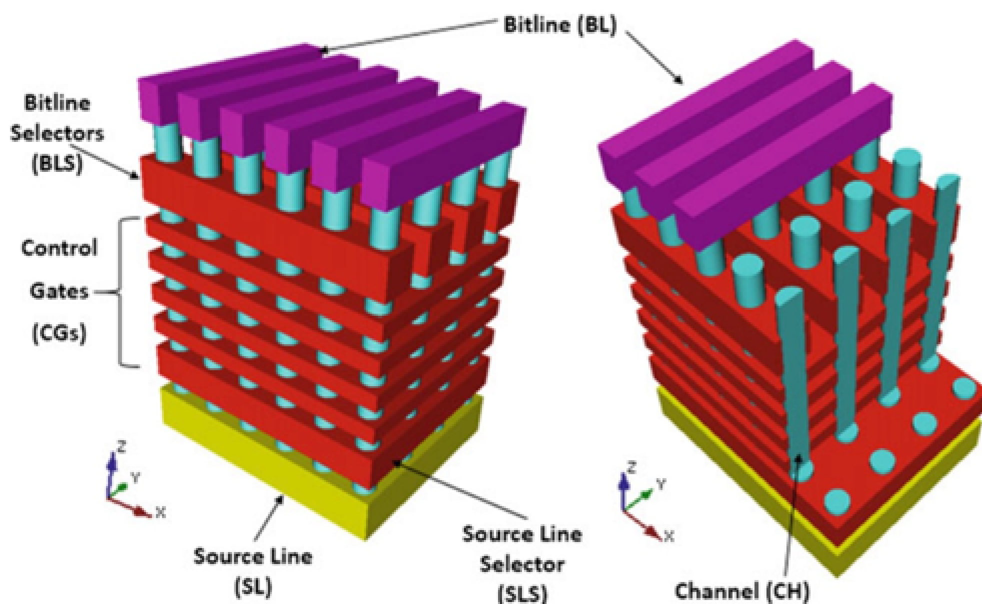

Figure 1.9: A schematic structure of 3D NAND[9]. Images reproduced with permission of the rights holders, Springer Nature.

As shown at Fig. 1.9, manufacturing 3D flash memory devices requires the fabrication of extremely deep holes with high-precision profiles to contain the dielectric material as well as semiconductor. The 3D NAND evolution involves overcoming challenges like deep etching, mechanical stress, and material uniformity, pushing towards 1000+ layers using techniques like high-aspect-ratio etching, new materials (high-k dielectrics), and advanced architectures (horizontal channel flash) to boost density, speed, and efficiency for SSDs and mobile devices. Today, multi-layered structures with 256+ layers is very common as commercial product so that we can enjoy SSDs and USB (universal serial bus) storage with lower price.

For traditional NAND cell, single-level cell (SLC) is utilized to store one bit per cell (2 voltage states). SLC NAND is the most expensive, but it can deliver the highest performance, reliability and endurance. So cheaper choices are Double-Level Cell (DLC) and Triple-Level Cell (TLC, e.g., Samsung 850 EVO) which could stores 2 and 3 bits per cell separately (4 and 8 voltage states, separately). The newest technology that is mass-producted is Quad-Level Cell (QLC) which could Stores 4 bits per cell (16 voltage states), offering more density but lower endurance (e.g., Crucial P1, Samsung 860 QVO).

1.2.4 Hard Disk Drive

A hard drive consists of just a few fundamental components. It includes one or more shiny silver platters where data is magnetically stored, an arm mechanism that moves a tiny device called a read-write head across the platters to read or write data, and an electronic circuit that manages the entire process and connects the hard drive to the rest of the computer, as illustrated in Figure 1.10.

The platters are the most crucial parts of a hard drive. As their name implies, they are disks made from durable materials like glass, ceramic, or aluminum, coated with a thin metal layer that can be magnetized or demagnetized. A small hard drive usually contains just one platter, but both sides of it have magnetic coatings. Larger drives have multiple platters stacked on a central spindle, separated by small gaps. These platters spin at around 10,000 revolutions per minute (rpm), allowing the read-write heads to access any area on them.

Each platter has two read-write heads—one for the top surface and one for the bottom—so a hard drive with five platters, for example, would have ten read-write heads in total. These heads are attached to an electrically controlled arm that moves from the center of the drive to its outer edge and back. To minimize wear, the heads do not physically touch the platters; instead, a thin layer of air or helium gas separates the head from the platter surface.

The key aspect of memory isn't just storing information, but being able to retrieve it later. We can imagine searching a magnetized iron nail among 1.6 million million identical nails to understand the challenge a computer would face without a highly organized system for managing its data.

When a computer saves data on its hard drive, it doesn't randomly scatter magnetized nails in a box. Instead, the data is arranged in a precise pattern on each disk platter. Data bits are organized along circular paths called tracks, which are further divided into smaller sections known as sectors. A portion of the hard drive keeps a record of which sectors are occupied and which are available. In Windows, this record is called the File Allocation Table (FAT). When new data needs to be saved, the computer consults this map to locate free sectors, then directs the read-write head to the exact spot to store the information. Reading data follows the same process in reverse.

But how does an electronic computer control the mechanical details of a hard drive? This is managed by an interface called a controller—a small circuit that operates the drive's actuators, selects specific tracks for reading and writing, and converts data between the computer's parallel format and the disk's serial format. Controllers can be integrated into the hard drive's own circuit board or be part of the computer's motherboard.

However, the Hard disk drive (HDD) industry has been facing two major and tough challenges from 2010s: the areal density (AD) growth rate has stalled in 2012 when the perpendicular magnetic recording (PMR) reached its limit in so-called superparamagnetism[10] and the rising of SSD which seize huge market share of HDD. However, the industry has broken the AD growth bottleneck by a few new technologies, such as shingled magnetic recording (SMR)[11][12], two dimensional magnetic recording (TDMR)[13], heat-assisted magnetic recording (HAMR)[10]. By equipping these technologies, HDD now could store more than 30 TB in a single desktop-level product.

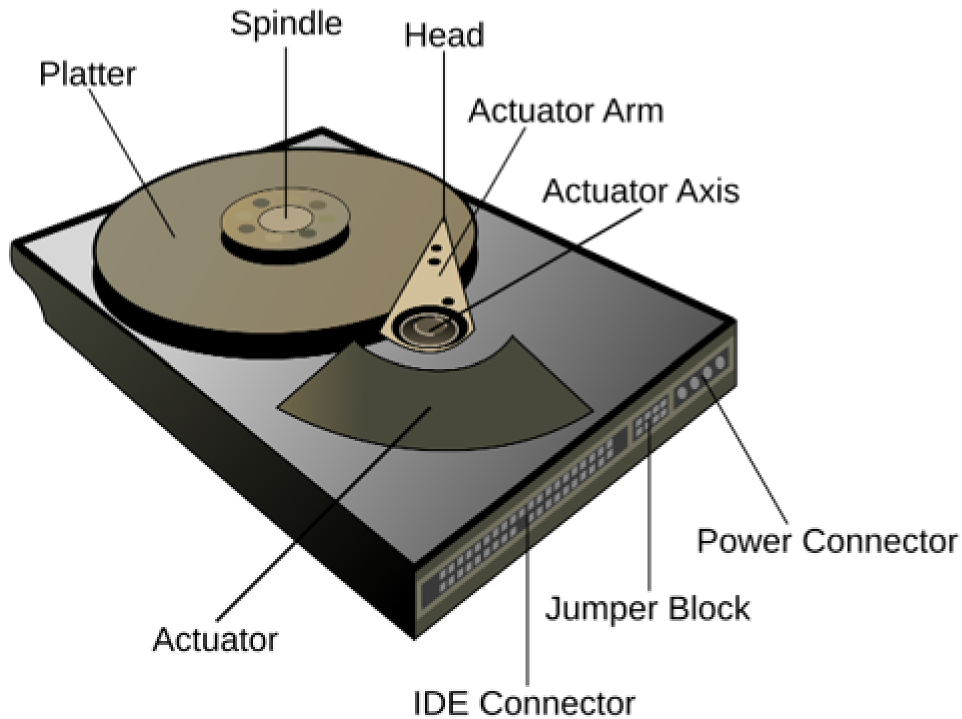

Figure 1.10: A schematic structure of a HDD. Source: Wikipedia.

SMR: This technology is designed to maximize the use of existing PMR head and media technology. In traditional recording methods, data tracks are separated from each other, with gaps left between them to prevent overwriting neighboring tracks during new data writing. Consequently, the spacing between data tracks is determined by the combined width of the writer and the gap. In contrast, SMR intentionally overlaps part of the new data track onto the previous one, resulting in narrower tracks compared to isolated ones. Enhancements in head design are necessary to achieve precise track edge writing and trimming, which are crucial for the effective implementation of SMR.

TDMR: This technology was initially proposed to achieve a areal density (AD) of 10 TB per square inch [14]. As the track pitch and reader width become much smaller, the signal-to-noise ratio (SNR) decreases significantly. When the reader is slightly off-center from the track, the SNR drops to a level where data cannot be reliably read. To enhance the SNR, a multiple-reader array has been suggested. Each pair of individual readers partially overlaps [14], causing the readback data to include information from multiple tracks. To retrieve the desired data from this noisy signal, a two-dimensional digital

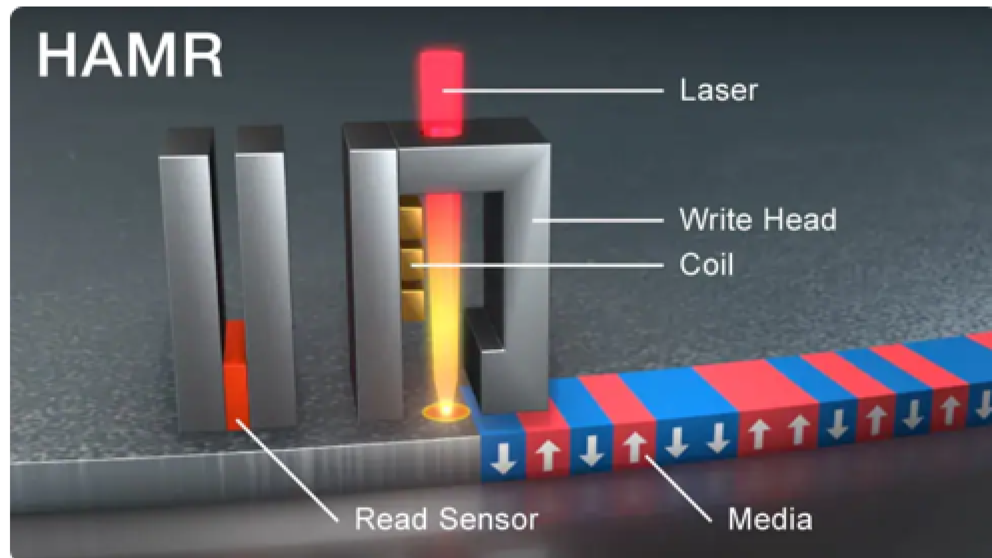

Figure 1.11: Schematic diagram of HAMR structure operating principle. Copyright © TDK.

processing method must be developed. However, recent studies indicate that the capacity improvement from two-dimensional magnetic recording (TDMR) alone is only about 6% [13].

HAMR: This technology is considered the most promising for increasing hard disk drive (HDD) areal density beyond a few terabytes per square inch. Seagate announced plans to release its first HAMR (Heat-Assisted Magnetic Recording) drive around 2017 [15]. To prevent superparamagnetism—where the magnetization of nanoscale magnetic grains flips direction due to temperature effects—the magnetic media is made from materials with high coercivity, which makes it harder for the magnetization to change direction. However, this high coercivity also makes writing data more challenging. The fundamental concept of HAMR involves using a laser beam, delivered through a near-field transducer (NFT), to heat the magnetic grains and temporarily lower their coercivity, thereby easing the writing process, as illustrated in Figure 1.11. Once writing is complete, the media cools down and returns to its high coercivity state, ensuring the recorded data remains stable. The primary challenges facing this technology are the durability of the recording head and the design of the media.

The future of HDD lies in the data center application, where bigger capacity

and low cost are the dominating factors.

1.3 Technological Development of MRAM

1.3.1 Giant Magnetoresistance

GMR refers to the variation in electrical resistance caused by an applied magnetic field. It was found that applying a magnetic field to a Fe/Cr multilayer leads to a notable decrease in the multilayer's electrical resistance. This change in resistance occurs because the magnetic field aligns the magnetic moments of the consecutive ferromagnetic layers, as shown schematically in Figure 1.12. The GMR ratio can be expressed as:

$$\text{GMR ratio} = \frac{R_{\text{AP}} - R_{\text{P}}}{R_{\text{P}}}. \tag{1.1}$$

Without an external magnetic field, the magnetizations of the ferromagnetic layers are oriented antiparallel, causing the resistance to rise to R_{AP}. When a magnetic field is applied, it aligns the magnetic moments and saturates the multilayer's magnetization, resulting in a decrease of the resistance to R_{P}[16].

As illustrated in Figure 1.13, electrical conductivity in FMs can be explained by two mostly independent conduction channels in both CIP-GMR and CPP-GMR configurations. These channels correspond to up-spin and down-spin electrons, which are differentiated based on the orientation of their spins along the quantization axis. In FMs, the likelihood of spin-flip scattering events is generally low compared to scattering events where the spin remains unchanged. This implies that up-spin and down-spin electrons remain separate over long distances, allowing electrical conduction to occur in parallel through the two spin channels, with the equivalent resistance calculated for each channel.

In addition, the scattering rates for electrons with up-spin and down-spin also differ significantly in FMs, regardless of the type of scattering centers involved. This is because the band structure in a ferromagnet is split by exchange interactions, resulting in different densities of states at the Fermi energy for up-spin and down-spin electrons. Since scattering rates are proportional to the

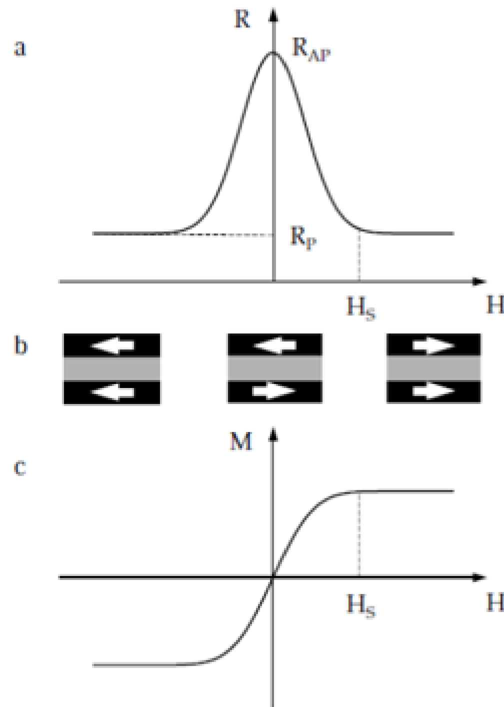

Figure 1.12: Diagram illustrating the Giant Magnetoresistance (GMR) effect. (a): Variation in the resistance of the magnetic multilayer depending on the applied magnetic field. (b): Magnetization arrangements (shown by arrows) within the multilayer (trilayer) under different magnetic field strengths: the magnetizations are antiparallel at zero field; they become parallel when the external magnetic field H exceeds the saturation field H_S. (c): The magnetization curve corresponding to the multilayer. Images reproduced with permission of the rights holders, Elsevier[16]

density of states, the scattering rates—and consequently the resistivities—vary between electrons of different spins.

There are two configurations to assess the resistance of this multilayered structure: one where the current flows parallel to the layers (referred to as current-in-plane GMR, or CIP-GMR), and another where the current flows perpendicular to the layers (called current-perpendicular-to-plane GMR, or CPP-GMR). The same model can be applied to analyze the magnetoresistive behavior in both cases, as long as the thickness of the layers is small relative to a characteristic length specific to each configuration.

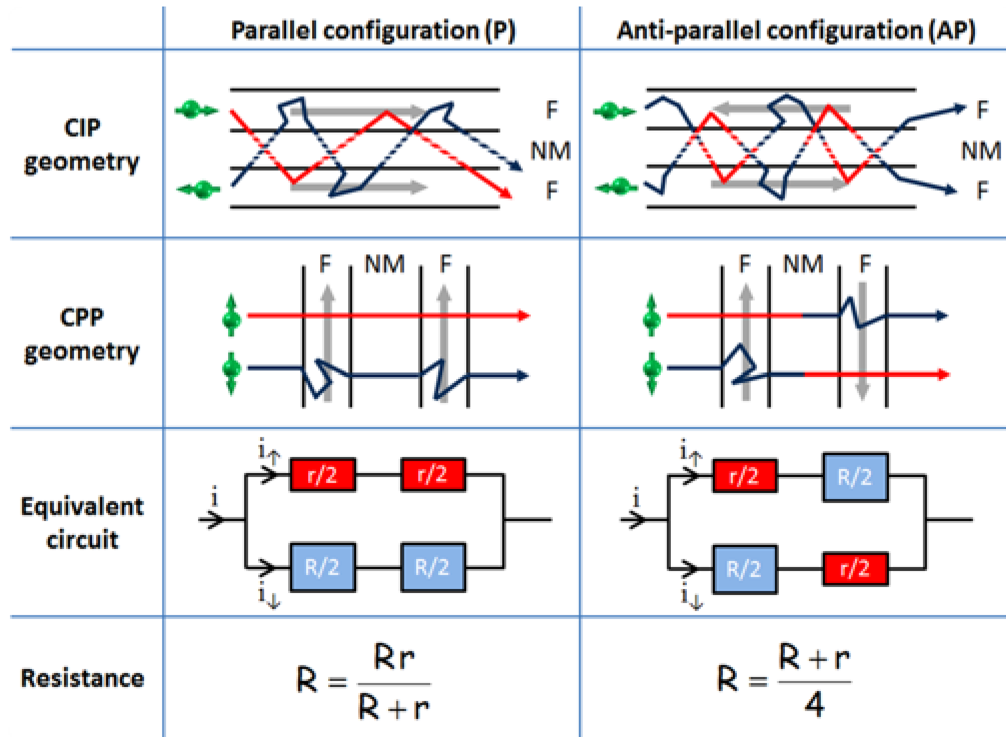

Figure 1.13: Diagram of the two-current model. It shows the conduction routes of spin-up and spin-down electrons in a ferromagnetic metal/normal metal/ferromagnetic metal (F/N/F) multilayer, illustrating both current-in-plane (CIP) and current-perpendicular-to-plane (CPP) transport scenarios. Electrons whose spin magnetic moments are aligned opposite (blue paths) to the local magnetization undergo more scattering compared to those with spins aligned parallel (red paths). The corresponding resistance circuit is depicted for the two magnetic alignments: parallel and antiparallel. Images reproduced with permission of the rights holders, WILEY Online Library[17].

1.3.2 Tunneling Magnetoresistance

Tunnel magnetoresistance (TMR) occurs in heterostructures composed of ferromagnetic and metallic layers separated by a thin insulating layer (Julliere, 1975, reference[18]). The insulating layer serves to decouple the ferromagnetic components, allowing electrons to utilize quantum tunneling to transfer between the magnetic layers. Because of this characteristic, TMR is a purely quantum mechanical phenomenon, distinct from giant magnetoresistance (GMR).

In a trilayer structure made of ferromagnet (FM)/tunnel barrier/FM, a

significant change in resistance has been observed when the magnetization of one ferromagnetic layer (the free FM) is switched between parallel and antiparallel alignment relative to the magnetization of the other ferromagnet (the reference FM).

This effect can be explained by considering the spin polarization P in a ferromagnetic layer, the conservation of spin during tunneling, and the presence of two separate currents corresponding to the two possible electron spin orientations. Spin polarization is defined based on the density of states (D_{S}) at the Fermi energy (E_{F}), where all available electron states are occupied for spin-up and spin-down electrons (relative to the external magnetic field), denoted as $D^{\uparrow}$ and $D^{\downarrow}$, respectively. Differences in these densities of states lead to variations in the conductance of spin-polarized electrons at the Fermi level between the first and second ferromagnets across the barrier, as illustrated schematically in Fig. 1.14 One finds that:

$$P = \frac{D^{\uparrow}(E_{\mathrm{F}}) - D^{\downarrow}(E_{\mathrm{F}})}{D^{\uparrow}(E_{\mathrm{F}}) + D^{\downarrow}(E_{\mathrm{F}})}. \tag{1.2}$$

where $D^{\uparrow}$ is assumed as majority while $D^{\downarrow}$ is assumed as minority.

$$G_{\mathrm{P}} \propto D_1^{\uparrow}(E_{\mathrm{F}}) \cdot D_2^{\uparrow}(E_{\mathrm{F}}) + D_1^{\downarrow}(E_{\mathrm{F}}) \cdot D_2^{\downarrow}(E_{\mathrm{F}}), \tag{1.3}$$

$$G_{\mathrm{AP}} \propto D_1^{\uparrow}(E_{\mathrm{F}}) \cdot D_2^{\downarrow}(E_{\mathrm{F}}) + D_1^{\downarrow}(E_{\mathrm{F}}) \cdot D_2^{\uparrow}(E_{\mathrm{F}}), \tag{1.4}$$

$$\text{TMR Ratio} = \frac{G_{\mathrm{P}} - G_{\mathrm{AP}}}{G_{\mathrm{AP}}} = \frac{R_{\mathrm{AP}} - R_{\mathrm{P}}}{R_{\mathrm{P}}} = \frac{2P_1P_2}{1 - P_1P_2}. \tag{1.5}$$

where R_{AP} and R_{P} are the resistance and G_{AP} and G_{P} are the conductance measured for ferromagnetic layers with antiparallel and parallel orientation respectively. The application of a voltage to the magnetic layers induce a flow of electrons towards the positive electrode. The total current is the combination of the currents for spin up and spin down electrons, each of them depending on the orientation of magnetization in the layers. As already seen in the case of GMR it is possible to induce change the relative configuration of magnetizations in the magnetic layers and, thus, change the electrical resistance of the device[19].

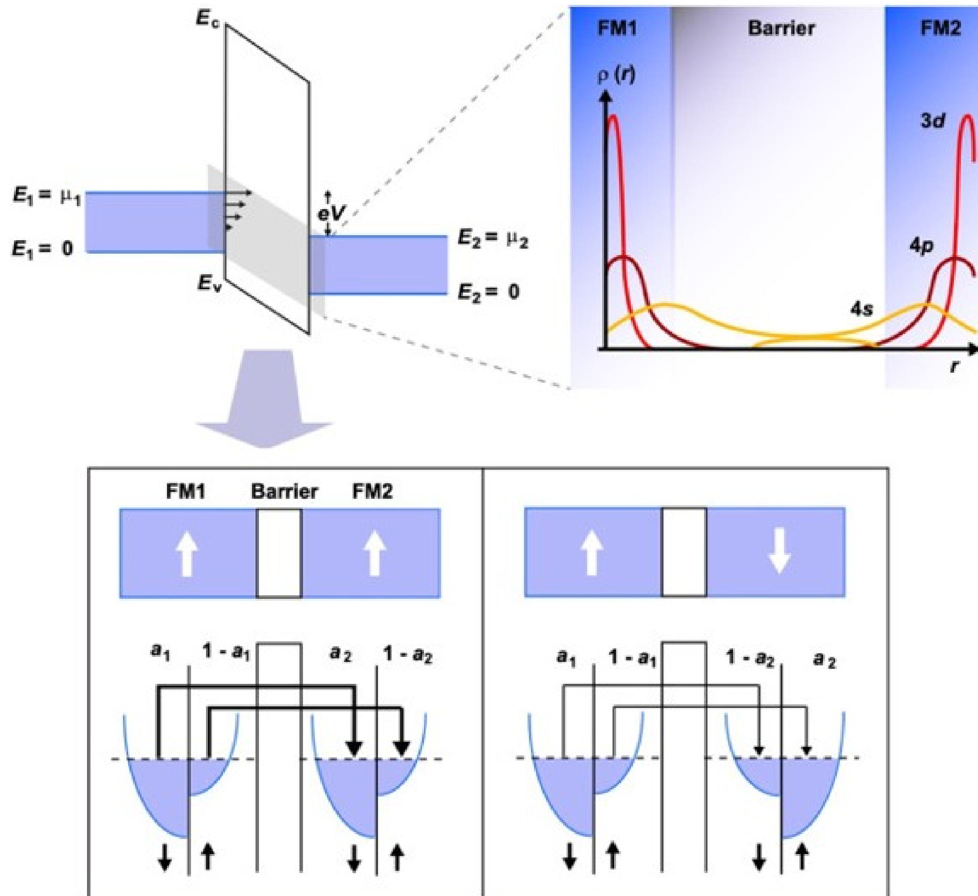

Figure 1.14: Schematic diagram of spin-polarized electron tunneling[20]. Reproduced from Elsevier open source article.

After numerous experiments to surpass the limitations of Jullieres model, a TMR ratio of up to 220% was found in the CoFe/MgO/CoFe junction in 2004[21]. This was possible thanks to the spin-filtering effect of MgO[22, 23]. Until now, the largest room temperature TMR ratio reported in MTJs is 631%[24]. With impressive TMR ratios, spintronic devices such as HDD readers and MRAM have employed the TMR effect to advance their performances.

1.3.3 Spin Transfer Torque MRAM

The history of manipulating the magnetization of magnetic nanostructures by spin-transfer torque (STT) began from the work of Berger's team[25] and Slonczewski's team[26] in 1996. In their research, the resistance changing

behavior after observing current perpendicularly cross the interface of two parallel magnetic films connected by a normal metallic spacer is discussed systematically with the accompanying of vectorial spin transfer during this process for the first time. So it provides a basic framework for the research of the STT effect in GMR, TMR, and spin valve devices. The giant TMR effect observed in MgO-based MTJs is also beneficial for the advancement of STT-MRAM. Typically, MTJs are designed so that one magnetic layer, known as the reference layer, has a fixed magnetization, while the magnetization of the other layer, called the storage layer, can be changed by employing the STT effect[27].

A typical MTJ structure for STT-MRAM is illustrated as Fig. 1.15 (a) and (b), the free layer in MTJ can be switched by STT from polarized tunnel current which cross through tunnel barrier, but the magnetization of reference layer keep in same orientation, so the parallel (low resistance) or antiparallel (high resistance) alignment between free layer and reference layer can be created, corresponding to storing data of '0' or '1'.

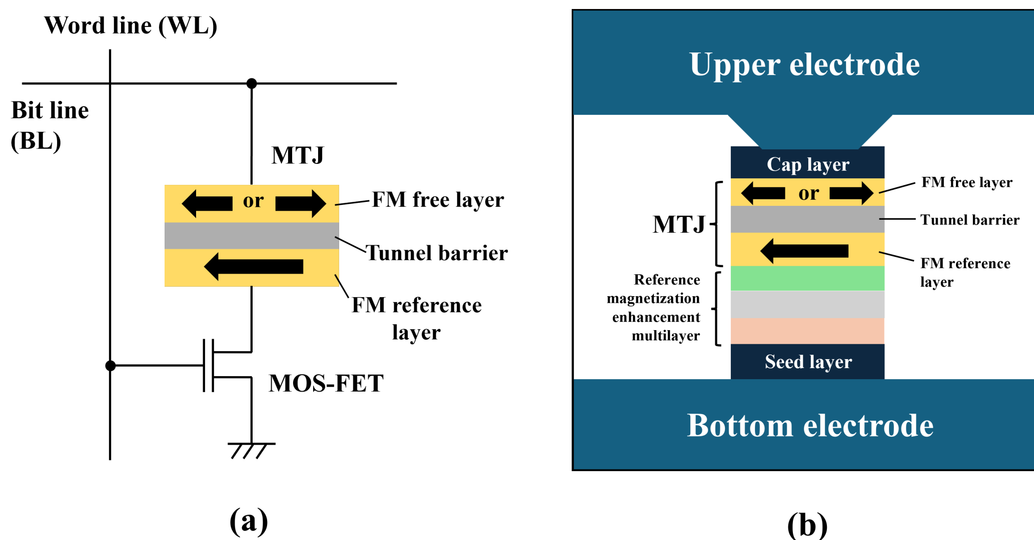

Figure 1.15: (a) Standard circuit diagram of in-plane type STT-MRAM. (b) Common cross-sectional design of a MTJ featuring a spin-valve configuration.

In 2005, Sony Corporation demonstrated a 4-kbit prototype STT-MRAM using CoFeB/MgO/CoFeB MTJs with in-plane magnetization (see Fig. 1.16) and successfully demonstrated reliable writing and reading operations[28]. How-

ever, with MTJs that have in-plane magnetization, achieving high thermal stability—necessary for data retention exceeding 10 years is very challenging when the lateral dimensions of MTJ cells are below approximately 50 nm, which is a common size for gigabit-scale STT-MRAM cells. One way as a commonsense nowadays to overcome this challenge for gigabit-scale STT-MRAM is to employ MTJs with electrodes magnetized perpendicularly (discussed in Chapter 2 and 5). Theoretically speaking, using perpendicularly magnetized electrodes with strong perpendicular magnetic anisotropy allows for both high thermal stability in 50 nm-sized MTJ cells and low write current density. Based on these reasons, after 2017, the mainstream of STT-MRAM with the memory size from 32MB to 1GB is all consisted of perpendicularly magnetized MTJ (pMTJ)[29, 30].

For the MRAM application currently, as the applications for industrial and ioT devices expands, with the integration of Al, higher-speed information processing will be desired for smarter terminal devices to reduce network latency and power consumption. Because the in memory computing capability, as a typical application MRAM can offer sophisticated control and real-time processing, high-processing performance with GHz-class CPU clock frequencies and robust security in the crossover area located on the performance boundary between high-end microcontroller units (MCUs) and low-end microprocessor units (MPUs)[31]. In table 1.1, various types of memories performances are compared including other type of emerging memories, such as PCRAM and ReRAM, STT-MRAM shows advantages such as high endurance and low leakage compared to other memories[32].

Table 1.1: Comparison of performance for SRAM, DRAM, NAND, PCRAM, ReRAM, STT-MRAM

	SRAM	**DRAM**	**NAND**	**PCRAM/ReRAM**	**STT-MRAM**
Architecture	Planar	Discrete 3D	Monolithic 3D	Planar	Planar
Device	6T	1T/1C	1T	1T ‖ 1BJT/1R	1T/1MTJ
Feature Size	7nm	18nm	19nm	20−27nm	40nm
Cell size	40-60F^2	6-8F^2	4F^2	4-6F^2	8-14F^2
Capacity	16Mb	16Gb/Die	1Tb/Die	16Gb	1Gb
Endurance	∞	10^{16}	10^5	10^9	10^{16}
Write energy	8pW/bit/MHz	100fJ/bit	10fJ/bit	5pJ/bit	5pJ/bit
Leakage	1x	0.1x-1x	$\sim$ 0.8x	0.01x	0.01x
Cost	1x	0.1x-1x	0.01x	0.1x	1x

However, the physical limitation of STT-MRAM writing process is due to the low charge to spin conversion efficiency given by

$$I_\mathrm{S} = \frac{\hbar}{2e} P \cdot I_\mathrm{C} \tag{1.6}$$

where the P is the spin polarization, I_C is the charge current, and I_S is the spin current, $\frac{\hbar}{2}$ is the angular momentum for each conduction electron, and e is the electron charge. Considering the finite P can not be larger than 1 (typically between 40 and 80%), the only way for a larger I_S is to increase the I_C which causes serious thermal problem, and tunnel barrier breakdown[33, 34].

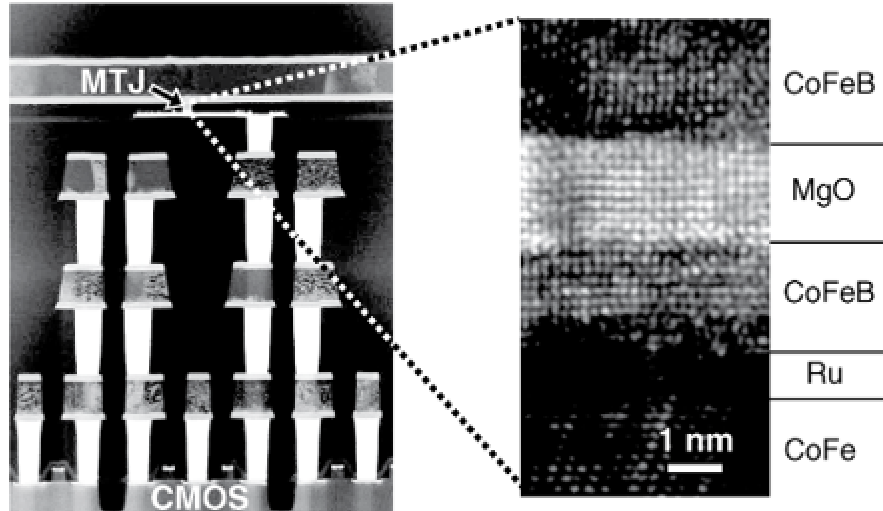

Figure 1.16: Cross-sectional TEM images of 4-kbit STT-MRAM (in-plane type) using CoFeB/MgO/CoFeB MTJs[28]. Courtesy of Sony Corporation, images reproduced with permission of the rights holders, IEEE

Moreover, the read disturb, which is defined as the inadvertent flipping of a bit-cell value during a read operation, constitutes a significant reliability concern of data retention in STT-MRAM because the read pathways need to occupy the write pathway. Specifically, in STT-MRAM, the current used for writing a ‘0’ (parallel, or ‘P’, state) and the read current traverse the same path and flow in the same direction, thereby increasing the risk of read disturb events, so in STT-MRAM, the issue of maintaining a precise ratio between read and write currents is critical to minimizing read disturb rates[35]. For instance, increasing the read current to enhance readability necessitates a

corresponding increase in the write current; failure to do so results in elevated read disturb occurrences. Similarly, reducing the write current to lower write energy consumption requires a proportional decrease in the read current, which adversely affects readability.

Last but not least, both STT-MRAM configurations exhibit a pronounced asymmetry in read and write latencies, as well as in the switching durations between parallel-to-antiparallel (P→AP) and antiparallel-to-parallel (AP→P) states[36, 37].

1.3.4 Spin Orbit Torque MRAM

In Section 1.3.4, we will explain why Spin Orbit Torque MRAM (SOT-MRAM) is more promising than STT-MRAM in a long-term development, based on its superior work principle and advanced SOT source.

Work Principle

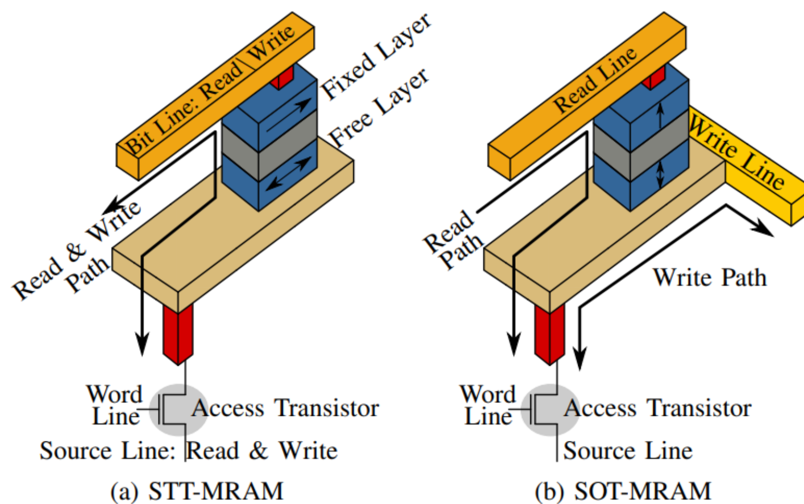

Figure 1.17: Bit-cell write paths and read paths for STT-MRAM and SOT-MRAM[38]. Image reproduced from right holder, IEEE

As shown in Fig. 1.17(a), STT-MRAM has the overlapping write and read paths. In SOT-MRAM, the read path and the write path are separated, as shown in Fig. 1.17(b). Attributing to the distinct separation of read and write

pathways, the read disturb is negligible in SOT-MRAM[39, 40]. SOT-MRAM offers independent optimization for read and write paths, and further enables a balanced co-optimization of readability, access latency, and writing energy efficiency. The write path is consisted of a non-magnetic (NM) material with strong spin-orbit-coupling, which generates a perpendicular pure spin current via the spin Hall effect. Since the pure spin current does not accompany a perpendicular charge current, there is no dielectric breakdown, thus SOT-MRAM has a remarkably high durability ($> 10^{12}$ cycles). Additionally, the write path in SOT-MRAM exhibits significantly lower resistance compared to that in STT-MRAM, where the current must traverse the magnetic tunnel junction (MTJ) cell. Moreover, there is no asymmetry in the writing current and incubation delay in SOT-MRAM during the switching, as SOT-MRAM switching is governed by the spin Hall effect. Conversely, STT-MRAM experiences substantial incubation times that can markedly prolong switching speeds[41]. In contrast, SOT-MRAM can be switched as fast as 300 ps.

Advanced SOT source

As shown in table 1.2, materials with strong spin Hall effect (SHE) arising from their pronounced spin-orbit coupling, including Heavy metals (HMs) such as platinum (Pt), tantalum (Ta), tungsten (W), and topological materials such as BiSb, BiSe and YPtBi. Spin Hall angle θ_{SH} is a critical parameter representing the charge-spin conversion efficiency. One can see in the table that the topological materials have very high spin Hall angle (> 1), 2 order larger than HMs. Meanwhile, in STT-MRAM the charge-spin conversion efficiency is given by the spin polarization P which is lower than 1. The qualitative equation for θ_{SH} is given by Equation 1.7,

$$J_{\mathrm{S}} = \frac{\hbar}{2e}\theta_{\mathrm{SH}} J_{\mathrm{C}} \tag{1.7}$$

$$I_{\mathrm{S}} = \frac{\hbar}{2e}\frac{L}{t}\theta_{\mathrm{SH}} I_{\mathrm{C}} \tag{1.8}$$

where I_{S} represents the spin current, I_{C} represents the charge current, L and t are the spin source length and thickness, respectively, $\hbar$ is the Planck constant, and e is the electron charge.

We can also define a spin Hall conductivity (σ_{SH}), given by Equation 1.9,

$$\sigma_{\mathrm{SH}} = \frac{\hbar}{2e}\theta_{\mathrm{SH}}\sigma \tag{1.9}$$

Because of high θ_{SH}, σ_{SH} of topological material is almost in a same magnitude compared with HMs.

Table 1.2: Performance comparison for topological materials and heavy metals

SOT source	θ_{SH}	$\sigma(\Omega^{-1}m^{-1})$	$\sigma_{\mathrm{SH}}(\frac{\hbar}{2e}\Omega^{-1}m^{-1})$
β-Ta	0.15	5.3×10^5	0.8×10^5
β-W	0.4	4.7×10^5	1.9×10^5
Pt	0.08	4.2×10^6	3.4×10^5
$Bi_{0.9}Sb_{0.1}$	52[42]	2.5×10^5	1.3×10^7
Bi_xSe_{1-x}	18.8[43]	7.8×10^3	1.4×10^5
$Bi_{0.85}Sb_{0.15}$	12.3[44]	1.5×10^5	1.8×10^6
YPtBi	1~7.8[45]	$0.14 \sim 0.4 \times 10^5$	$0.4 \sim 1.5 \times 10^5$

For the physical theories of the SHE and SOT, we would like to introduce them later in Chapter 2.

1.4 Research Motivations and Objectives

We have introduce SOT-MRAM which offers fast operation and high endurance in section 1.3.4. However, the full exploitation of the potential of SOT-MRAM requires addressing 3 main challenges[46].

Firstly, integration of high performance SOT materials such as topological materials and perpendicular magnetic anisotropy (PMA) systems is essential to realize the low switching current and scalability of SOT-MRAM, aligning its development with the progression of CMOS technological nodes.

Secondly, ensuring compatibility with back-end-of-line (BEOL) complementary metal-oxide-semiconductor (CMOS) fabrication processes is vital to facilitate seamless incorporation into existing manufacturing workflows.

Thirdly, the implementation of field-free switching mechanisms is crucial for the practical deployment of SOT-MRAM devices.

For solving the first and second challenges above, this study focuses on 2 main objectives:

1. Integrate high performance BiSb topological insulator and perpendicularly magnetized CoFeB/MgO to realize ultralow power SOT-MRAM in the future.

2. Improving PMA of CoFeB for further scaling beyond the 16 nm CMOS process.

Basing on the two results from this study, it is possible to realize the thermal-robust SOT-MRAM with low switching current and scalability in the future.

Motivation 1

Previous works on sputtered BiSb with high θ_{SH} have been performed in heterostructures with Co or Co/Pt multilayers, which are not the main stream ferromagnetic metal (FM) in p-MTJ. Thus, it is essential to demonstrate high θ_{SH} of BiSb in heterojunctions with perpendicularly magnetized CoFeB/MgO[47], which is now the de facto FM/tunnel barrier for p-MTJ.

In previous works, a maximum θ_{SH} of 2.8 has been realized in BiSb/CrO_x /Ta/CoFeB/MgO[48], which helps reducing the SOT switching current to the level of that of STT. However, higher θ_{SH} is essential to further reduce the SOT switching current to lower than that of STT for the SOT-MRAM integrated with PMA CoFeB.

Objective 1: Integration of BiSb with High θ_{SH} and CoFeB/MgO Multilayers with PMA

In this study, we investigate the spin Hall performance in heterostructures of $Bi_{0.85}Sb_{0.15}$ (10 nm) / interfacial layers / $Co_{20}Fe_{60}B_{20}$/MgO with PMA. While the thick MgO interlayer used in the inverse spin Hall effect measurement (Ref.[49]) is useful for enhancing the spin-polarization of the injected spin-polarized current, MgO is known to strongly suppress diffusion of the pure spin current. Thus, the MgO interlayer is not suitable for SOT-MRAM application. For this reason, we chose to use metallic interlayers in this work. By optimizing the metallic interfacial layer thickness as well as deposition condition of BiSb, we achieve large effective spin Hall angle $\theta_{\mathrm{SH}}^{\mathrm{eff}}$ of 6.0±0.1 and relatively high electrical conductivity $\sigma_{\mathrm{BiSb}} = 1.5\times10^5\ \Omega^{-1}\cdot\mathrm{m}^{-1}$ at room temperature, which are larger than those of the MBE-grown $(BiSb)_2Te_3$ ($\theta_{\mathrm{SH}}^{\mathrm{eff}} =$

2.5 and $\sigma_{BiSb_2Te_3} = 1.8 \times 10^4\ \Omega^{-1} \cdot m^{-1}$[50]. We then demonstrate SOT-induced magnetization switching driven by a small threshold current density $|J_{th}|$ of 1×10^6 A·cm^{-2}. Benchmarking using a bilayer model shows that the writing power consumption of our stack is 2∼3 orders smaller than that of HMs.

Motivation 2

One of the most serious problems for the popular Ta/CoFeB/MgO system is that the PMA is degraded and eventually disappears during 400 °C post-annealing, which is required for back-end-of-line (BEOL) CMOS manufacturing. Stacks of Ta (3 ∼ 10 nm)/CoFeB (0.7 ∼ 1.8 nm)/MgO show degradation of saturation magnetization (M_s) and magnetic anisotropy energy density when the annealing temperature T_{an} is over 250 °C, and PMA is lost when T_{an} is over 350 °C[51, 52, 53, 54, 55]. It was then found that Mo underlayer/CoFeB/MgO could keep PMA after 400 °C annealing and showed an interfacial PMA 20% higher than Ta/CoFeB/MgO[56]. Other examples of underlayers for maintaining PMA at $T_{an} \sim 400$ °C are Hf and Mo/Hf multilayers[57, 58].

Despite intensive studies, the magnetic anisotropy field H_k of a bottom CoFeB/MgO single interface is still about 4 ∼ 6 kOe, and the corresponding magnetic anisotropy energy constant K_{eff} is about $3 \times 10^6 \sim 5 \times 10^6$ erg·cm^{-3}. Therefore, the minimum size of MTJ devices with a single CoFeB layer and a thermal stability factor Δ of at least 60 for 10-year retention is about 29 nm, which can be integrated up to the CMOS process of 16 nm. For further device size scaling and better resistance against thermal and external magnetic field disturbance, it is essential to enhance the PMA of CoFeB.

Objectives 2: PMA for CoFeB after 400°C Annealing

In this study, we aim to realize a giant PMA in Mo (2 nm)/$Co_{19}Fe_{56}B_{25}$ (t_{CoFeB})/$MgAl_2O_4$ (4 nm)/Ta (1 nm). By using the B-rich $Co_{19}Fe_{56}B_{25}$ layer in combination with the Mo underlayer and the spinel $MgAl_2O_4$ (4 nm) oxide layer, we achieve giant PMA in CoFeB, with maximum H_k ranging from 17.5 to 19.5 kOe, and maximum K_{eff} ranging from $6.9 \times 10^6 \sim 9.4 \times 10^6$ erg·cm^{-3}. Our results pave the way for further scaling of MTJs and improved resistance to thermal and external magnetic field disturbances.

Chapter 2

Fundamental physics for next generation MRAM

2.1 Basic Magnetic Phenomenons and Properties in MRAM

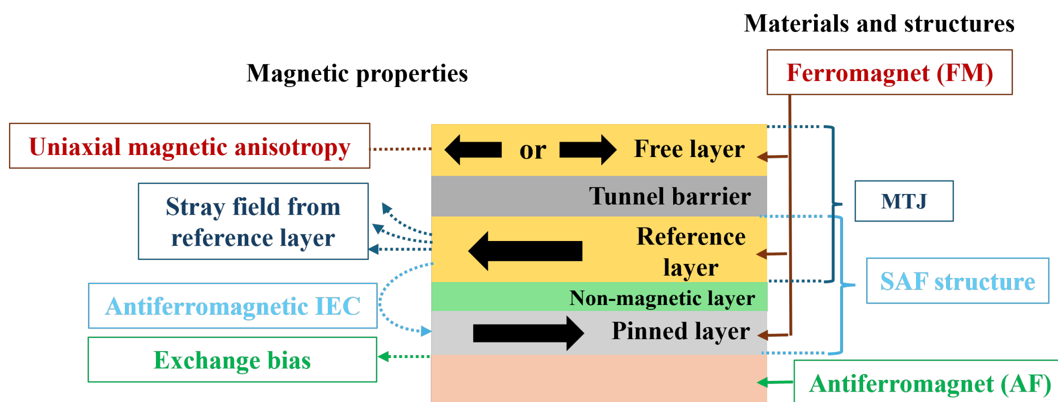

Figure 2.1: Typical stacking structure of MTJ for in-plane magnetized MRAM.

To understand how design a high-performance magnetic junction, it is necessary to overview all the important magnetic properties, materials, and structures in magnetic multilayer. As shown at Fig. 2.1, a typical MTJ stack includes a free layer and a reference layer made by FM, synthetic antiferromagnetic (SAF) structure and antiferromagnet (AF) layer. The free layer is

required to exhibit uniaxial magnetic anisotropy, which may arise from shape anisotropy or magnetocrystalline anisotropy. This anisotropy preferentially aligns the magnetization along a specific direction, referred to as the easy axis. The SAF structure helps to enhance the magnetization orientation and reduce stray field of the reference layer by antiferromagnetic Interlayer Exchange Coupling (IEC) with a pinned layer. By IEC with an AF, which is also called exchange bias, pinned layer's magnetization orientation has been further locked.

In this chapter, we will introduce the magnetic properties that are related to the work in Chapter 4 and 5, that including ferromagnet and antiferromagnet, demagnetizing field and shape magnetic anisotropy, magnetocrystalline anisotropy and interfacial magnetic anisotropy, IEC and SAF structure, thermal stability factor, and the relationship between magnetic anisotropic energy and retention time. Finally, we introduce the spin Hall effect, topological insulator, and BiSb as a conductive topological insulator with a giant spin Hall angle.

2.1.1 Ferromagnet and Antiferromagnet

A ferromagnet is characterized as a material exhibiting spontaneous magnetization, defined as magnetization occurring in the absence of an external magnetic field. Prototypical ferromagnetic materials include iron (Fe), cobalt (Co), and nickel (Ni), which are 3d transition metals, as well as gadolinium (Gd) and dysprosium (Dy), which are rare-earth metals, along with alloys predominantly composed of these ferromagnetic elements. Within a ferromagnetic substance, each atom of the magnetic element carries a localized magnetic moment primarily arising from d or f electrons. Although, strictly speaking, the d electrons in transition metals and their alloys exhibit itinerant behavior and are not strictly localized to individual atoms, the term "localized magnetic moment" is commonly employed for conceptual simplicity. In ferromagnetic materials, these localized moments tend to align parallel to one another due to a quantum mechanical ferromagnetic exchange interaction, resulting in a net magnetization M, defined as the magnetic moment per unit volume. Conversely, in antiferromagnetic materials, the localized magnetic moments of adjacent atoms preferentially align antiparallel as a consequence

of an antiferromagnetic exchange interaction.

When subjected to an external magnetic field exceeding the saturation magnetic field H_{S}, all localized magnetic moments align along the direction of the applied field, forming a single magnetic domain, as depicted in states (i) and (iii) of Figure 2.2. The spontaneous magnetization closely approximates the saturation magnetization M_{S}, thereby allowing M_{S} to represent both spontaneous and saturation magnetizations. For fields below H_{S}, the magnitude of the magnetization $|M|$ can vary continuously between zero and M_{S}, due to the formation of a multidomain state (state (ii) in Figure 2.2) that serves to minimize the magnetostatic energy associated with the demagnetizing field. The magnetization process in ferromagnets is typically accompanied by a hysteresis loop. The magnetic field at which the magnetization becomes zero is termed the coercive force or coercive field H_{c}, while the magnetization remaining at zero applied field is referred to as the remanent magnetization M_{r}. In cases where the hysteresis loop exhibits a square shape, M_{r} approaches M_{S}, indicating that the single domain state achieved at saturation persists even in the absence of an external field. Such a square hysteresis loop is considered ideal for the free layer in magnetic tunnel junctions (MTJs) utilized in magnetoresistive random-access memory (MRAM) applications.

2.1.2 Demagnetizing Field and Shape Magnetic Anisotropy

When the magnetization within a bulk or thin-film ferromagnet is oriented parallel to an external magnetic field (H_{ext}), fictitious yet mathematically defined positive and negative magnetic poles emerge on opposite faces of the ferromagnet. These poles give rise to a demagnetizing field, denoted as H_{d}, which is directed antiparallel to both the magnetization M and the external field H_{ext}. Consequently, the effective magnetic field inside the ferromagnet, H_{eff}, can be represented as $H_{\mathrm{eff}} = H_{\mathrm{ext}} - H_{\mathrm{d}}$. It should be noted that the subsequent analysis holds rigorously only for geometries such as spheres and ellipsoids. In this context, a rectangular thin film is approximated as an ellipsoid with a negligible dimension along the z-axis. A comprehensive treatment of demagnetizing fields is available in the work of Chen et al. [60].

When the magnetization is aligned along the x-axis, the demagnetizing field is given by $H_{\mathrm{d}} = -N_x M$, where N_x denotes the demagnetizing factor

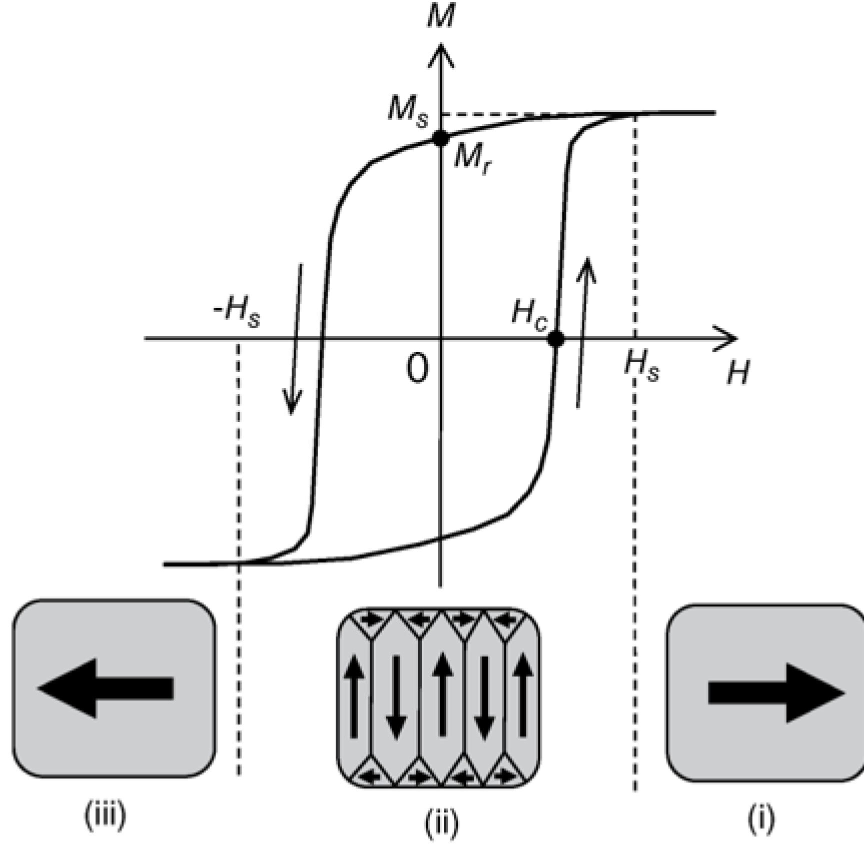

Figure 2.2: Typical magnetization process of a ferromagnet. M_S, H_S, H_c, and M_r respectively denote saturation magnetization, saturation field, coercive force, and remanent magnetization., Wiley Online Library reference[59].

along the x-axis. Similarly, for magnetization oriented along the y-axis and the z-axis, the demagnetizing fields are expressed as $H_\mathrm{d} = -N_y M$ and $H_\mathrm{d} = -N_z M$, respectively. Here, the demagnetizing factors satisfy $0 < N_\alpha < 1$ for $\alpha = x, y, z$, and their sum adheres to the relation $N_x + N_y + N_z = 1$ within the ellipsoidal approximation. In the special case of a spherical ferromagnet, the demagnetizing factors are equal, with $N_x = N_y = N_z = 1/3$. For a thin film situated in the x–y plane, where the lateral dimensions significantly exceed the film thickness, the factors approximate to $N_x \approx N_y \approx 0$ and $N_z = 1$, assuming the absence of other magnetic anisotropies such as interfacial magnetic anisotropy (IMA).

The magnetostatic energy associated with the demagnetizing field, denoted

as E_d, when the magnetization points along the direction α ($\alpha = x, y, z$), is expressed as follows:

$$E_{\mathrm{d}\alpha} = -\mu_0 \cdot M_{\mathrm{S}} \cdot H_{\mathrm{d}a}/2 = \mu_0 \cdot N_\alpha \cdot M_{\mathrm{S}}^2/2. \quad (2.1)$$

The magnetostatic energy is directly proportional to the demagnetizing factor N_α. In the case of a ferromagnetic thin film lacking other forms of magnetic anisotropy, the energy attains its minimum when the magnetization M aligns along a specific axis known as the easy axis, typically corresponding to the plane of the film. Conversely, the energy reaches its maximum when M is oriented along the hard axis, which is generally perpendicular to the film plane.

However, for magnetic nanopillars exhibiting a very high aspect ratio, the easy axis aligns parallel to the thickness direction of the pillar, thereby inducing what is referred to as perpendicular shape anisotropy (PSA) [61].

2.1.3 Magnetocrystalline Anisotropy and Interface Magnetic Anisotropy

When the effective magnetic field, defined as $H_{\mathrm{eff}} = H_{\mathrm{ext}} - H_{\mathrm{d}}$, is employed in the analysis of the magnetization curve (M–H curve), the influence of the sample's shape is effectively eliminated, allowing for the examination of the intrinsic magnetic properties of the ferromagnetic material. In isotropic "soft" ferromagnetic materials, the magnetization readily aligns parallel to the applied field direction, resulting in saturation at relatively low magnetic field strengths. A prototypical example of such a soft ferromagnet is face-centered cubic (fcc) $\mathrm{Ni_{0.81}Fe_{0.19}}$ (Permalloy). When the magnetic energy exhibits dependence on the orientation of the magnetization, this directional dependence is referred to as "magnetic anisotropy." In most typical scenarios, the magnetic anisotropy energy (E_{MA}) can be represented as follows:

$$E_{\mathrm{MA}} = K_{\mathrm{u}} \cdot \sin^2\theta, \quad (2.2)$$

Let θ denote the angle between the magnetization direction and a specific crystallographic axis, referred to as the anisotropy axis. This form of magnetic

anisotropy is termed "uniaxial magnetic anisotropy." When the anisotropy constant K_u is positive ($K_u > 0$), the system's energy attains its minimum at $\theta = 0$, indicating that the magnetization preferentially aligns along this axis, which is identified as the easy axis of magnetization. The magnetization curve measured along the hard axis is characterized by a high saturation field H_s, whereas the magnetization curve along the easy axis exhibits a square-shaped hysteresis loop with a large coercive field H_c.

Magnetic anisotropy arises from various mechanisms. Shape anisotropy plays a significant role in in-plane magnetized magnetic random access memory (MRAM) devices. Conversely, in out-of-plane magnetized MRAM, the predominant sources of anisotropy are magnetocrystalline anisotropy and interfacial magnetic anisotropy.

Magnetocrystalline Anisotropy:

The intrinsic anisotropy of the crystal lattice is typically manifested as magnetocrystalline anisotropy. For lattices exhibiting cubic crystallographic symmetry, the magnetocrystalline anisotropy correspondingly possesses cubic symmetry. In contrast, lattices with uniaxial symmetry-such as body-centered tetragonal (bct), face-centered tetragonal (fct), hexagonal close-packed (hcp), or $L1_0$-type ordered structures-often display uniaxial magnetic anisotropy. Certain $L1_0$-ordered alloys, for example $Fe_{50}Pt_{50}$, are known to exhibit exceptionally high uniaxial magnetic anisotropy with the easy axis oriented along the [001] crystallographic direction [62]. When the easy axis of uniaxial anisotropy in a thin ferromagnetic film is oriented perpendicular to the film plane, this anisotropy is referred to as perpendicular magnetic anisotropy (PMA).

Interfacial Magnetic Anisotropy

In multilayer magnetic structures composed of two or more materials, where at least one constituent is ferromagnetic, the interfaces between these materials can induce magnetic anisotropy, known as interfacial magnetic anisotropy. Certain material combinations produce interfaces that exhibit perpendicular magnetic anisotropy, with the easy axis oriented normal to the plane. Notable examples include Co/Pt, Co/Pd [63], and CoFeB/MgO [64] interfaces, which are recognized for their strong PMA.

Comprehensive physicochemical analyses of CoFeB/MgO, including X-ray absorption spectroscopy (XAS) and X-ray photoemission spectroscopy (XPS), have demonstrated that this interfacial anisotropy originates from chemical bonding between oxygen ions in the oxide layer and transition metal ions at the interface[65, 66]. Subsequent ab initio calculations corroborated that the hybridization between oxygen *sp*-orbitals and the d_{z^2} orbitals of the transition metal (Co or Fe), along with the resulting reduction in degeneracy of the transition metal *d*-orbitals, underpins this anisotropy[67]. Ikeda's team reported that this anisotropy facilitates the fabrication of MgO-based, out-of-plane magnetized magnetic tunnel junctions (MTJs) suitable for spin-transfer-torque magnetic random access memories (STT-MRAM)[47]. These MTJs exhibit large tunneling magnetoresistance (TMR) due to the spin-filtering effect of MgO, combined with low critical switching currents enabled by low Gilbert damping. Indeed, in the development of STT-MRAM technology, out-of-plane magnetized MTJs have demonstrated superior scalability compared to their in-plane magnetized counterparts.

2.1.4 Interlayer Exchange Coupling and Synthetic Antiferromagnetic Structure

When two ferromagnetic (FM) metal layers are separated by a nonmagnetic (NM) metal spacer of nanometer-scale thickness, an exchange interaction between the FM layers frequently arises. This phenomenon is termed interlayer exchange coupling (IEC). The coupling energy can be mathematically described as $E_{\mathrm{IEC}} = -J_{\mathrm{IEC}} \cos\theta$, where θ denotes the angle between the magnetization vectors of the two FM layers, and J_{IEC} represents the exchange coupling constant. A positive value of J_{IEC} ($J_{\mathrm{IEC}} > 0$) corresponds to ferromagnetic IEC, whereas a negative value ($J_{\mathrm{IEC}} < 0$) indicates antiferromagnetic IEC.

In the late 1980s, Grünberg and colleagues identified antiferromagnetic IEC in Fe/Cr/Fe trilayers, demonstrating that this coupling could modulate the relative magnetization orientation of the Fe layers from an antiparallel alignment at zero applied magnetic field to a parallel alignment under a saturating magnetic field. Subsequently, Fert and Grünberg independently ob-

served a significant variation in the sheet resistance of these films associated with the magnetization reorientation. This phenomenon, known as giant magnetoresistance (GMR) and discussed in Chapter 1, catalyzed the emergence of spintronics as a novel branch of electronics.

In 1990, Parkin et al. reported that the IEC exhibits an oscillatory dependence on the thickness of the NM spacer for various FM/NM material combinations[68]. As schematically depicted in Figure 2.3, the IEC typically manifests as a damped oscillatory function of the NM layer thickness[69]. The underlying physical mechanism of IEC is commonly interpreted either as an RKKY-type interaction between the FM layers or as the formation of spin-polarized quantum well states within the NM spacer[70]. Generally, a NM layer thickness exceeding approximately 5 nm is required to effectively decouple the two FM layers. Conversely, at the first antiferromagnetic coupling peak (see Figure 2.3), the IEC attains its maximum strength. For instance, a ruthenium (Ru) spacer combined with cobalt (Co) or Co–Fe alloys exhibits a pronounced antiferromagnetic IEC at the first AF peak, occurring at a Ru thickness of about 0.4 nm. Such strongly antiferromagnetically coupled FM/NM/FM trilayers are referred to as synthetic antiferromagnetic (SAF) structures.

SAF configurations employing Ru spacers serve as fundamental components in magnetic tunnel junctions (MTJs) for device applications, as elaborated in the subsequent section. In the context of magnetic random-access memory (MRAM), the magnetization of the reference layer is stabilized in a fixed direction by the SAF, while the magnetization of the storage layer can be toggled between "up" and "down" states, encoding the binary logic states "0" and "1," respectively. More recently, in 2022, Jinwu Wei and collaborators demonstrated that by depositing a SAF structure composed of Co(2.2 nm)/Ir(0.5 nm)/W(0.4 nm)/Co(2 nm) at the bottom of a MgO/CoFeB/W/CoFeB/MgO stack, an effective equivalent external field (H_{ext}) is generated, enabling field-free spin-orbit torque (SOT) switching[71].

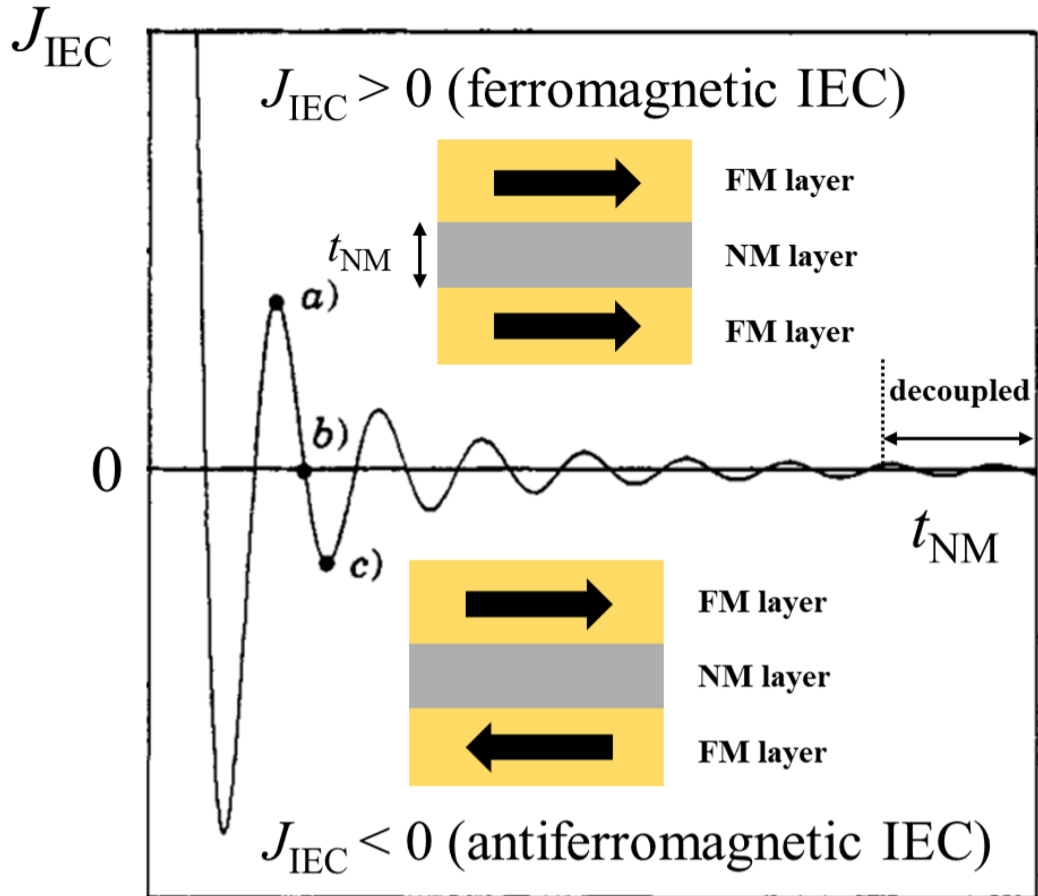

Figure 2.3: Schematic illustration of oscillatory interlayer exchange coupling (IEC)[72], with permission, redrawing from right holder, Europhysics Letters.

2.1.5 Thermal Stability Factor, Relationship between Magnetic anisotropic energy and Retention time

Information storage can be optimized by precisely controlling the orientation of microscopic magnetic domains, commonly referred to as bits. In the context of binary data storage, the magnetic medium used for recording information is engineered to exhibit two stable remanent states. This bistability is achieved through uniaxial magnetic anisotropy, which imposes a preferred direction for the magnetization vector. Consequently, the magnetization can adopt one of two possible orientations along the anisotropy axis. The uniaxial

anisotropy is typically characterized by an anisotropy energy density, denoted as K_u, which quantifies the variation in anisotropy energy as a function of the angle between the magnetization vector $\vec{M}$ and the easy axis of magnetization, represented by the unit vector $\hat{n}$. This relationship is mathematically expressed by the following formula:

$$\mathrm{E} = -K_\mathrm{u} \left(\vec{M} \cdot \hat{n} \right)^2 \tag{2.3}$$

In order to facilitate the enhancement of areal density in granular ferromagnetic recording media composed of ferromagnetic alloy grains, such as CoCrPt utilized in hard disk drives (HDDs) [73], the grain size must be progressively reduced as storage density increases. Taking HDDs as a representative example, at current areal densities of approximately 700 Gbit$\cdot$in^{-2}, the grain size is on the order of 7 nm. Concurrently, the number of grains per bit has diminished over time, decreasing from over 100 in earlier implementations to roughly 10 in contemporary devices. The process of writing information necessitates the reversal of grain magnetization between two stable states by surmounting an energy barrier ΔE that separates these states. The energy required for this transition is expressed as follows:

$$\Delta E = K_\mathrm{u} V \tag{2.4}$$

Here, K_u denotes the anisotropy energy density of the storage layer, and V represents its volume, corresponding to the grain size. The energy barrier ΔE governs the stability of the recorded information. If this barrier is insufficiently high, thermal fluctuations characterized by $k_\mathrm{B}T$ may induce spontaneous reversal of the grain's magnetization, leading to information degradation. The characteristic switching time associated with surmounting the energy barrier follows an Arrhenius-type behavior [63]:

$$\tau = \tau_0 \exp\left(\frac{\Delta E}{k_\mathrm{B}T} \right) \tag{2.5}$$

Here, τ_0 denotes a characteristic attempt time on the order of 1 nanosecond. In order for the information to remain stable over a designated retention period $t_\mathrm{retention}$ (commonly 10 years), the energy barrier is required to satisfy the following condition:

$$\Delta E > k_{\mathrm{B}}T \log\left(\frac{t_{\mathrm{retention}}}{\tau_0}\right), \tag{2.6}$$

$$\Delta E = K_{\mathrm{u}}V > 49k_{\mathrm{B}}T \tag{2.7}$$

Equation (2.7) indicates that, to achieve a retention time of 10 years, the product $K_{\mathrm{u}}V$ must exceed $49k_{\mathrm{B}}T$. Over time, as storage density has increased, the volume of individual grains has necessarily decreased. Consequently, to satisfy the condition $K_{\mathrm{u}}V > 49k_{\mathrm{B}}T$, the magnetic anisotropy constant K_{u} must be proportionally increased. Transitioning from in-plane magnetic anisotropy (IMA) to perpendicular magnetic anisotropy (PMA) mitigates the detrimental effects of demagnetizing energy on the effective anisotropy as the bit dimensions shrink [74].

For the thermal stability calculation of MRAM, data retention also depends on the energy barrier height $K_{\mathrm{u}}V$ similar to the HDD example. Analogous to magnetic recording media, reducing the size of memory cells to enhance storage capacity necessitates an increase in anisotropy to maintain thermal stability. This stability is typically quantified in MRAM by the standby failure rate. For a memory array comprising N bits, the failure rate over a time interval t can be expressed by considering the probability that at least one bit fails during this period. This probability is equal to one minus the probability that no failures occur in any of the N bits within the same timeframe, leading to the following formulation:

$$\mathrm{F}(t) = 1 - \exp(-Nt/\tau) = 1 - \exp\left[\frac{-Nt}{\tau_0}\exp\left(-\frac{\Delta E}{k_{\mathrm{B}}T}\right)\right]. \tag{2.8}$$

For a specified retention time $t = t_{\mathrm{retention}}$ and a given chip capacity, this relationship imposes a lower bound on the thermal stability ratio $\mathit{\Delta} = \frac{\Delta E}{k_{\mathrm{B}}T}$, and consequently on the product K_uV. In magnetic materials, the energy barrier ΔE, which governs the thermal stability factor, is typically established by magnetic anisotropy arising from various sources as discussed in section 2.1.3.

Figure 2.4 illustrates the variation in failure rate over a ten-year period in standby mode (i.e., when no read or write operations are occurring) as a function of the thermal stability factor ($\mathit{\Delta}$) from 1 Kbit to 256 Mbit MRAM

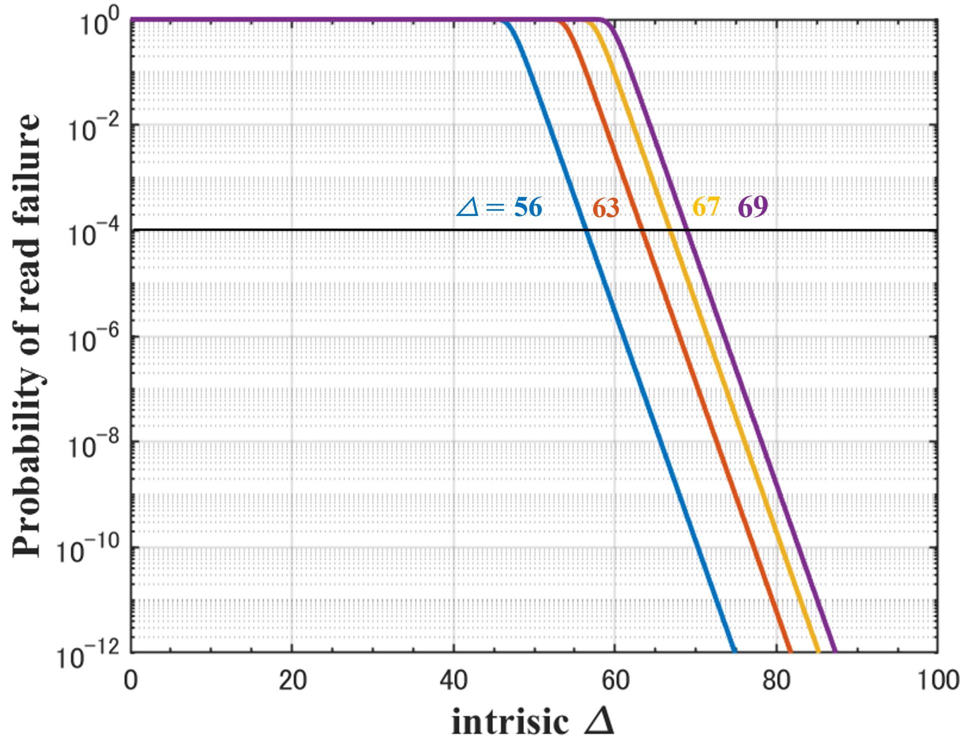

Figure 2.4: Failure rate during 10 years in standby mode for MRAM chips of 1 Kbit, 1 Mbit, 32 Mbit or 256 Mbit as a function of thermal stability factor.

chips. To ensure that the probability of experiencing a single failure within this ten-year timeframe remains below an acceptable threshold of 10^{-4} failures in time (FIT), which is a value that varies depending on whether the application pertains to memory or logic and the potential implementation of error correction codes, the thermal stability factor must exceed 56 for the 1 Kbit chip , 63 for 1 Mbit chip, 67 for the 32 Mbit chip and 69 for 256 Mbit chip.

As the estimation that will be explained in chapter 5, our single FM layer structure A2 and B2 show a suitable Δ at least 60 meeting the typical requirement of (Δ) with $\mathrm{F}(t) < 10^{-4}$ after 10 years data retention. It is expected to satisfy the thermal stability requirement of MRAM with smaller size by designing and stacking double, triple or more FM layers with stronger IEC.

2.2 Spin Hall effect

The generation of spin current is due to the spin Hall effect (SHE), which is a phenomenon that occurs when a spin current source carries a current and spin accumulates on the surface[75, 76]. When spin accumulates, the surface boundaries of the spin current source have spins of the opposite sign. Thus, for example, when electrons with spin-up accumulate to the right and electrons with spin-down accumulate to the left, a spin current flows from right to left. While an electric current carries charge, a spin current carries spin angular momentum. This is a new phenomenon, first theoretically predicted in 2003[75, 76], and then experimentally detected in 2006[77]. It should be noted that spin current, as a non-conserved current, inevitably decays when transported over a micron scale. However, since its application in nanoscale magnetic devices was found to be feasible, it has been widely considered in spin valves[78], magnetic memory devices[79], and specialized devices used to verify electromagnetic properties[80, 81].

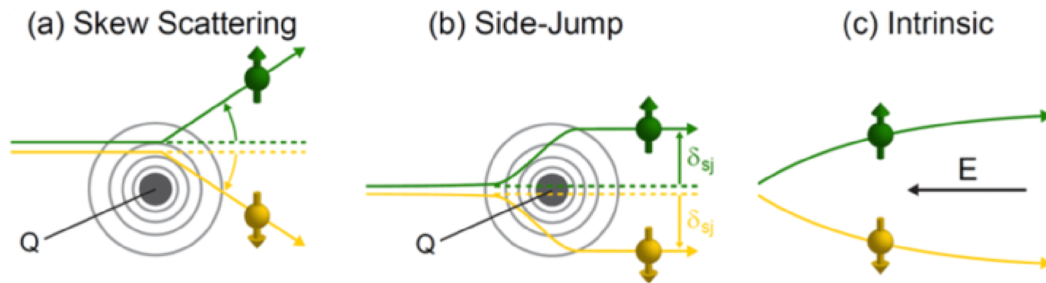

Figure 2.5: Spin-dependent scattering mechanisms responsible for spin Hall effect. (a) Skew scattering, (b) Side-jump scattering, (c) intrinsic interaction[82]. Image reproduced with permission from Diploma thesis of Dr.D. Ruffer.

The "spin Hall effect," which is the origin of spin accumulation and spin current, has been observed in a wide range of materials, including semiconductors, metals, semimetals, and topological insulators, and can be divided into extrinsic and intrinsic. First, the extrinsic spin Hall effect occurs when impurities (including crystalline disorder) are present in a solid, resulting in electron scattering that varies depending on the direction of the electron's spin, due to spin-orbit interactions between the electron and the impurities.

In contrast, the greatest feature of the intrinsic spin Hall effect is that the spin Hall conductivity is largely independent of crystalline disorder or impurities, exhibiting a value that is almost inherent to the material. The spin Hall effect, which can be found in such a wide variety of materials, requires the most appropriate model to be selected depending on the actual situation. For example, two-dimensional semiconductors and topological insulators are described by the Rashba model, while transition metals and transition metal compounds are described by the orbital Aharonov-Bohm model. These models, when mathematically investigated, can be reduced to Berry curvature, an effective magnetic field in wave number space, and are proposed within the framework of gauge theory. Berry curvature is the phase that the wave function acquires when the parameters of a system change adiabatically and then return to their original state[83].

Topological Surface State and Intrinsic Spin Hall Effect

The "topological surface state," an electronic state formed on the surface of a topological insulator, is a completely new concept that differs from previously known surface electronic states. Conventional surface states, known as Schockley and Tamm states, are electronic states arising from differences in atomic bonding and potential at the crystal surface compared to the bulk interior. These electronic states are due to dangling bonds and surface reconstructions on semiconductor surfaces, and are naturally sensitive to surface contamination and defects. However, topological surface states are independent of the details of the surface structure, impurities, and defects. Even if the bulk is an insulator, the metal-like state remains even if the surface is contaminated. Because this electronic state is based on "time-reversal symmetry," one of the most fundamental properties of nature, it is said to exist robustly regardless of surface contamination or defects.

As shown by the red line (spin up) and dotted blue line (spin down) in Fig. 2.6, topological surface states are known to have various dispersions and characteristics that differ from those of bulk states. They all form within the energy gap of the underlying bulk crystal's electronic bands, and are therefore electronically isolated from the underlying crystal. That is, electrons near the surface sense a discontinuity in the crystal's periodicity and form electronic

states localized only at the surface, resulting from a difference in potential relative to the bulk crystal. In Fig. 2.6(a), the red and blue lines extend into the band gap, down to the Fermi level, indicating "surface-state conduction." However, when the two lines overlap, they also represent "spin degeneracy," where the energy level of the surface state can accommodate both spin-up and spin-down electrons. In other words, each orbital has two distinct degenerate spin states, and spin accumulation does not occur.

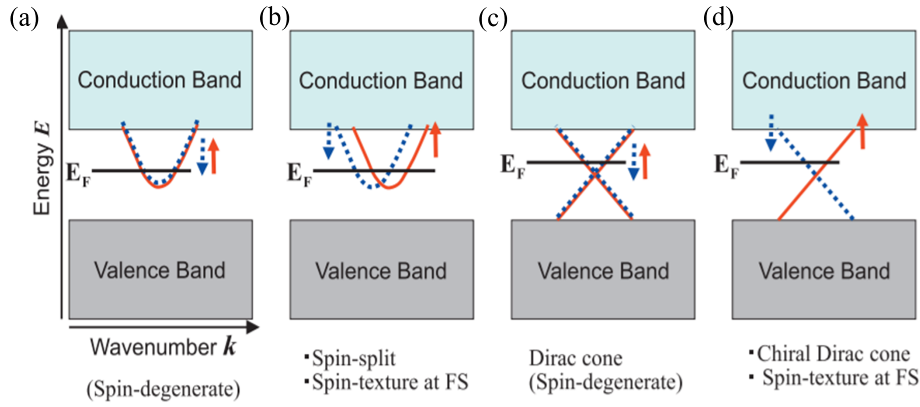

Figure 2.6: schematic diagram of the band structure with different surface state[84]. Reproduced with permission from the right holder, American Physical Society.

In Fig. 2.6 (b), spin degeneracy is broken, splitting the band into two, and the electrons occupying each band have opposite spin orientations. This is the Rashba effect, resulting from strong spin-orbit interaction. In general, a state $(k, \uparrow)$ with wave vector k and spin up is transformed by a time-reversal operation into a state $(-k, \downarrow)$ with both vectors reversed. In the absence of a magnetic field or magnetic impurities, time-reversal symmetry is maintained, so the energies of these two states are equal:

$$E(k, \uparrow) = E(-k, \downarrow) \text{ (Time Reversal Symmetry)} \tag{2.9}$$

On the other hand, a spatial-reversal operation reverses only the wave vector k without changing the spin direction, so state $(k, \uparrow)$ is transformed into

state $(-k, \uparrow)$. Inside a crystal with spatial inversion symmetry, the energies of these two states are equal:

$$E(k, \uparrow) = E(-k, \uparrow) \text{ (Spatial Inversion Symmetry)} \tag{2.10}$$

Therefore, in situations where both time-reversal symmetry and spatial inversion symmetry are maintained, both equations (2.10) and (2.11) hold true. Comparing the right-hand sides of the equations leads to spin degeneracy, where the energy is the same regardless of the spin direction if the wave vector is the same:

$$E(k, \uparrow) = E(k, \downarrow) \text{ (Kramers Degeneracy)} \tag{2.11}$$

However, at crystal surfaces, spatial inversion symmetry is generally broken, so equation (2.11) does not hold. Therefore, even if the bulk state is Kramers degenerate, the surface state may not be degenerate. Thus, $E(k, \uparrow) \neq E(k, \downarrow)$. The difference in energy between opposite spin states is determined by the strength of the spin-orbit interaction.

The linear band dispersion shown in Fig. 2.6(c) has been observed in graphene, a material often used as a superconductor. The energy E is linearly proportional to the wavenumber k, forming a linear dispersion relationship, with two lines intersecting at the band gap to form a Dirac cone[85]. Each band is occupied by electrons with both spin up and spin down, making it a spin-degenerate band. Carbon is a light element, so the spin-orbit interaction is small and the Rashba effect is not observed.

As shown in Fig. 2.6(d), the right-leaning branch and the left-leaning branch form electron bands with opposite spin directions. Because such materials exhibit the Rashba effect and the speed-of-light electrons, research into topological superconductors (insulators that are superconductors only at the surface) has recently produced impressive results[86]. In reality, the dispersion relations are often not as straight as this, but rather curved, such as in topological insulator, which is also one of the subject in this study.

2.2.1 Topological Insulator

Topological insulators (TIs) represent a class of quantum materials characterized by an insulating bulk and conductive surface states. The concept of topological states was initially introduced in the 1980s[87] to elucidate the quantum Hall effect observed in MOSFETs[88]. However, practical applications of the quantum Hall effect have been limited due to its requirement for ultralow temperatures and strong magnetic fields. In 2005, the quantum spin Hall effect (QSHE) was theoretically proposed in materials exhibiting topological order [89], with its presence predicted in HgTe quantum wells in 2006[90]. Unlike the quantum Hall effect, the QSHE arises from spin-orbit interaction and does not require external magnetic fields or low temperatures. Following its experimental observation in 2007[91], research efforts have increasingly focused on the potential for room-temperature applications of TIs. The HgTe quantum well serves as a two-dimensional (2D) TI featuring topological edge states. Subsequently, in 2009, the first three-dimensional (3D) TI, BiSb, exhibiting an insulating bulk and two-dimensional surface states, was identified via angle-resolved photoemission spectroscopy (ARPES)[92].

In TIs, the bulk band structure resembles that of conventional insulators; however, conductive electronic states with Dirac-like dispersion emerge at the edges or surfaces, as illustrated in Figures 2.7(b) and 2.7(d)[90, 93]. Electrons localized on these edges or surfaces experience strong spin-orbit interaction (SOI) accompanied by spin-momentum locking[94, 95]. In 2D TIs, electrons are constrained to two propagation directions, with spin-up and spin-down electrons moving oppositely, as depicted in Figure 2.7(a). The schematic representation of surface state electrons in 3D TIs is provided in Figure 2.7(c). The suppression of backscattering in these states prevents dissipation in spin currents, thereby endowing TIs with significant potential for integration into novel electronic devices. This capability positions TIs as promising candidates for advancing electronic devices beyond the limitations imposed by Moore's Law.

One significant application of topological insulators (TIs) is their use as spin Hall layers in SOT-MRAM, owing to their large spin Hall angles derived from strong spin-orbit interaction (SOI) and Dirac-like energy dispersion[96]. It has been demonstrated that Bi_2Se_3 and $(BiSb)_2Te_3$ exhibit substantial spin

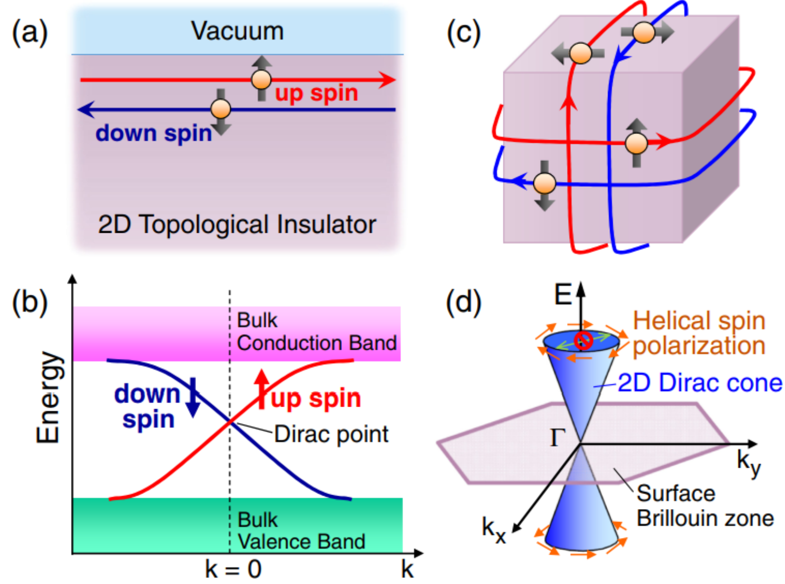

Figure 2.7: (a) Diagram illustrating the edge states in a two-dimensional topological insulator (2D TI). (b) Energy dispersion relation of the spin non-degenerate edge states in a 2D TI, exhibiting a one-dimensional Dirac cone structure. (c) Diagram depicting the two-dimensional surface states in a three-dimensional topological insulator (3D TI). (d) Energy dispersion relation of the spin non-degenerate surface states in a 3D TI, forming a two-dimensional Dirac cone[93]. Reproduced with permission from the right holder, The Physical Society of Japan.

Hall angles of approximately 3.5 and 2.5 at room temperature, respectively. These values are at least an order of magnitude greater than those observed in tungsten (W), which is considered the most effective heavy metal for this purpose. However, the limited surface density of states in these TIs constrains their σ to the order of $\sim 10^4\ \Omega^{-1}\text{m}^{-1}$; for instance, σ is approximately $5.7 \times 10^4\ \Omega^{-1}\text{m}^{-1}$ for Bi_2Se_3 and $1.8 \times 10^4\ \Omega^{-1}\text{m}^{-1}$ for $(Bi_{0.07}Sb_{0.93})_2Te_3$. Since the spin Hall layer interfaces directly with the FM free layer, the relatively low conductivity results in significant current shunting into the FM layer, with less than 10% of the total current passing through the TI. To minimize unnecessary energy dissipation, it is therefore imperative to develop TIs that simultaneously exhibit both a large spin Hall angle and high electrical conductivity.

2.2.2 The Conductive Topological Insulator BiSb

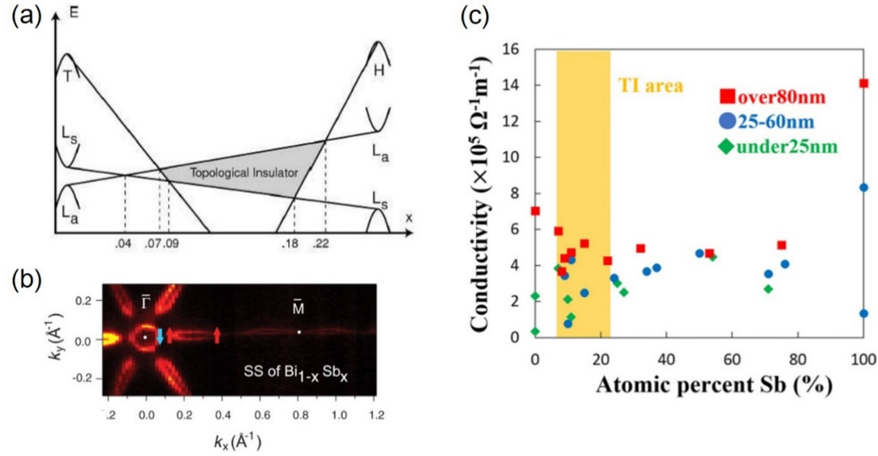

Figure 2.8: (a) Band structure of BiSb[97], reproduced with the permission of copyright holder, Elsevier. (b) ARPES mapping for the surface states of BiSb[92], reproduced with the permission of copyright holder, The American Association for the Advancement of Science. (c) Room temperature conductivity of BiSb as a function of Sb concentration in BiSb thin films with different thickness[98], reproduced with the permission of copyright holder, AIP Publishing.

The BiSb crystal, composed of group-V semimetals bismuth (Bi) and antimony (Sb), exhibits the same rhombohedral A7 crystal structure as its constituent elements. It has been established that a band gap emerges when the Sb concentration ranges between 7% and 22% [97, 99], as illustrated in Figure 2.8(a). Within this compositional window, BiSb behaves as a topological insulator (TI), characterized by a small bulk band gap of approximately 20 meV[97, 99] and a high bulk σ on the order of 4 to 6.4×10^5 $\Omega^{-1}\text{m}^{-1}$[100]. In thin films, quantum size effects substantially enhance the band gap of BiSb, resulting in predominant surface conduction when the film thickness is reduced to around 10 nm[98]. Owing to the presence of multiple surface states, the conductivity of BiSb thin films can reach values as high as 2.5×10^5 $\Omega^{-1}\text{m}^{-1}$. Figure 2.8(c) presents a summary of the room temperature conductivity of BiSb thin films as a function of Sb concentration across various thicknesses.

Furthermore, ARPES mapping, depicted in Figure 2.8(b)[92], confirms the existence of Dirac cones associated with the surface states, indicative of a

pronounced spin Hall effect (SHE) in BiSb. Prior investigations conducted by our research group have demonstrated that epitaxial BiSb(012)/MnGa bilayers exhibit a spin Hall angle as high as 52, representing the largest value reported to date among known materials. However, these studies employed molecular beam epitaxy (MBE) for film growth. Consequently, there is a critical need to develop methods for producing high-quality BiSb thin films via sputtering deposition to facilitate integration into SOT-MRAM.

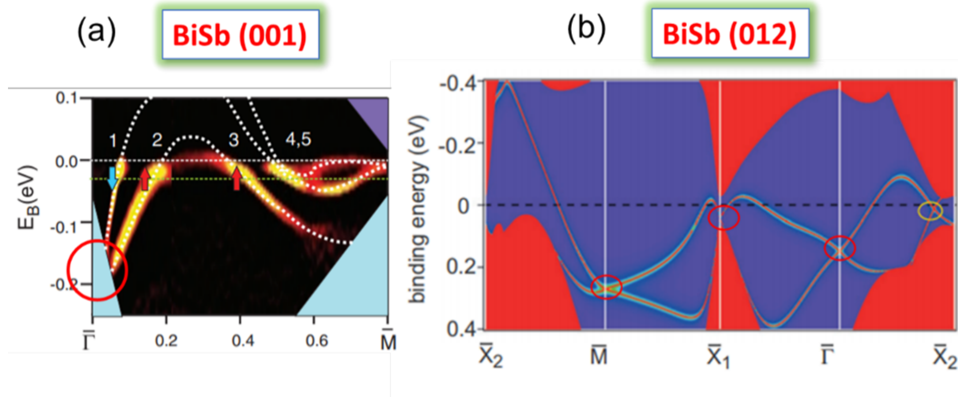

Figure 2.9: Topological surface states for (a) BiSb(001)[92], reproduced with the permission of copyright holder, The American Association for the Advancement of Science, and (b) BiSb(012)[101]. The circles indicate Dirac cones, reproduced with the permission of copyright holder, New Journal of Physics.

The spin Hall angle of BiSb is significantly influenced by the quality of the crystal and the interface with the ferromagnetic layer. A BiSb layer exhibiting a spin Hall angle of 52, epitaxially grown via molecular beam epitaxy (MBE), demonstrates a high-quality single-crystal structure with an optimized (012) orientation. It is established that the BiSb(012) surface hosts four Dirac cones: three arising from time-reversal symmetry located at the $\bar{\Gamma}$, $\bar{C}_1$, and $\bar{M}$ points, and one originating from crystal symmetry near the $\bar{C}_2$ point, as illustrated in Figure 2.9(b)[101]. In contrast, other surface orientations, such as BiSb(001), possess only a single Dirac cone at the $\bar{\Gamma}$ point, as depicted in Figure 2.9(a)[92]. Given that Dirac points serve as monopoles of Berry curvature, the BiSb(012) surface exhibits the largest spin Hall angle due to a pronounced intrinsic mechanism, whereas other orientations yield comparatively smaller spin Hall angles. Consequently, the optimization of crystal orientation is critical for achieving a substantial spin Hall angle in BiSb.

Chapter 3

Chapter 3: Sample preparation and characterization techniques

3.1 Sample preparation

3.1.1 Magnetron sputter

Magnetron sputtering is a commonly used physical vapor deposition (PVD) method with many advantages, such as low deposition temperature, fast deposition rate, good uniformity of deposited films, and composition close to that of the target material. Under high vacuum conditions, a suitable amount of argon gas is introduced. A DC or RF power between $3 \sim 120$ W is applied between the cathode (cylindrical target or planar target) and the anode (coating chamber wall). This generates a magnetron-controlled glow discharge within the coating chamber. Electrons, under the influence of an electric field E, collide with argon atoms as they fly towards the substrate, ionizing the argon gas (Ar atoms ionize into Ar^+ ions and electrons under high voltage). The incident ions (Ar^+) bombard the target material under the influence of the electric field, causing neutral atoms or molecules on the target surface to gain sufficient kinetic energy to detach from the target surface and deposit on the substrate to form a thin film as shown at Fig. 3.1 . The resulting secondary electrons are affected by both electric and magnetic fields[102], resulting in a drift in the direction indicated by $E \times B$, a phenomenon known as $E \times B$ drift. Their trajectory approximates a cycloid. If the magnetic field is toroidal, the

electrons move in a circular motion on the target surface in an approximate cycloid manner. Their path is not only long but also confined to a plasma region near the target surface, where they ionize a large number of Ar^+ ions to bombard the target material, thus achieving a high deposition rate.

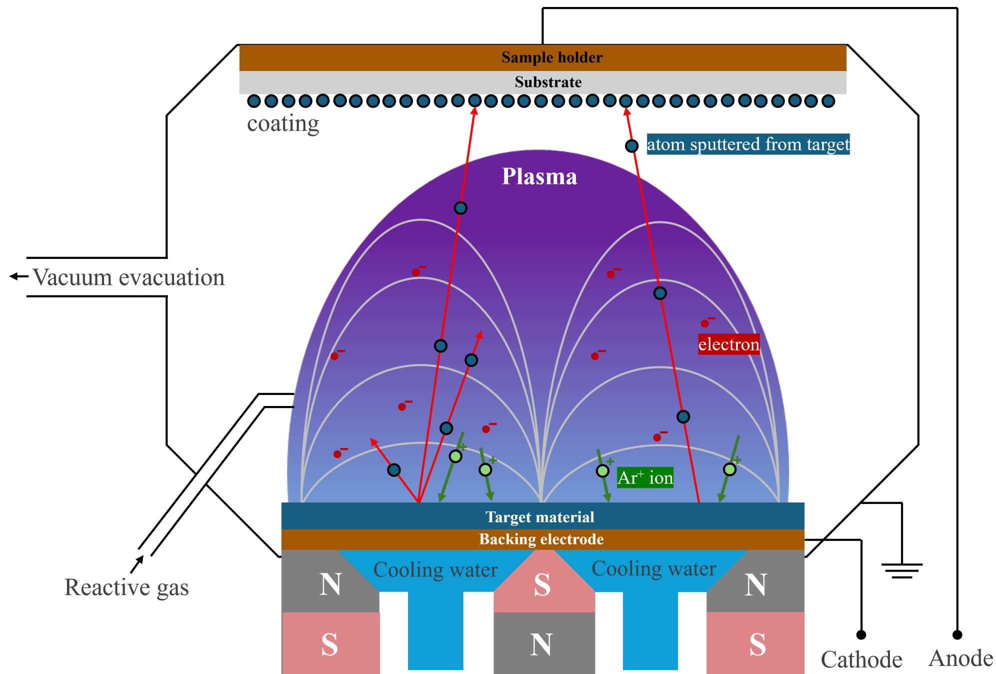

Figure 3.1: Schematic illustration of the magnetron sputtering system used for thin-film deposition.

The sputtering behavior is highly influenced by whether the target material is magnetic or not. For non-magnetic targets like Bi, Sb, and BiSb, the external magnetic field easily penetrates the target, creating a stable plasma above its surface. On the other hand, for magnetic targets such as Co, Fe, and CoFeB, part of the magnetic flux is absorbed by the target, which weakens the magnetic field near the surface. This phenomenon, known as the magnetic short-circuit effect, reduces plasma confinement and causes the plasma to move toward the edges, leading to a lower sputtering rate and poorer film uniformity. To address this, stronger magnets, improved magnetic yoke designs, or RF-assisted power sources are commonly used to stabilize the discharge.

In this study, both non-magnetic (BiSb) and ferromagnetic (CoFeB) tar-

gets were utilized. Consequently, sputtering conditions—including discharge power, argon pressure, and the distance between the target and substrate were individually optimized to achieve uniform thickness and well-defined interfaces in the BiSb/interlayer/CoFeB and Mo/CoFeB/$MgAl_2O_4$ heterostructures.

3.1.2 Hallbar fabrication process

The Hall bar fabrication process is briefly described below:

I. Sample Cleaning:

(1) Organic Cleaning

1-1. Boil acetone (130°C, 10 minutes); 1-2. Rinse acetone with ethanol, then rinse ethanol with ultrapure water; 1-3. Dry with an N_2 gun;

II. Device Fabrication:

(1) Resist Coating

1-1. Apply PMGI using a spin coater under the following conditions: (1st: 1000 rpm for 3 seconds, 2nd: 4000 rpm for 60 seconds, 3rd: 0 rpm for 3 seconds) $\rightarrow$ Resist thickness: $\sim 1.5\mu m$ 1-2. Pre-bake (150°C, 300 seconds); 1-3. Apply OFPR using a spin coater under the following conditions: (1st: 1000 rpm for 3 seconds, 2nd: 3000 rpm for 60 seconds, 3rd: 0 rpm for 3 s) $\rightarrow$ Resist thickness: $\sim 1.5\mu m$ 1-4. Pre-bake (110°C, 90 seconds);

(2) Exposure

2-1. Perform using a maskless lithography system; input the device pattern into a computer connected to the system, set the exposure time to approximately 1 second, and automatically expose;

(3) Development

3-1. Develop with developer (NMD-3) (rest for 45 seconds); 3-2. Rinse NMD-3 with pure water;

(4) Perform ion milling (dry etching) to form the Hall bar device.

(5) Resist removal

5-1. Resist Remover 104 (130°C, until the resist is removed); 5-2. clean up the Resist Remover 104 with ethanol; 5-3. Dry sample with an N_2 gun

The schematic illustration of these steps is shown as the step (1)$\sim$(5) in Fig. 3.2.

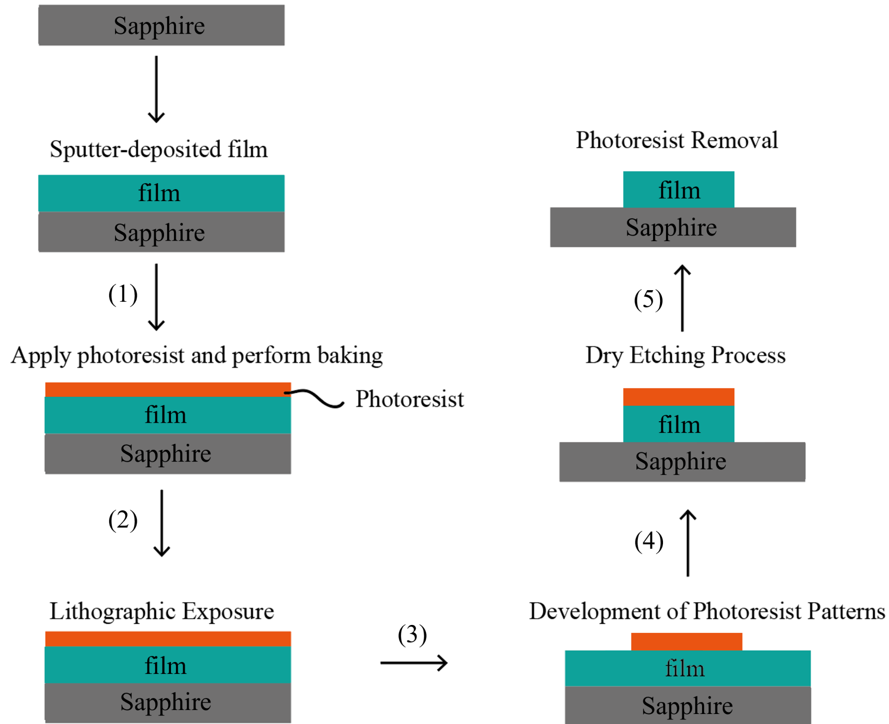

Figure 3.2: Schematic illustration of the standard photolithography process, including film deposition, photoresist coating, baking, exposure, development, dry etching, and photoresist removal.

3.2 Magnetization measurement

AHE Measurement

The anomalous Hall effect (AHE) was measured using a standard four-probe setup. A constant direct current was applied along the x-axis with a Keithley 2450 Source Meter, while an out-of-plane magnetic field (H_z) was varied using a high-current bipolar power supply controlled through a GPIB interface module. Both the longitudinal voltage (V_{xx}) and the transverse Hall voltage (V_{xy}) were recorded simultaneously using ADCMT 7461A Digital Multimeters. These voltage readings were then converted into resistance values (R_{xx} and R_{xy}) by dividing by the applied current.

Second harmonic measurement

Second harmonic measurement is a technique for estimating the magnitude of the spin-Hall angle by applying an AC current to a heterojunction sample consisting of a ferromagnetic layer and a spin current source layer and measuring the second harmonic component of the AC Hall voltage. When the Hall resistance depends on the magnetization direction of the ferromagnetic layer, the spin current source layer injects a spin current at the same frequency as the current, so the magnetization oscillates at the same frequency around the equilibrium position. Thus, the measured voltage along xy direction V_{xy} can be written as follows:

$$V_{xy} = (R_{xy0} + \Delta R_{xy} \sin \omega t) \cdot I \sin \omega t \tag{3.1}$$

Here, R_{xy0} is the Hall resistance when the magnetization direction is at equilibrium. ΔR_{xy} is the fluctuation component of the Hall resistance caused by the magnetization oscillation generated by the spin current; the larger the magnetization oscillation, the larger ΔR_{xy} becomes. Based on this equation, if a current $I \sin \omega t$ is injected in the longitudinal direction of the Hall bar described in the previous section, V_{xy} is read in the transverse direction.

$$\begin{aligned} V_{\mathrm{xy}} &= \frac{1}{2}\Delta R_{\mathrm{xy}} I + \Delta R_{\mathrm{xy0}} I \sin \omega t - \frac{1}{2}\Delta R_{\mathrm{xy}} I \cos 2\omega t \\ &= V_{\mathrm{xy}}^{\mathrm{DC}} + V_{\mathrm{xy}}^{\omega} \sin \omega t + V_{\mathrm{xy}}^{2\omega} \cos 2\omega t \end{aligned} \tag{3.2}$$

The $\sin \omega t$ and $\sin^2 \omega t$ terms of the read V_{xy} are separated, and the $\sin^2 \omega t$ term is converted to $\cos 2\omega t$ to evaluate the Hall resistance due to magnetization oscillations caused by the spin current. However, in many cases, the measured value of ΔR_{xy} contains components due to various physical phenomena in addition to the component reflecting the spin Hall effect.

To easily separate the terms contained in ΔR_{xy}, it is necessary to sweep the external magnetic field H_{ext} parallel to the current and further separate them by utilizing the differences in the dependence of each phenomenon on the external magnetic field, as shown in equation (3.3). For this reason, in most cases, $V_{\mathrm{xy}}^{\mathrm{DC}}$ is omitted and only $V_{\mathrm{xy}}^{2\omega}$ is used.

$$R_{\rm xy}^{2\omega} = \frac{R_{\rm AHE}}{2}\frac{H_{\rm DL}}{|H_{\rm ext}| - H_{\rm k}} + R_{\rm ONE}|H_{\rm ext}| + R_{\rm ANE+SSE} \tag{3.3}$$

where $R_{\rm AHE}$ is the anomalous Hall resistance, $H_{\rm DL}$ is the damping-like field caused by the spin current, $H_{\rm k}$ is the anisotropy field, $R_{\rm ONE}$ is the normal Nernst effect component, and $R_{\rm ANE+SSE}$ represents contribution from the anomalous Nernst effect and spin Seebeck effect.

Then, by fitting $R_{\rm xy}^{2\omega}$ as a function of $H_{\rm ext}$, the damping-like field $H_{\rm DL}$ can be estimated. Finally, $\theta_{\rm SH}$ whose details will be discussed in Chapter 4, can be calculated.

To assess the effects caused by spin-orbit torque, an alternating current at 259.68 Hz was applied along the x-axis with a Keithley 6221 AC/DC current source, while the $V_{\rm xy}^{2\omega}$ in the transverse direction was measured using an NF LI5650 Digital Lock-in Amplifier. A magnetic field was applied parallel to the current. This approach allows for a quantitative evaluation of spin-orbit torque efficiency by analyzing the harmonic signals.

SOT Switching Test

For switching tests, the Keithley Model 6221 AC/DC current source can be used to output a series of pulses, allowing for various levels of the pulse amplitude. For one cycle, a high pulse was firstly applied, followed by a low pulse, and a 2182A NanoVoltemeter was triggered to collect data after each pulse.

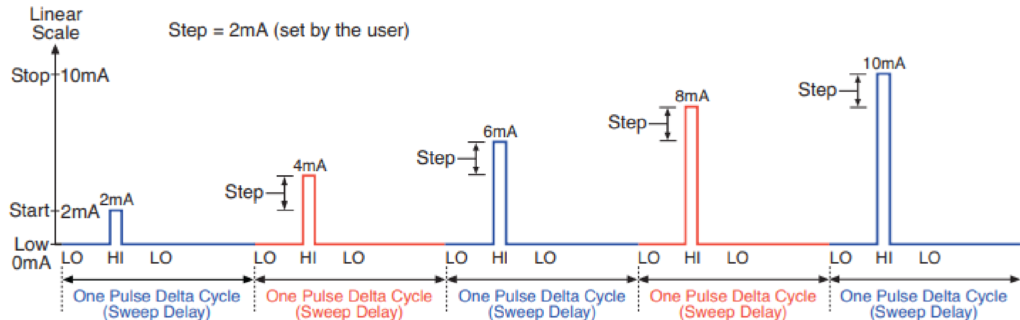

Figure 3.3: Sweep current waveform for switching test.

Superconducting Quantum Interference Device

The SQUID (Superconducting Quantum Interference Device) is the most sensitive device for measuring the magnetic properties of materials. Here, we have used an EverCool equipped MPMS-XL SQUID magnetometer from Quantum Design for magnetization measurement in this study.

The SQUID measurement is based on the tunneling supercurrent occurring between two superconductors separated by a small insulating junction which is called as Josephson Junctions, and there is a relationship of the phase difference between the two superconductors and the magnetic flux.

In Fig. 3.4, a loop with two Josephson Junctions in a magnetic field is shown. In the absence of an external magnetic field, the input current is distributed equally between the two junctions. However, when an external magnetic field is present, the currents in the two branches become unequal, generating a magnetic field that counteracts the external magnetic flux. Consequently, a voltage is induced within the circuit. By measuring this induced voltage, the magnitude of the external magnetic field can be determined.

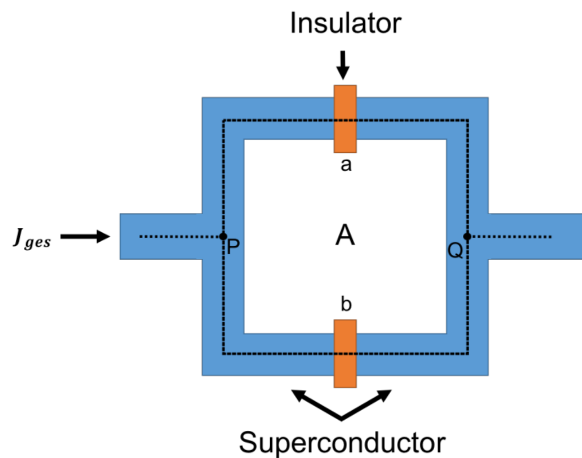

Figure 3.4: A SQUID is made up two Josephson junctions a and b connected in parallel. Reproduced from[103], reproduced with permission of copyright holder, Springer Nature.

Vibrating Sample Magnetometer (VSM) Equipment

VSM is a device used to quickly measure the H_k and H_c of samples. It can measure those magnetism properties of a sample from the induced electromotive force generated in the detection coil when the sample is vibrated at a constant frequency in a uniform magnetic field. It is characterized by its ability to perform high-speed measurements at room temperature. In this study, the VSM device shown below was used. It can measure magnetization in the perpendicular and in-plane directions, and can apply an external magnetic field of up to 1.5 T.

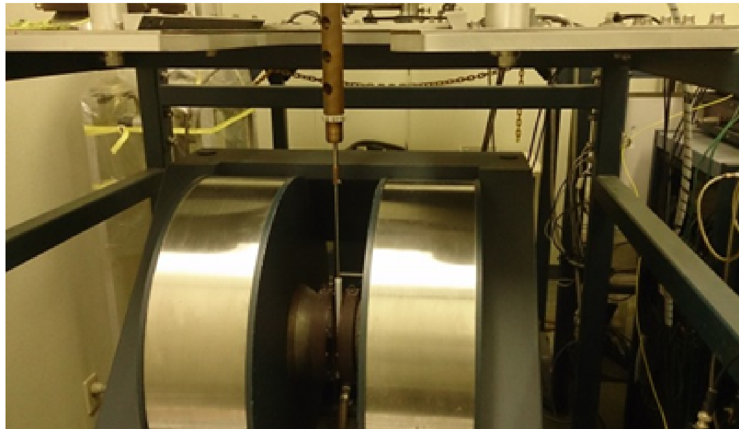

Figure 3.5: VSM equipment with sample holder.

3.3 Characterization techniques

3.3.1 X-ray reflectivity

The X-ray reflectivity (XRR) technique has very important features for this study: 1) It is applicable for analyzing single-crystal, polycrystalline, or amorphous materials. 2) It allows for assessment of roughness. 3) It can be used to examine films that are opaque to visible light. 4) It enables determination of the layer structure in both multilayer and single-layer films. 5) It can measure film thicknesses ranging from a few nanometers up to 1000 nanometers. Based on these features, XRR is the most precise tool to estimate film thickness, thus, sputtering rate in this study.

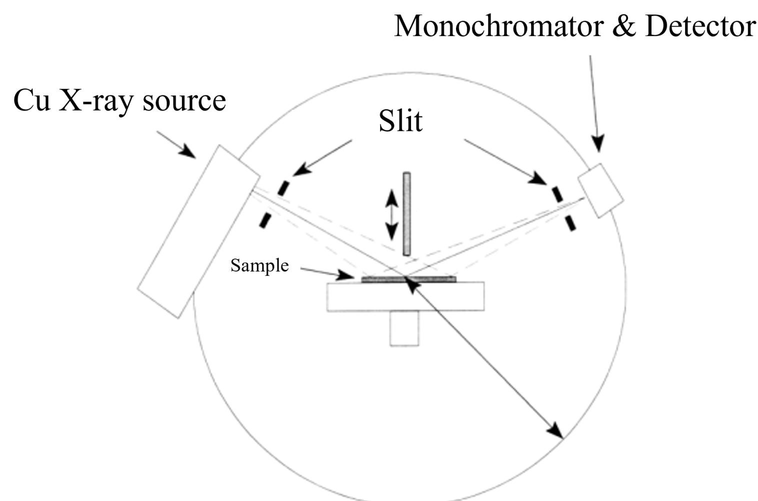

Figure 3.6: Schematic setup of the diffractometer used for the reflection measurement. Copyright © Rigaku.

Figure 3.5 shows the schematic setup of the diffractometer used for the reflection measurement. The detector and the x-ray tube lie on a circle and can be rotated around the common center, where the sample is placed. The detector is a scintillation counter with a monochromator-crystal placed in front, so that only the Cu-Kα-radiation can reach the detector. To avoid a saturation of the detector, the reflectivity curve must be measured with an attenuator.

Figure 3.6 presents an overview of how film thickness, density, and the roughness of both the surface and interface influence the X-ray reflectivity curve of a thin film.

Film thickness

The basic reason of why oscillations in reflected intensity occurs is that the detected scattered X-rays result from the combined scattering of individual electrons when a substrate composed of an ideal material is uniformly coated with a substance of different density. In other word, the X-ray reflectivity intensity is computed for each layer, which is defined by its elemental composition and the filling rate of the spacer, so we use film thickness, density and interface roughness as parameter for fitting XRR result. These oscillations were first

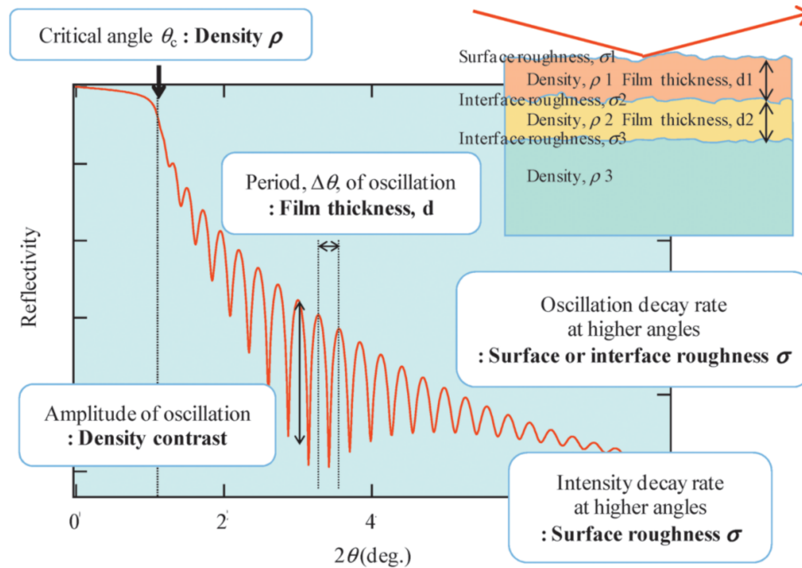

Figure 3.7: Film structural information obtained from the X-ray reflectivity profile.. Copyright © Rigaku.

observed in 1931 by Kiessing and is called Kiessing fringes[104]. Based on his result, the oscillation depends on the film thickness, and the thicker film, the shorter period of the oscillations.

Film Density

The oscillation amplitude and the critical angle for total reflection reveal details about the density of films. The oscillation amplitude is influenced by the density difference between the film and its substrate, so the greater this difference, the larger the oscillation amplitude is.

Interface Roughness

Reflected X-rays diminish more quickly as interface roughness increases. In other words, the greater the roughness of a film, the faster the X-ray reflectivity decreases, so the oscillation amplitude decreases.

Parameter fitting

Because the obtained profile is related to three parameters: film thickness, density, and interface roughness, one of the biggest issues in XRR measurements is how to approximate the fit results, which are determined by these parameters, to the measured profile. In practice, this is considered a combined optimization problem of parameters, and fitting is always performed using a genetic algorithm[105].

First, many "genes" of parameter set are created randomly distributed within a certain range around the set value. The simulation results for all of these genes are compared with the raw data, and a "score" is calculated using the least-squares method. Only the top-performing genes are allowed to survive to the next generation. There are various specific methods, such as allowing only the top 20% of genes to survive. The surviving genes then make copies of themselves to create offspring, which are then shuffled with other genes through a process known as "gene crossover." This shuffling process generates the next generation of genes, which are then scored again, leaving only the top 20% to produce offspring. Repeating this process leads to a point where, after several generations, the score no longer improves. This is called convergence, and it is what makes combinatorial parameter optimization successful[105].

3.3.2 Auger electron spectroscopy

Auger electron spectroscopy (AES) is a type of electron spectroscopy that utilizes the Auger effect, involving the examination of high-energy electrons released from an excited atom following a sequence of internal relaxation processes.

AES is currently a highly effective technique for analyzing surfaces, thin films, and interfaces. Its usefulness comes from its surface specificity, which ranges from 0.5 to 10 nanometers, excellent spatial resolution on the surface—down to about 10 nanometers—broad coverage of elements across the periodic table (excluding hydrogen and helium), and a decent sensitivity level, detecting concentrations as low as 100 parts per million for most elements.

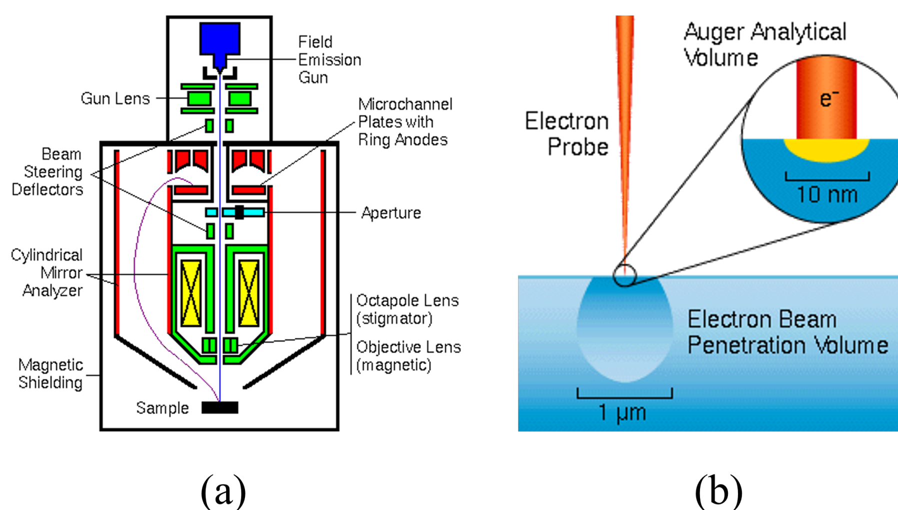

Figure 3.8: (a) Schematic illustration of AES instrument structure, (b) Auger analytical volume. Copyright © Eurofins Scientific.

Instrument Structure

The instrument used in this study is called JAMP-9500F manufactured by JEOL whose main body consists of two chambers: a sample exchange chamber and an analysis chamber, separated by a gate valve. The analysis chamber is evacuated by a sputter ion pump (SIP) and maintained at an ultra-high vacuum of less than 5×10^{-8} Pa. The sample exchange chamber is evacuated by a TMP and a RP.

The JAMP-9500F is a field emission Auger microprobe that achieves high spatial resolution at high currents thanks to a Schottky Field Emission Gun (FEG) and a unique electron optical system. The energy analyzer uses an electrostatic hemispherical analyzer, and the combination of a multi-channel multiplexed detector and an entrance lens optimized for Auger analysis enables high-sensitivity, high-energy-resolution spectra. Furthermore, the instrument can also analyze insulating materials by neutralizing the charge using a neutralization gun.

FEG consist of extremely sharp tungsten tips subjected to electric fields greater than 10^7 V/cm. Under these conditions, electrons tunnel directly through the energy barrier and are emitted from the tip. FEG produce the brightest beams, with current densities ranging from 10^3 to 10^6 A/cm^2, and

electron beams as small as 10 nm, enabling the examination of very small features. Electrostatic hemispherical analyzers are the most commonly used type because their high transmission efficiency improves signal-to-noise ratios. The primary electron beam strikes the sample surface at the analyzer's source point. Auger electrons are emitted in all directions, and some pass through an aperture in the analyzer's inner hemisphere. A variable negative voltage applied to the outer hemisphere deflects the Auger electrons back through a second aperture in the inner hemisphere and then through an exit aperture aligned with the analyzer's axis.

The Auger Process

The Auger process begins when an electron is removed from an inner atomic shell, creating a vacancy. This vacancy can be generated through various methods, but the most common is by bombarding the atom with an electron beam. An electron from an outer shell then fills the inner shell vacancy, and the energy released from this transition causes a third electron, known as the Auger electron, to be ejected from the atom.

The Auger process refers to an excited ion losing energy by ejecting an electron, resulting in a doubly charged ion. Alternatively, this energy can be released through the emission of an X-ray photon. For elements with low atomic numbers, the most likely transitions happen when a K-shell electron is removed by the primary beam, an electron from the L-shell fills the vacancy, and another L-shell electron is emitted. In contrast, for elements with higher atomic numbers, transitions such as LMM and MNN are more common than KLL transitions.

Qualitative analysis depends on the identification of the elements responsible for the peaks in the spectrum. There are most strongest and most characteristic Auger peaks in the KLL, LMM, and MNN parts of the spectrum for each element. For the detailed compositional and elemental analysis of a sample, it relies on measuring the number of Auger electrons emitted during the probing process. The electron yield is influenced by several key factors, including the electron-impact cross-section and the fluorescence yield. Based on the standard data of characteristic Auger peaks' intensity and Auger electron yield for each element, the separation from raw AES signal which is collected

from complicated compound to a series of single element AES signal can be executed semi-quantitatively[106].

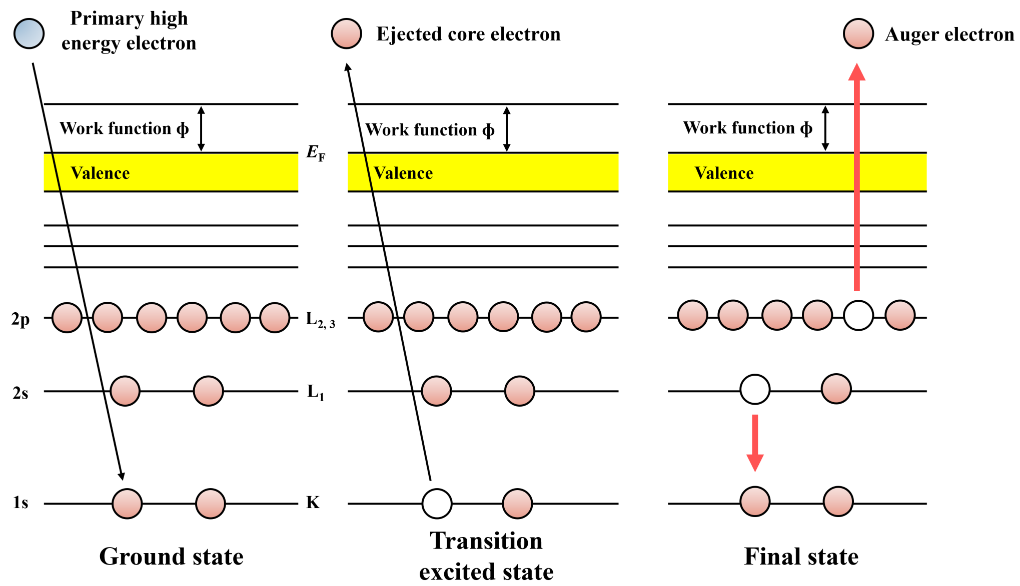

Figure 3.9: Schematic illustration of a full Auger process including primary high energy electron impact, core electron ejecting, Auger electron ejecting.

Depth profile analysis

Because Auger electrons can only probe information from a few nanometers beneath the surface, ion sputtering is employed to etch the surface when the contamination layer is thick or when analyzing deeper regions. By alternating between sputtering and measurement, a depth profile of elemental composition can be obtained from the spectral data. These depth profiles are utilized to assess film thickness in multilayer samples and to investigate causes of metal discoloration or corrosion. Argon (Ar) ions are commonly used for Auger depth profile analysis.

Chapter 4

High spin Hall angle in BiSb topological insulator and perpendicularly magnetized CoFeB/MgO multilayers with metallic interfacial layers

4.1 Introduction

Spin-orbit torque magnetoresistive random-access memory (SOT-MRAM) has been attracting attention for this role thanks to its low energy consumption, high durability, and ultrafast writing[107, 108, 109, 110, 111]. In SOT-MRAM, it is essential to integrate a SOT layer with a strong spin Hall effect and a perpendicularly magnetized magnetic tunnel junction (p-MTJ), which is commonly based on CoFeB/MgO with perpendicular magnetic anisotropy (PMA). While heavy metals (HMs) have been widely studied for SOT, the limited spin Hall angle θ_{SH} of HMs (typically < 1)[112, 113] results in large writing current density and high writing energy. Furthermore, large driving transistors are required to support the large writing current of HMs. Indeed, K. Garello et al. have used W (θ_{SH} $\sim$0.4) for the SOT layer and demonstrated ultrafast SOT switching in 60 nm p-MTJ by 1 ns pulse currents, but the current is as large as

$279 \sim 290$ μA, which is significantly larger than the typical 40 μA of the spin-transfer-torque (STT) current for the same 60 nm p-MTJ[114]. To decrease the writing current density and energy, it is important to integrate SOT materials with high spin Hall angle to CoFeB/MgO-based p-MTJ. Recently, topological insulators (TIs) such as Bi_2Se_3, $(BiSb)_2Te_3$, and BiSb with topological surface states have been shown to have very large θ_{SH} (> 1)[115, 116, 42, 50]. Among them, BiSb is very promising since it shows the highest $\theta_{SH} \sim 52$ and relatively high electrical conductivity $\sigma \sim 2.5 \times 10^5\ \Omega^{-1} \cdot \mathrm{m}^{-1}$ in epitaxial BiSb(012) grown by molecular beam epitaxy (MBE) at room temperature[42]. The giant spin Hall effect in BiSb was also confirmed by measuring the inverse spin Hall effect (inverse $\theta_{SH} \sim$ 61) in CoFe/MgO/BiSb structure, where a spin-polarized current was injected from CoFe/MgO to BiSb[49]. Furthermore, BiSb can be deposited by the industry-friendly sputtering technique while showing decent θ_{SH} ~10 and $\sigma \sim 1.5 - 1.8 \times 10^5\ \Omega^{-1} \cdot \mathrm{m}^{-1}$for BiSb(110) and BiSb(001) at room temperature[117, 118]. However, previous works on sputtered BiSb with high θ_{SH} have been performed in heterostructures with Co or Co/Pt multilayers, which are not the main stream ferromagnetic metal (FM) in p-MTJ. Thus, it is essential to demonstrate high θ_{SH} of BiSb in heterojunctions with perpendicularly magnetized CoFeB/MgO[47], which is now the de facto FM/tunnel barrier for p-MTJ. Recently, a maximum θ_{SH} of 2.8 has been realized in BiSb/CrO_x/Ta/CoFeB/MgO[48], which helps reducing the SOT switching current to the level of that of STT. However, higher θ_{SH} is essential to further reduce the SOT switching current to lower than that of STT.

In this study, we investigate the spin Hall performance in heterostructures of $Bi_{0.85}Sb_{0.15}$ (10 nm) / interfacial layers / $Co_{20}Fe_{60}B_{20}$/MgO with PMA. While the thick MgO interlayer used in the inverse spin Hall effect measurement (Ref.[49]) is useful for enhancing the spin-polarization of the injected spin-polarized current, MgO is known to strongly suppress diffusion of the pure spin current. Thus, the MgO interlayer is not suitable for SOT-MRAM application. For this reason, we chose to use metallic interlayers in this work. By optimizing the metallic interfacial layer thickness as well as deposition condition of BiSb, we achieve large effective spin Hall angle θ_{SH}^{eff} of 6.0±0.1 and relatively high electrical conductivity $\sigma_{BiSb} = 1.5\times10^5\ \Omega^{-1} \cdot \mathrm{m}^{-1}$ at room tem-

perature, which are larger than those of the MBE-grown $(\mathrm{BiSb})_2\mathrm{Te}_3$ ($\theta_{\mathrm{SH}}^{\mathrm{eff}} = 2.5$ and $\sigma_{\mathrm{BiSb_2Te_3}} = 1.8\times10^4\ \Omega^{-1}\cdot\mathrm{m}^{-1}$[50]. We then demonstrate SOT-induced magnetization switching driven by a small threshold current density $|J_{\mathrm{th}}|$ of 1×10^6 A·cm^{-2}. Benchmarking using a bilayer model shows that the writing power consumption of our stack is 2∼3 orders smaller than that of HMs.

4.2 Sample preparation

Figure 4.1(a) shows the schematic of our heterostructures, which are deposited on c-plane sapphire substrates using DC (for BiSb and metals) and RF (for MgO) magnetron sputtering. Here, the crystallization of sputtered BiSb on c-plane sapphire substrate has been systematically studied where the quasi-single-crystal BiSb(001) with equivalent twin crystals can be confirmed[119]. We deposited 10 nm-thick BiSb with a low power of 3 W for a low rate of 1.3 nm·min^{-1}, or a higher power of 10 W for a higher rate of 3.3 nm·min^{-1}, using a 2 inch-diameter $\mathrm{Bi_{0.85}Sb_{0.15}}$ alloy target. The electrical conductivity of our s puttered BiSb thin films is $1.5\times10^5\ \Omega^{-1}\cdot\mathrm{m}^{-1}$, which is an order of magnitude higher than that of MBE-grown $\mathrm{Bi_2Se_3}$ or $\mathrm{BiSb_2Te_3}$[115, 50]. Then, we deposited metallic interfacial layers of Ti (Ru) (1 ∼ 4 nm) / Ta (0.8 nm) on well-crystallized BiSb(001). Finally, we deposited CoFeB (1 nm) / MgO (2.5 nm)/ Ta (1 nm) cap. Here, a Ti(Ru) interfacial layer inserted between the TI and FM layers has been shown to suppress Sb diffusion and enhance $\theta_{\mathrm{SH}}^{\mathrm{eff}}$ in BiSb/Co and $\mathrm{BiSb_2Te_3}$/CoFeB[120, 121]. Thicker interfacial Ti(Ru) layers can suppress Sb diffusion better than thin Ti(Ru), but with the trade-off of increasing shunting current and spin loss. Thus, there is an optimized Ti(Ru) thickness to achieve the highest $\theta_{\mathrm{SH}}^{\mathrm{eff}}$.

The 0.8 nm-thick Ta layer provides a further Sb diffusion barrier and also works as B absorber from CoFeB during post-growth thermal annealing. After the deposition of the full stack, we performed post-growth thermal annealing at 250 °C for 30 mins in ultrahigh vacuum (1×10^{-6} Pa), during which $\mathrm{Co_{20}Fe_{60}B_{20}}$ was crystallized to bcc-$\mathrm{Co_{25}Fe_{75}}$ with high saturation magnetization, and PMA of the resulting CoFe/MgO was realized. Then, we fabricated $25\times10\ \mu\mathrm{m}^2$ Hall bar devices for electric measurement with DC, AC, and pulsed current source. Fig. 4.1(b) shows an optical image of our Hall bar and measurement setup.

We also prepared reference stacks without BiSb but with Ta(0.8 nm), Ru(3 nm)/Ta(0.8 nm), and Ti(3 nm)/Ta(0.8 nm) interfacial layers, and confirmed that the parasitic SOT in those metallic interfacial layers is negligible with parasitic θ_{SH} less than 0.05.

4.3 PMA and Effective Spin Hall Angle $\theta_{\mathrm{SH}}^{\mathrm{eff}}$ Evaluation

We first examined PMA and the spin Hall effect in BiSb (10 nm)/Ru (1∼4 nm)/Ta(0.8 nm)/CoFeB (1 nm) /MgO (2.5 nm)/Ta (1 nm) stacks. The BiSb in these stacks was deposited by 10 W (high power condition). Figure 4.2(a) and 4.2(b) show the anomalous Hall resistance R_{AHE} of the sample with Ru (3 nm), measured with an out-of-plane magnetic field H_{z} and an in-plane magnetic field H_{x}, respectively. We achieved a large PMA field $H_{\mathrm{k}} = 4.6$ kOe by,

$$R_{\mathrm{AHE}} = R_{\mathrm{AHE}}(0)\sqrt{1-\left(\frac{H_{\mathrm{x}}}{H_{\mathrm{k}}}\right)^{2}}, \tag{4.1}$$

which is obtained by fitting the low field data in Fig. 4.2(b) red solid line. This large H_{k} is similar to typical values in high quality CoFeB/MgO reported in literature[47]. We then evaluate the spin-orbit torque generated by BiSb using the second harmonic Hall measurement technique with an AC at 259.68 Hz and an in-plane magnetic field H_{k}. When H_{k} is larger than H_{k}, the second harmonic Hall resistance $R_{\mathrm{xy}}^{2\omega}$ is given by[122]

$$R_{\mathrm{xy}}^{2\omega} = \frac{R_{\mathrm{AHE}}}{2}\frac{H_{\mathrm{AD}}}{H_{\mathrm{x}} - H_{\mathrm{k}}\cdot H_{\mathrm{x}}/|H_{\mathrm{x}}|} + R_{\mathrm{PHE}}\frac{H_{\mathrm{FL}}}{H_{\mathrm{x}}} + R_{\mathrm{ANE+SSE}}\frac{H_{\mathrm{x}}}{|H_{\mathrm{x}}|} \tag{4.2}$$

where H_{AD} and H_{FL} are the effective field corresponding to the antidamping-like $\vec{m}\times(\vec{m}\times\vec{\sigma})$ and field-like $\vec{m}\times\vec{\sigma}$ torques, R_{PHE} is the planar Hall resistance, and $R_{(\mathrm{ANE+SSE})}$ reflects contribution from the anomalous Nernst effect and the spin Seebeck effect. Figure 4.2(c) shows $R_{\mathrm{xy}}^{2\omega} - H_{\mathrm{x}}$ curves measured by AC of 2.4 – 4 mA. Figure 4.2(d) shows fitting by Eq. (4.2) for $H_{\mathrm{x}} > H_{\mathrm{k}}$, from which we can obtain H_{AD}. Figure 4.3(a) shows H_{AD} as a function of the BiSb current

density J_{BiSb}. Then, we calculate

$$\theta_{\mathrm{SH}}^{\mathrm{eff}} = \frac{2e}{\hbar} t_{\mathrm{FM}} M_{\mathrm{S}} \frac{\partial H_{\mathrm{AD}}}{\partial J_{\mathrm{BiSb}}}, \tag{4.3}$$

where t_{FM} and M_{S} are the thickness and saturation magnetization of CoFeB measured by a superconducting quantum interference device. $\theta_{\mathrm{SH}}^{\mathrm{eff}}$ is calculated to be 1.5±0.1 from the gradient $\frac{\partial H_{\mathrm{AD}}}{\partial J_{\mathrm{BiSb}}}$ in Fig. 4.3(a). Figure 4.3(b) summarizes $\theta_{\mathrm{SH}}^{\mathrm{eff}}$ as a function of the Ru thickness t_{Ru}. We observed that $\theta_{\mathrm{SH}}^{\mathrm{eff}}$ reaches maximum value at $t_{\mathrm{Ru}} = 3$ nm. However, further increasing of t_{Ru} reduces $\theta_{\mathrm{SH}}^{\mathrm{eff}}$ significantly, which is explained by the short spin diffusion length of Ru, consistent with spin pumping results in NiFe/Ru/Pt[123].

Next, we investigate the BiSb (10 nm)/Ti (1-4 nm)/Ta (0.8 nm)/CoFeB (1 nm)/MgO (2.5 nm)/Ta (1 nm) stacks, where the Ti layer has much longer spin diffusion length than Ru and can be expected to reduce spin loss and yield higher $\theta_{\mathrm{SH}}^{\mathrm{eff}}$. Figure 4.4(a)-4.4(d) show the R_{AHE} measured with H_{z} and H_{x}, $R_{\mathrm{xy}}^{2\omega}$, and fitting of the sample with a 3 nm-thick Ti layer and BiSb deposited by 10 W (high power). Meanwhile, Figs. 4.5(a)-4.5(d) show those of the sample with the same 3 nm-thick Ti layer but BiSb deposited by 3 W (low power). Both samples show PMA and very strong second harmonic signals, indicating strong SOT effects. Figure 4.6(a) shows H_{AD} as functions of J_{BiSb} in these two samples, from which we estimate $\theta_{\mathrm{SH}}^{\mathrm{eff}} = 2.5\pm0.1$ for BiSb deposited by high power, and $\theta_{\mathrm{SH}}^{\mathrm{eff}} = 6.0\pm0.1$ for BiSb deposited by low power. These values are higher than that of the sample with 3 nm-thick Ru. Furthermore, the $\theta_{\mathrm{SH}}^{\mathrm{eff}}$ of BiSb deposited by lower power is also higher than $\theta_{\mathrm{SH}}^{\mathrm{eff}} = 2.5$ of the MBE-grown $(\mathrm{BiSb})_2\mathrm{Te}_3$/Ti (3 nm)/CoFeB/MgO reported in Ref. 15. Figure 4.6(b) summarizes $\theta_{\mathrm{SH}}^{\mathrm{eff}}$ as a function of the Ti layer thickness t_{Ti}. Again, we observe that 3 nm is the optimized thickness for maximizing $\theta_{\mathrm{SH}}^{\mathrm{eff}}$ of BiSb in these stacks.

4.4 SOT Switching Evaluation

We now perform SOT-induced magnetization switching in the optimized sample with 3 nm-thick Ti and BiSb deposited by low power. Figure 4.7(a) and 4.7(b) show the SOT magnetization switching loops, measured by 50 μs pulse

currents and H_x= ±100 Oe for symmetry-breaking. The switching direction is reversed when the direction of H_x is reversed, indicating the SOT mechanism of magnetization switching. The threshold current density $|J_{th}|$ is $1 \times 10^6 \mathrm{A} \cdot \mathrm{cm}^{-2}$ in BiSb, which is averagely much smaller than those in HMs. Figure 4.7(c) shows SOT magnetization switching loops by 5.0 ms pulse currents under H_x varying from 10 ∼ 100 Oe. We observed full SOT magnetization switching even at the smallest H_x =10 Oe, while the change of $|J_{th}|$ is negligible. Figure 4.8 shows the switching threshold current densityJ_{th} at various current pulse width τ_{pulse}. The red lines are theoretical fitting using the thermal activation model[124]:

$$J_{th} = J_{th}^0 \times \left[1 - \frac{1}{\Delta}\log(\tau_{pulse}/\tau_0)\right], \tag{4.4}$$

where J_{th}^0 is the threshold switching current density at 0 K, Δ is the thermal stability factor which corresponds to the energy barrier of domain wall nucleation in the typical range for PMA in CoFeB/MgO junction with a diameter larger than 40 nm[125, 126, 127] and $\tau_0^{-1} = 1$ GHz ($\tau_0 = 1$ ns) is the attempt switching frequency, respectively.

This fitting yields $J_{th}^0 = 1.5\ \mathrm{MA} \cdot \mathrm{cm}^{-2}$ and $\Delta = 37$, the former is among the smallest for SOT magnetization switching of CoFeB, and the latter is consistent with those reported in literature[125, 126, 127], consolidating the Sb diffusion barrier effect of Ti.

To evaluate and compare the power consumption P_{SOT} of SOT-induced magnetization switching in various SOT material and CoFeB/MgO multilayer system, we use a bilayer model, where we further take into account the shunting current in the FM and the interfacial layers. Here, P_{SOT} is proportional to[117],

$$P_{SOT} \propto \frac{\sigma_{FM}t_{FM} + \sigma_{INT}t_{INT} + \sigma_{SOT}t_{SOT}}{(\sigma_{SOT}t_{SOT}\theta_{SH}^{eff})^2}, \tag{4.5}$$

where σ_{FM}, t_{FM} are the electrical conductivity and thickness of the FM layer, σ_{INT}, t_{INT} are those of the interfacial layers, and σ_{SOT}, t_{SOT} are those of the SOT layer. Table 4.1 summarizes the parameters used for calculation and normalized P_{SOT} for W, Pt, Ta, MBE-grown $(BiSb)_2Te_3$, and our sputtered BiSb in this work. We assume $\sigma_{FM} = 6 \times 10^5\ \Delta^{-1} \cdot m^{-1}$ and $t_{FM} = 1$ nm for CoFeB. For HMs, we use the optimized thickness reported in Ref.[112, 128, 129]

while we use the thickness of 6 nm for $(BiSb)_2Te_3$ reported in Ref. 15, and 10 nm for BiSb. As can be seen in the Table 1, P_{SOT} of BiSb is the smallest thanks to the high effective spin Hall angle (smaller writing current) and high electrical conductivity (less shunting current to other layers), despite having a Ti (3 nm)/Ta (0.8 nm) interfacial layers. We note that the best θ_{SH} obtained so far for BiSb(001) orientation with a single Dirac point at room temperature is about $\theta_{SH} \sim 10$[118], while that of epitaxial BiSb(012) is much higher, reaching $\theta_{SH} = 52$ owing to the high quality and the existence of four Dirac points on the topological surface states[42, 130]. Thus, we can expect a 4 times higher θ_{SH}^{eff} ~ 24 in BiSb(012)/Ti/Ta/CoFeB/MgO. Very recently, we have realized $\theta_{SH}^{eff} \sim$ 22 in BiSb(012)/NiFe by using specially designed buffer layers that promote growth of BiSb(012) and interfacial layers for suppression of Sb diffusion[131].

Table 4.1: Benchmarking of the normalized SOT magnetization switching power consumption P_{SOT} for various HMs and TIs.

SOT Material	W	Pt	Ta	$(BiSb)_2Te_3$ (MBE)	BiSb (sputtered)
Interfacial layers				Ti (2 nm)	Ti (3 nm)/Ta (0.8 nm)
$\lvert\theta_{SH}\rvert$	0.21	0.12	0.15	2.5	6.0
σ_{SOT} $(10^5\Omega^{-1}m^{-1})$	2.7	21	5.6	0.18	1.5
t_{SOT} (nm)	5	5	8	6	10
P_{SOT}	1	2.9×10^{-1}	4.8×10^{-1}	3.5×10^{-1}	8.1×10^{-4}

4.5 Conclusion

In conclusion, we have studied the PMA and SOT characteristics in $Bi_{0.85}Sb_{0.15}$ (001) (10 nm)/Ru(Ti) (1∼4 nm)/Ta (0.8 nm)/$Co_{20}Fe_{60}B_{20}$ (1 nm)/MgO (2.5 nm)/Ta (1 nm) deposited by magnetron sputtering on c-plane sapphire substrates. We found that the highest $\theta_{\mathrm{SH}}^{\mathrm{eff}}$ is obtained when Ru(Ti) buffer layer thickness is 3 nm. Furthermore, by depositing BiSb with a low power, we achieved $\theta_{\mathrm{SH}}^{\mathrm{eff}} = 6.0 \pm 0.1$, which is higher than that of MBE-grown $(BiSb)_2Te_3$. We then demonstrated the full SOT magnetization switching with a small zero Kelvin threshold switching current density of $1.5 \times 10^6\ \mathrm{A \cdot cm^{-2}}$. Our benchmarking shows that the SOT magnetization power consumption in our stack is 2∼3 orders smaller than that in HMs or other TIs. Our results show that sputtered BiSb has the potential for ultrafast and ultralow power SOT-MRAM.

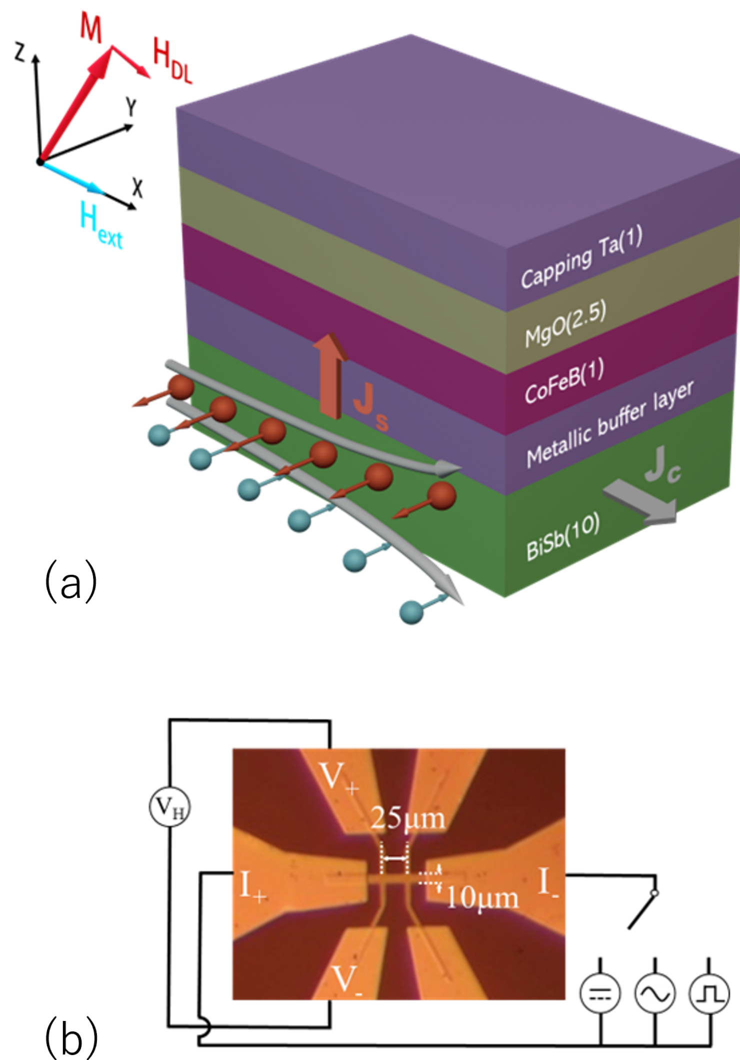

Figure 4.1: (a) Schematic structure of BiSb (10 nm)/metallic interfacial layers of Ru or Ti (1∼4 nm) / Ta (0.8nm) / CoFeB (1 nm) / MgO (2.5nm) / Ta (1 nm) deposited on c-plane sapphire substrates. (b) Optical image of a Hall bar device and experimental setup for measurement of the anomalous Hall effect, second harmonic Hall effect, and SOT-induced magnetization switching.

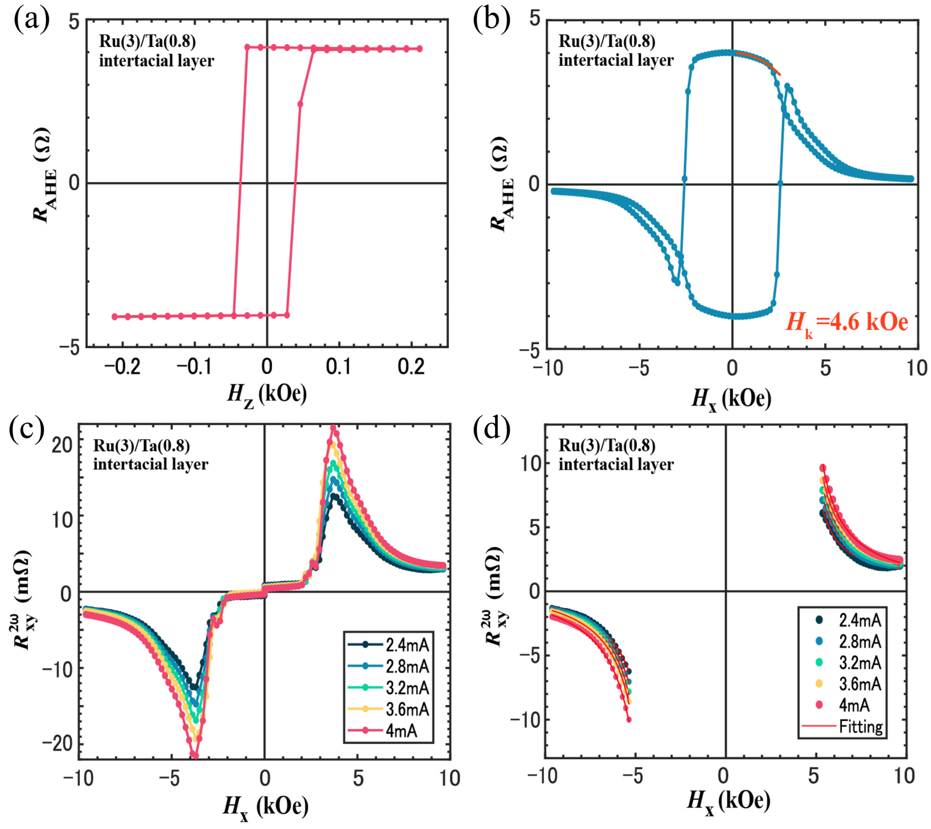

Figure 4.2: (a), (b) Anomalous Hall resistance R_{AHE} of the sample with Ru (3 nm)/Ta (0.8 nm) interfacial layers, measured with an out-of-plane magnetic field H_{z} and an in-plane magnetic field H_{x}. (c), (d) Second harmonic Hall resistance $R_{\mathrm{xy}}^{2\omega}$ as a function of H_{x} at different AC and theoretical fitting using Eq.(1).

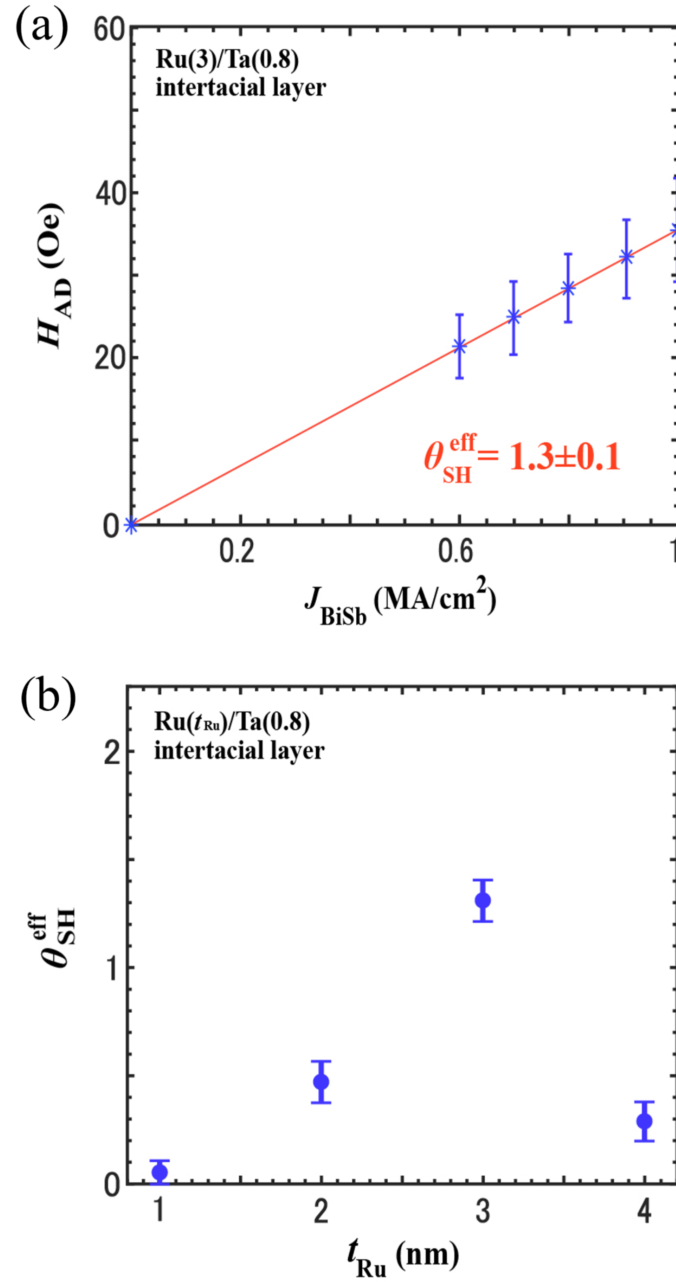

Figure 4.3: (a) Antidamping-like field $H_{\rm AD}$ as a function of $J_{\rm BiSb}$. (b) $\theta_{\rm SH}^{\rm eff}$ as a function of the Ru layer thickness.

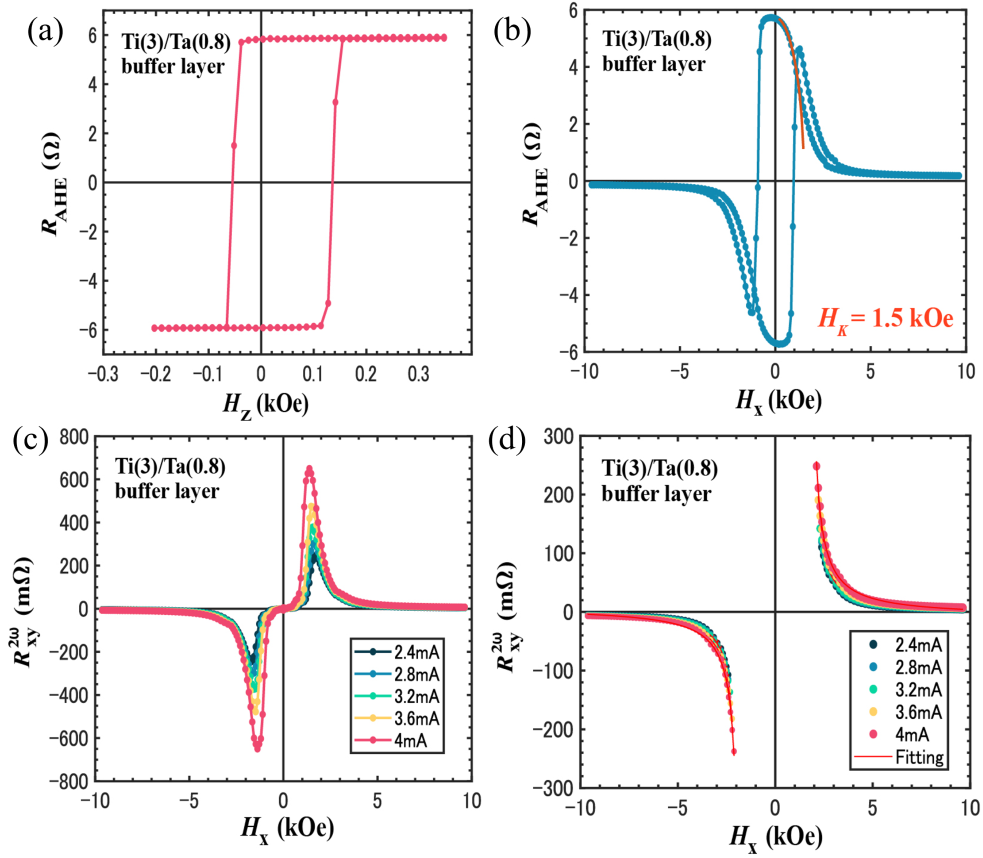

Figure 4.4: (a), (b) Anomalous Hall resistance R_{AHE} of the sample with Ti (3 nm)/Ta(0.8 nm) interfacial layers and BiSb deposited by high power (10 W), measured with an out-of-plane magnetic field H_{z} and an in-plane magnetic field H_{x}. (c), (d) Second harmonic Hall resistance $R_{\mathrm{xy}}^{2\omega}$ as a function of H_{x} at different AC and theoretical fitting using Eq.(1).

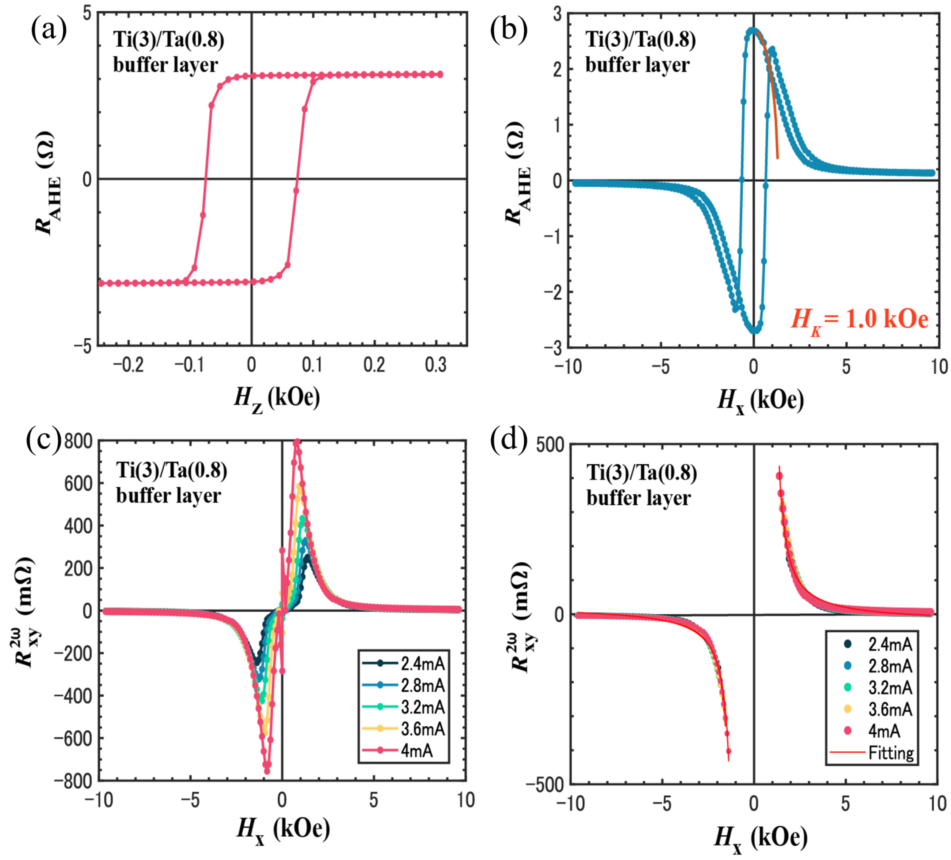

Figure 4.5: (a), (b) Anomalous Hall resistance R_{AHE} of the sample with Ti (3 nm)/Ta(0.8 nm) interfacial layers and BiSb deposited by low power (3 W), measured with an out-of-plane magnetic field H_{z} and an in-plane magnetic field H_{x}. (c), (d) Second harmonic Hall resistance $R_{\mathrm{xy}}^{2\omega}$ as a function of H_{x} at different AC and theoretical fitting using Eq.(1).

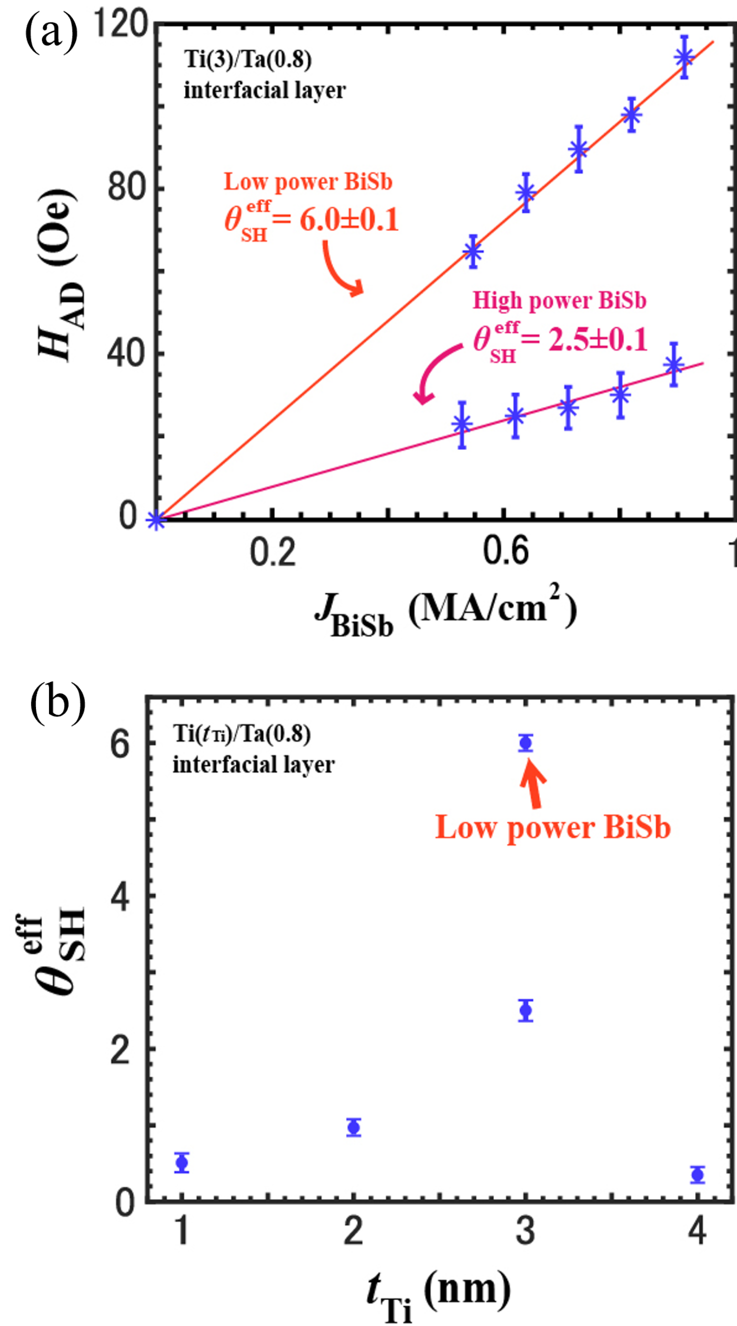

Figure 4.6: (a) H_{AD} as functions of J_{BiSb} for these two samples. (b) $\theta_{\mathrm{SH}}^{\mathrm{eff}}$ as a function of the Ti layer thickness.

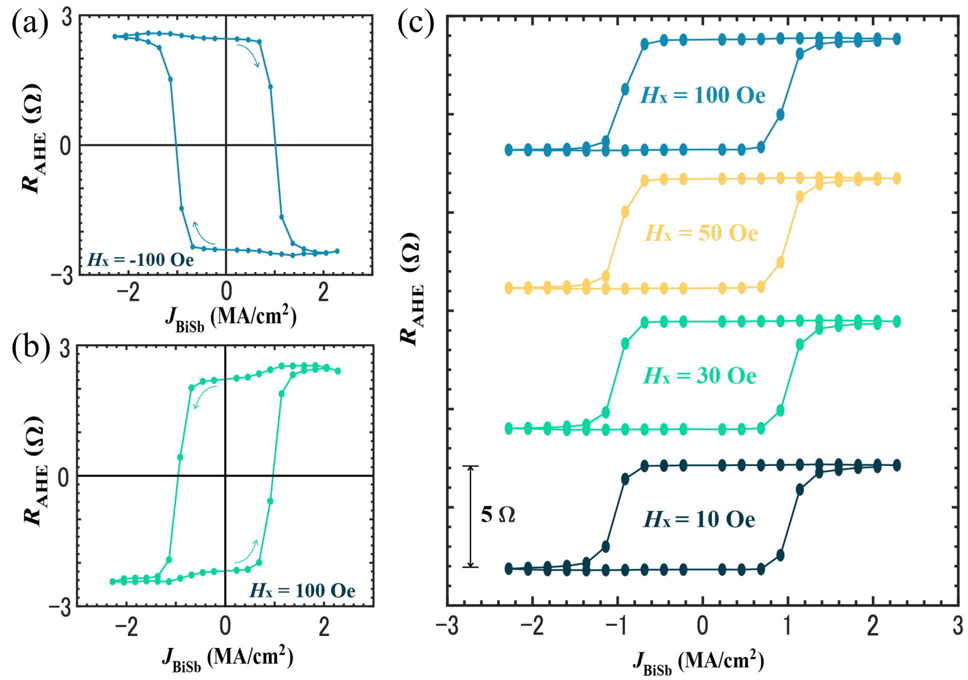

Figure 4.7: (a) (b) SOT magnetization switching loops induced by 50 µs pulse currents under H_x of 100 Oe applied along -x direction and +x direction, respectively. (c) SOT magnetization switching loops by 5.0 ms pulse currents measured under various H_x = 10, 30, 50, and 100 Oe.

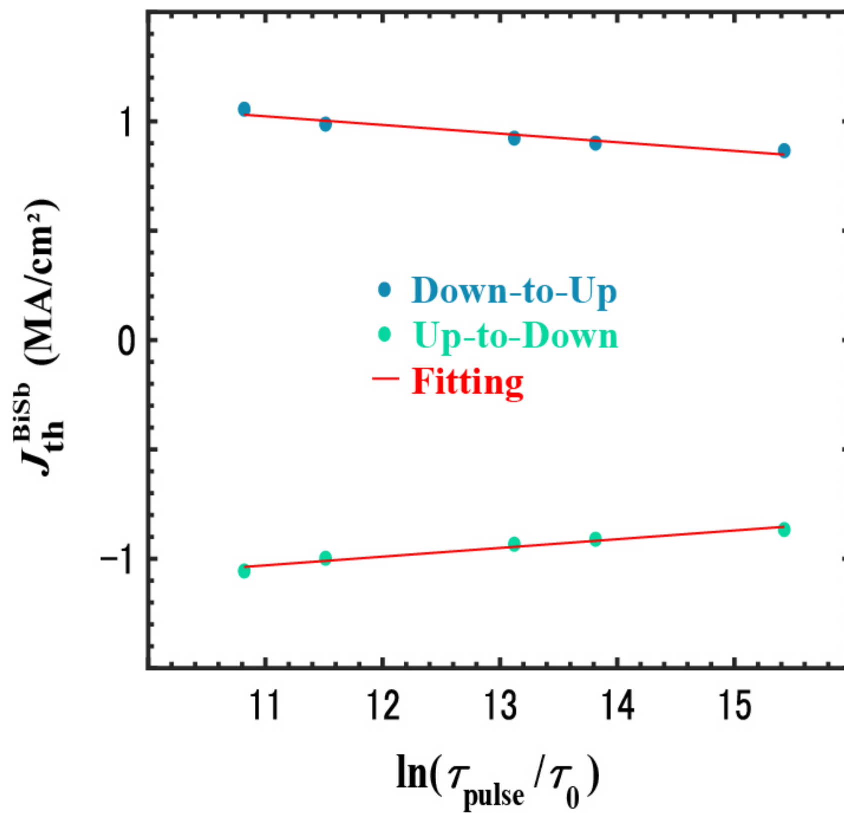

Figure 4.8: Threshold switching current density as a function of current pulse width τ_{pulse}. Red solid lines are fitting using the thermal activation model.

Chapter 5

Giant perpendicular magnetic anisotropy in Mo/Boron-rich CoFeB/$MgAl_2O_4$ structure

5.1 Background

5.1.1 Quantification of Magnetic anisotropy

A storage layer magnetized perpendicular to the plane generally offers better thermal stability at smaller sizes compared to in-plane magnetized layers, due to its significantly higher intrinsic anisotropy. This advantage was a key factor behind the hard disk drive industry's transition from in-plane magnetized media to perpendicular media in 2004, as well as the choice of PMA-MTJ for MRAM technology below the 32 nm scale. Perpendicular magnetic anisotropy (PMA) in thin film magnetic materials can arise from various sources. One such source is the bulk of the material itself, as seen in FePt or FePd L10 ordered alloys, where a tetragonal distortion of the lattice cell along the growth direction induces anisotropy. This bulk anisotropy, denoted as K_{b}, is typically expressed as an energy density measured in joules per cubic meter ($\mathrm{J{\cdot}m^{-3}}$).

$$E^{\mathrm{Bulk}}_{\mathrm{anisotropy}} = -K_{\mathrm{b}}(\hat{n} \cdot \vec{M})^2, \tag{5.1}$$

where $\hat{n}$ is a unit vector normal to the plane of the layer. The PMA may also be of interfacial origin due to interfacial electron hybridization[132] or interfacial stress[133]. This interfacial PMA is usually expressed in terms of a volume energy (in J·m^{-3}) as

$$E_{\text{anisotropy}}^{\text{Interface}} = -\frac{K_{\text{i}}}{t}(\hat{n} \cdot \vec{M})^2, \tag{5.2}$$

Here, K_{i} represents the surface energy (in J·m^{-2}), and t_{eff} denotes the thickness of the storage layer without the part of magnetic dead layer (MDL) thickness. However, this perpendicular magnetic anisotropy (PMA) is partially offset by the demagnetizing energy, which is the magnetostatic energy cost associated with pulling the magnetization of a thin film out of the plane. For a thin magnetic film situated between two interfaces, the anisotropy is typically described as an effective anisotropy per unit volume. From a purely magnetostatic perspective, the thickness of a magnetic thin film is usually its smallest dimension, making the direction along the thickness the hard axis of magnetization. Therefore, if the magnetization is nevertheless oriented out of the plane due to other anisotropy sources, these sources must overcome the demagnetizing energy. For an extended thin film, the demagnetizing energy per unit volume is expressed as follows:

$$E_{\text{demagnetizing}} = +\frac{1}{2}\mu_0 M_{\text{S}}^2(\hat{n} \cdot \vec{M})^2. \tag{5.3}$$

$$E_{\text{anisotropy}} = E_{\text{anisotropy}}^{\text{Bulk}} + E_{\text{anisotropy}}^{\text{Interface}} + E_{\text{demagnetizing}} = K_{\text{eff}} \cdot (\hat{n} \cdot \vec{M})^2 \tag{5.4}$$

$$K_{\text{eff}} = \left(K_{\text{b}} - \frac{\mu_0}{2}M_{\text{S}}^2\right) + \frac{K_{\text{i}}}{t_{\text{eff}}}, \tag{5.5}$$

where K_{b} accounts for all the material bulk anisotropy contributions, $-\frac{\mu_0}{2}M_{\text{S}}^2$ represents the demagnetizing energy, K_{i} combines all the interfacial contributions from the two interfaces and K_{eff} is the total effective anisotropy. Experimentally, the product K_{eff} can be plotted against effective magnetic film thickness t_{eff} to determine the various contributions. The slope of this curve represents the overall bulk anisotropy, while the point where it intersects the vertical axis indicates the total interfacial anisotropy.

5.1.2 Motivation

The CoFeB/MgO-based MTJ is used to achieve both PMA and high tunneling magnetoresistance (TMR) ratio[134], which is usually annealed at 250 $\sim$ 400 °C so that CoFeB is crystallized into the bcc CoFe phase induced by the cubic MgO template[135]. According to the first principle calculation, Fe-O with hybridizations between Fe-3d and O-2p orbitals at the interface of CoFeB/MgO plays a more critical role than the Co-O bonding for PMA[136, 63], which explains the experimental results that Fe-rich CoFeB has larger PMA than the Co-rich case[137]. Moreover, over- or underoxidized MgO interfaces may weaken PMA[138]. To optimize the performance of CoFeB/MgO used in p-MTJs below 30 nm device diameter, CoFeB element composition ratio[139, 140], interfacial PMA[47, 136, 141], shape anisotropy[142, 143], atomic-scale structure and local chemistry[144], annealing temperature (T_{an})[145], buffer layer material/thickness[141, 146, 147], and element diffusion[148, 149], and multi CoFeB/MgO interfaces [150] have been intensively studied.

During annealing, Boron (B) in CoFeB may behave differently depending on the underlayer. For example, in a typical stack consisting of amorphous Ta/CoFeB/MgO, it has been shown that most of Boron diffuses into Ta, thus Ta is a good Boron getter for CoFeB[144]. However, one of the most serious problems for the Ta/CoFeB/MgO system is that the PMA is degraded and eventually disappears during 400 °C post-annealing, which is required for back-end-of-line (BEOL) CMOS manufacturing. Stacks of Ta (3 $\sim$ 10 nm)/CoFeB (0.7 $\sim$ 1.8 nm)/MgO show degradation of saturation magnetization (M_{s}) and magnetic anisotropy energy density when the annealing temperature T_{an} is over 250 °C, and PMA is lost when T_{an} is over 350 °C[51, 52, 53, 54, 55]. It was then found that Mo underlayer/CoFeB/MgO could keep PMA after 400 °C annealing and showed an interfacial PMA 20% higher than Ta/CoFeB/MgO[56]. Other examples of underlayers for maintaining PMA at $T_{\mathrm{an}} \sim 400$ °C are Hf and Mo/Hf multilayers[57, 58]. Despite those efforts, the magnetic anisotropy field H_{k} of a bottom CoFeB/MgO single interface is still about 4 $\sim$ 6 kOe, and the corresponding magnetic anisotropy energy constant K_{eff} is about $3 \times 10^6 \sim 5 \times 10^6$ erg $\cdot$ cm^{-3}. Therefore, the minimum size of MTJ devices with a single CoFeB layer and a thermal stability factor Δ of at least 60 for 10-year retention is about 29 nm, which can be

integrated up to the CMOS process of 16 nm. For further device size scaling and better resistance against thermal and external magnetic field disturbance, it is essential to enhance the PMA of CoFeB.

In this study, we aim to realize a giant PMA in Mo (2 nm)/$Co_{19}Fe_{56}B_{25}$ (t_{CoFeB})/$MgAl_2O_4$ (4 nm)/Ta (1 nm). By using the B-rich $Co_{19}Fe_{56}B_{25}$ layer in combination with the Mo underlayer and the spinel $MgAl_2O_4$ (4 nm) oxide layer, we achieve giant PMA in CoFeB, with maximum H_k ranging from 17.5 to 19.5 kOe, and maximum K_{eff} ranging from $6.9 \times 10^6 \sim 9.4 \times 10^6$ erg $\cdot$ cm^{-3}. Our results pave the way for further scaling of MTJs and improved resistance to thermal and external magnetic field disturbances.

5.2 Film Stacks Deposition and Strategy for PMA enhancement

Film stacks were deposited using a magnetron sputtering system with a base pressure of 7.0×10^{-7} Pa on sapphire substrates. The surface of sapphire is very smooth, allowing us to deposit our stacks with a thin and smooth Mo directly on the substrates without using a buffer layer. We prepared two series of multilayers. Samples A1 $\sim$ A10 consisting of, from the substrates, Mo (2 nm)/$Co_{19}Fe_{56}B_{25}$ ($t_{CoFeB} = 0.7 \sim 2.0$ nm) / $MgAl_2O_4$ (4 nm)/Ta (1 nm), were post-annealed at 300 °C for 30 minutes in vacuum. Samples B1 $\sim$ B10 consisting of the same Mo (2 nm)/$Co_{19}Fe_{56}B_{25}$ ($t_{CoFeB} = 0.7 \sim 2.0$ nm)/$MgAl_2O_4$ (4 nm)/Ta (1 nm) stacks, were annealed at 300 °C for 30 minutes and then further annealed at 400 °C for another 30 minutes in vacuum. We also fabricated a reference sample C consisting of Mo (2 nm)/$Co_{19}Fe_{56}B_{25}$ (1 nm)/MgO (2.5 nm)/Ta (1 nm) on a Si/SiO_2 substrate, and annealed this sample by the same manner as samples B. Magnetic properties were characterized by a superconducting quantum interference device (SQUID). We fabricated Hall bar devices with size of 10×25 μm^2 for magnetotransport measurement using the four-probe method. Finally, we used Auger electron spectroscopy (AES) to characterize element distribution in the film stacks.

We first discuss the strategy to enhance K_{eff} and H_k of CoFeB, which are

given by formula (5.5) and (5.6):

$$H_{\mathrm{k}} = \frac{2K_{\mathrm{eff}}}{M_{\mathrm{S}}}, \tag{5.6}$$

where the H_{k} and M_{S} is magnetic anisotropy field and saturation magnetization, respectively. To enhance K_{eff} and H_{k}, most research has been focused so far on enhancing K_{i}. However, a sizable enhancement of K_{i} is difficult. Instead, our strategy is to reduce M_{S}, which has a more pronounced effect on both K_{eff} and H_{k}. Thus, the key factor to achieve giant PMA in this work is the use of B-rich $Co_{19}Fe_{56}B_{25}$ embedded between a Boron-blocking Mo underlayer and $MgAl_2O_4$ oxide to yield a low M_{S}. Here, we focus on the spinel $MgAl_2O_4$ oxide layer rather than MgO, since $MgAl_2O_4$ based MTJs are considered to be superior to MgO-based ones with regard to their lattice-matching with Fe-based and CoFe-based ferromagnets for the (001) epitaxial growth, which may lead to enhancement of the TMR ratio[151, 152, 153, 154]. Indeed, it was reported that $Fe_{0.5}Co_{0.5}/MgAl_2O_4/Fe_{0.5}Co_{0.5}$ can reach a high TMR ratio of 308% at room temperature[155]. Furthermore, $MgAl_2O_4$-based MTJs show improved bias voltage dependence of the TMR ratio[156].

5.3 PMA Evaluation

Figures 5.1(a) and (b) show the normalized anomalous Hall resistance $R_{\mathrm{AHE}}^{\mathrm{N}}$ for samples A1 $\sim$ A7 and B1 $\sim$ B8 with PMA, measured with an in-plane magnetic field H_{x}. To estimate H_{k}, we fitted the low-field data by

$$R_{\mathrm{AHE}}^{\mathrm{N}} = \sqrt{1 - \left(\frac{H_{\mathrm{x}}}{H_{\mathrm{k}}}\right)^2}. \tag{5.7}$$

For the two most important samples A2 and B2 with the highest H_{k}, we measured the anomalous Hall resistance with an in-plane magnetic field in the range of ± 14.5 kOe, and fitted the data for the full range to precisely estimate H_{k} (see Fig. 5.3). Samples A2 and B2 with $t_{\mathrm{CoFeB}} = 0.8$ nm show a giant $H_{\mathrm{k}} = 17.5$ and 19.5 kOe, respectively, which are much larger than the typical $H_{\mathrm{k}} = 4 \sim 6$ kOe observed so far in CoFeB/MgO or CoFeB/$MgAl_2O_4$ systems. From sample A2 to A7 and from B2 to B8, H_{k} decreases as t_{CoFeB}

increases from 0.8 nm to 1.3 nm and 1.6nm, respectively. Comparing samples A1 $\sim$ A7 and B1 $\sim$ B7, we observe that all of their H_k are enhanced after the 400°C annealing. Notably, sample A1 with $t_{\text{CoFeB}} = 0.7$ nm has a low H_k of 4 kOe, but it increases to 16 kOe for the sample B1 after the additional 400°C annealing. Figures 5.2(a) and (b) show $R^{\text{N}}_{\text{AHE}}$ for samples A7 $\sim$ A10 and B7 $\sim$ B10 measured with an out-of-plane magnetic field H_z. We observe that CoFeB shows PMA up to at least $t_{\text{CoFeB}} = 1.6$ nm.

Figure 5.4(a) shows the saturation magnetic moment per unit area $M_S{\cdot}t_{\text{CoFeB}}$ for samples A and B, plotted as a function of t_{CoFeB}. The solid and dashed lines are linear fitting for estimation of the magnetic dead layer (MDL) thickness t_d and the average volume saturation magnetization M_S from the intercept to the x-axis and the slope of the fitted lines. The average M_S decreases from 1079 $\text{erg} \cdot \text{cm}^{-3}$ (samples A2 $\sim$ A10) to 711 $\text{erg} \cdot \text{cm}^{-3}$ (all samples B) after 30 minutes of 400°C annealing. For sample A1 with $t_{\text{CoFeB}} = 0.7$ nm, M_S is only 656 $\text{erg} \cdot \text{cm}^{-3}$ which deviates significantly from the linear region. The MDL thickness of samples A is $t_d = 0.9$ Angstrom. Meanwhile, for sample B1, M_S is still in the linear region with H_k four times of that of sample A1. This observation is also aligned with the fact that there is no MDL in samples B with $t_d = 0$ Angstrom.

Figure 5.4(b) shows the t_{eff} dependence of the product $K_{\text{eff}} \sim t_{\text{eff}}$ for samples A and B, where $t_{\text{eff}} = t_{\text{CoFeB}}$ - t_d. The maximum $K_{\text{eff}} \sim t_{\text{eff}}$ was observed for sample A2 at $t_{\text{eff}} = 0.71$ nm ($t_{\text{CoFeB}} = 0.8$ nm) and sample B2 at $t_{\text{eff}} = t_{\text{CoFeB}}$ $= 0.8$ nm with maximum H_k values of 17.5 kOe and 19.5 kOe, respectively. The solid and dashed lines in Fig. 5.4(b) are linear fitting for estimation of K_i from their intercepts to the y-axis, which yield $K_i \approx 1.5$ $\text{erg} \cdot \text{cm}^{-2}$ for samples A and $K_i \approx 1.2$ $\text{erg} \cdot \text{cm}^{-2}$ for sample B. Table 5.1 compares the stack structure, average M_S, the highest H_k, the highest K_{eff}, K_i, and t_d observed in Ta/CoFeB/$MgAl_2O_4$[151], Ta/CoFeB/MgO and Mo/CoFeB/MgO[56], and samples A and B in this work.

One can see that there are two distinct features of our samples compared to the literature: the very large maximum H_k of 17.5 $\sim$ 19.5 kOe and the very large maximum K_{eff} of $6.9 \times 10^6 \sim 9.4 \times 10^6$ $\text{erg} \cdot \text{cm}^{-3}$. Furthermore, $K_i \approx 1.5$ $\text{erg} \cdot \text{cm}^{-2}$ of samples A is higher than $K_i \approx 1.3$ $\text{erg} \cdot \text{cm}^{-2}$ of the Ta/CoFeB/$MgAl_2O_4$ stack annealed at the same temperature of 300 °C, con-

sistent with the previous observation that the Mo underlayer yields higher K_i than the Ta underlayer in CoFeB/MgO junctions[56].

Table 5.1: Magnetic properties of M_S, highest H_k, highest K_eff, K_i and t_d and sample structures

Sample structure and T_an	$\boldsymbol{M_\mathrm{s}}$ **(emu·cm^{-3})**	**Highest $\boldsymbol{H_\mathrm{k}}$ (kOe)**	**Highest $\boldsymbol{K_\mathrm{eff}}$ (10^6 erg·cm^{-3})**	$\boldsymbol{K_\mathrm{i}}$ **(erg·cm^{-2})**	$\boldsymbol{t_\mathrm{d}}$ **(nm)**
Ta(5)/CoFeB/$MgAl_2O_4$(2)/Ta(5), T_an = 300°C (Ref.[151])	1751	4.5	3.9	1.3	0.26
Ta(5)/$Co_{40}Fe_{40}B_{20}$/MgO(2)/Ta(5), T_an = 300°C (Ref.[56])	1600	3.5	2.8	1.7	0.45
Mo(5)/$Co_{40}Fe_{40}B_{20}$/MgO(2)/Mo(5), T_an = 425°C (Ref.[56])	1600	6.0	4.8	2.0	0
Mo(2)/$Co_{19}Fe_{56}B_{25}$/$MgAl_2O_4$(4)/Ta(1), T_an = 300°C (This work)	1079	17.5	9.4	1.5	0.09
Mo(2)/$Co_{19}Fe_{56}B_{25}$/$MgAl_2O_4$(4)/Ta(1), T_an = 400°C (This work)	711	19.5	6.9	1.2	0

However, K_i of our Mo/CoFeB/$MgAl_2O_4$ is lower than $K_\mathrm{i} \approx 2.0$ erg $\cdot$ cm^{-2} and $K_\mathrm{i} \approx 1.7$ erg·cm^{-2} observed in Mo/CoFeB/MgO and Ta/CoFeB/MgO[56]. This may be due to the general trend that CoFeB/$MgAl_2O_4$ has a lower K_i than CoFeB/MgO, or due to the less concentration of Co/Fe in the Boron-rich CoFeB in this work. Since the K_i in our stack is not particularly large, the observed very large PMA does not originate from the enhanced K_i. Instead, it comes from the low demagnetization energy owing to the small M_S.

5.4 Auger Electron Spectroscopy (AES) Evaluation

To qualitatively investigate the atomic distribution in our samples, we employ the AES technique, which is implemented with an in-situ ion milling gun operating in an Ar gas environment. The etching spot size is about 100 μm^2. We normalized the AES intensity depth profile for better visualization. Figures 5.5(a) and 5.5(b) show the normalized AES intensity depth profile for sample A2 and B2, respectively. The color arrows indicate the central positions of each element. When there were multiple peaks in the AES signals, we deconvolated the AES signals (dashed lines) and assigned arrows to the local peaks. For example, there are two arrows for oxygen (O), which are at the center of the oxidized Ta cap layer and the $MgAl_2O_4$ layer. In both samples

A2 and B2, it's very clear that Boron diffused to the $MgAl_2O_4$ and partly to the oxidized Ta cap. There are still about 20% of the original Boron atoms remaining inside the CoFeB layer, which explains the small M_S.

Furthermore, the Mo underlayer effectively blocked Boron diffusion toward the substrate. Comparing sample A2 and B2, we found that there was no significant difference in the distribution of Fe, Co, Mg, Al, and O, and the interfaces between $MgAl_2O_4$/CoFeB/Mo remained relatively sharp. However, in sample B2, Boron diffused more to the oxidized Ta cap, as the AES peak intensity of Boron inside the oxidized Ta cap is now close to that inside $MgAl_2O_4$. There are several possible reasons for the observed Boron diffusion. First, the Mo thin film with a nanometer thickness is relatively easy to crystallize even at room temperature deposition[157]. Second, transmission electron microscope and electron energy loss spectroscopy analysis have shown that Boron tends to diffuse into non-crystalline region such as amorphous Ta, or grain boundaries in MgO[149, 158]. Thus, the well-crystallized Mo layer with smaller surface energy is good at blocking Boron diffusion. Meanwhile, $MgAl_2O_4$ was shown to grow with columnar structures during deposition with grain boundaries[159]. Such intercolumnar grain boundaries can provide channels for the diffusion of light elements such as Boron. Because there is always broadening in AES signals, it is difficult to discuss qualitatively the level of mixing at the interface of each layer in Mo/CoFeB/$MgAl_2O_4$ stack.

However, one can see from the Fig. 5.5 that (1) Boron atoms are effectively blocked by the Mo underlayer and diffuse upward to the $MgAl_2O_4$ layer, likely through the intergranular boundary channels in $MgAl_2O_4$, and (2) the interface between Mo/CoFeB is clear and sharp. These results are consistent with the negligible MDL in Mo/CoFeB ($t_d < 0.1$ nm), compared with the large MDL in Ta/CoFeB as summarized in Table 5.1. The tendency of blocking atomic diffusion, low intermixing, and the long spin diffusion length of Mo are also very beneficial for use as an interlayer between a ferromagnetic layer and a spin Hall layer composed of a heavy metal, a topological insulator[42, 121, 120, 160] or topological semimetal[161, 162], for spin-orbit torque (SOT)-MRAM and SOT magnetic sensor[49, 163].

It is worth noting that the amount of Boron remaining in CoFeB is important for the observed giant PMA. If the amount of Boron remaining in CoFeB

is too high, the giant PMA cannot be obtained. For this reason, $MgAl_2O_4$ also plays an important role: it provides a reasonable sink for Boron as shown in Fig. 5.5. The good balance between the Boron-blocking Mo layer and the Boron-sink $MgAl_2O_4$ layer results in about 20% of the original Boron remaining in CoFeB, leading to a small M_S and giant PMA. We also prepared reference samples C1 and C2 consisting of Ta (3 nm)/CoFeB (0.8 nm)/$MgAl_2O_4$(4 nm)/Ta(1 nm). The sample C1 was annealed at 300 °C for 30 minutes, and the sample C2 was annealed at 300 °C for 30 minutes followed by an additional 400 °C annealing for 30 minutes. PMA survived in sample C1 but it was destroyed in sample C2. Figures 5.6(a) and 5.6(b) show the normalized AES profiles for the reference samples C1 and C2. We observed that B diffused down to the Ta underlayer, similar to the case of Ta/CoFeB/MgO. Importantly, Ta significantly intermixed with CoFeB, resulting in a strong intermixing layer at the Ta/CoFeB interface. In sample C2, the AES intensity peak of Ta shifts upward, approaching that of CoFeB. Such Ta diffusion into CoFeB can interfere with the interfacial magnetic anisotropy and may explain the total loss of PMA in sample C2.

By comparing Figs. 5.5(a)(b) with Figs. 5.6(a)(b), one can see that (1) B atoms are tend to diffuse to the Ta underlayer unlike the B blocker effect for Mo seed layer, and (2) the interface between Mo/CoFeB is clearer and sharper than the Ta/CoFeB interface. The latter also has significant Ta diffusion to the inside of CoFeB. These results are consistent with the large MDL in Ta/CoFeB as summarized in Table 5.1.

We also deposited a reference stack C3 consisting of Mo (2 nm)/$Co_{19}Fe_{56}B_{25}$ (1 nm)/MgO (2.5 nm)/Ta (1 nm) on a Si/SiO_2 substrate, and found that MgO is not a good sink for Boron. As a result, a large amount of Boron (about 60% of the original Boron) remained in CoFeB even after 400 °C annealing, as shown in its AES intensity depth profile in Fig. 5.7(a). Consequently, H_k of this stack was only 5 kOe, as shown in Fig. 5.7(b). This is likely due to weak interfacial PMA at the CoFeB/MgO interface when a large amount of B remains in the CoFeB layer. Therefore, both Mo and $MgAl_2O_4$ are important for achieving a reasonable amount of B remaining in CoFeB and the giant PMA in this work.

5.5 Discussion

We note that the $K_{\mathrm{eff}} = 9.4 \times 10^6$ erg $\cdot$ cm^{-3} obtained at $t_{\mathrm{eff}} = 0.71$ nm is the highest K_{eff} reported so far for a single layer of CoFeB. This value is nearly double that of the typical K_{eff} value of conventional CoFeB/MgO. Therefore, the minimum diameter of MTJ devices with a single CoFeB and a thermal stability factor Δ of at least 60 can be reduced to 22 nm, which can be integrated to the 7 nm CMOS process. The bit density can be nearly doubled. To further reduce the MTJ diameter size, it is essential to increase the effective thickness of CoFeB without sacrificing K_{eff}. To demonstrate this concept, we fabricated double layers of CoFeB in a stacking structure of Mo (1 nm)/$Co_{19}Fe_{56}B_{25}$ (0.8 nm)/Mo (0.4 nm)/$Co_{19}Fe_{56}B_{25}$ (0.8 nm)/ $MgAl_2O_4$ (4 nm)/Ta (1 nm) as shown in Fig. 5.8. In this double CoFeB layer structure, each of the B-rich CoFeB layer faces Mo and $MgAl_2O_4$.

Furthermore, they can be ferromagnetically coupled through the middle Mo (0.4 nm). Figure 5.9(a) and 5.9(b) show the anomalous Hall resistance of a Hall bar device of this stack, measured with an out-of-plane and in-plane magnetic field, respectively. The stack was annealed at 400 °C for 30 minutes. In Fig. 5.9(a), we observe a coherent magnetization reversal of the double CoFeB layers, indicating that they are ferromagnetically coupled through the Mo (0.4 nm). The red line in the Fig. 5.9(b) is a fitting curve for estimation of H_{k}, which yields a giant $H_{\mathrm{k}} = 17$ kOe, similar to that observed in a single Mo/CoFeB/$MgAl_2O_4$. By comparing the Fig 5.9(a) and Fig 5.10(a) and 5.10(b), one can see, the double layer CoFeB structure has a higher H_{c} (over 150 Oe) than that (less than 60 Oe) in single layer CoFeB sample annealed at the same 400 °C. Thus, we concluded that even a very thin Mo (0.4 nm) and $MgAl_2O_4$ (1 nm) are effective for generating giant PMA. Using this kind of double layers, the minimum diameter of MTJ can be further reduced for use in more advanced CMOS process.

5.6 Conclusion

In conclusion, by using B-rich $Co_{19}Fe_{56}B_{25}$ in Mo/CoFeB/$MgAl_2O_4$, we have realized giant PMA with H_{k} of 17.5 $\sim$ 19.5 kOe, and K_{eff} of $6.9 \times 10^6 \sim$

9.4×10^6 erg $\cdot$ cm^{-3}. The giant PMA originates from the low demagnetization energy owing to the small M_s of B-rich $Co_{19}Fe_{56}B_{25}$ exposed to 300 °C and 400 °C annealing. The MDL in our samples is negligible ($<$ 0.1 nm). AES measurements show that the Mo underlayer effectively blocks Boron diffusion and has clean and sharp interface with CoFeB, while $MgAl_2O_4$ provides a reasonable sink for Boron. The good balance between the Boron-blocking Mo layer and the Boron-sink $MgAl_2O_4$ layer results in about 20% of the origin Boron remaining in CoFeB, leading to a small M_S and giant PMA. We also demonstrated double CoFeB layers with giant PMA for use in more advanced CMOS process. Our results provide a recipe for designing MTJ with improved resistance against thermal and external magnetic field disturbance for further device size scaling.

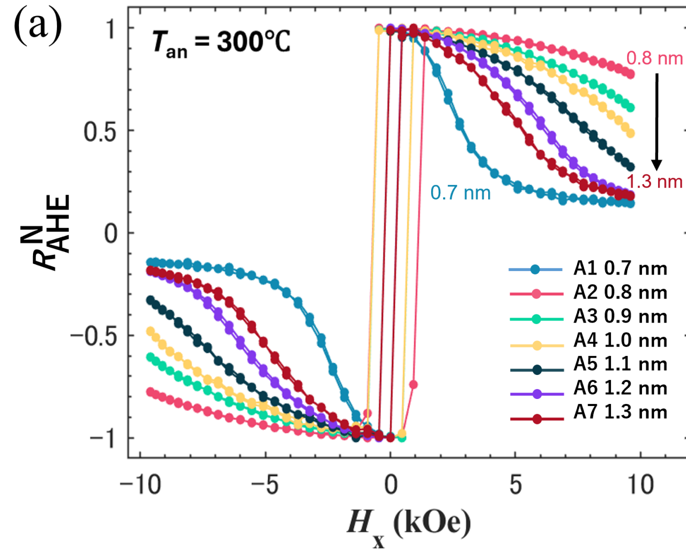

(a) Samples A1 $\sim$ A7 ($t_{\mathrm{CoFeB}} = 0.7 \sim 1.3$ nm) measured with an in-plane magnetic field H_{x}.

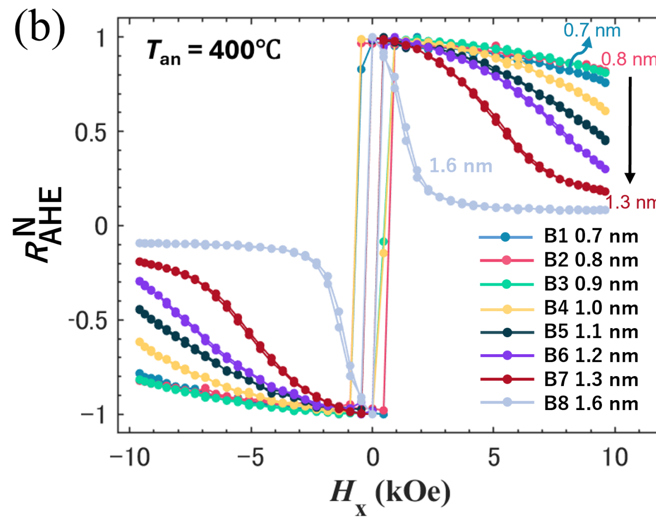

(b) Samples B1 $\sim$ B8 ($t_{\mathrm{CoFeB}} = 0.7 \sim 1.6$ nm) measured with an in-plane magnetic field H_{x}.

Figure 5.1: Normalized anomalous Hall resistance $R^{\mathrm{N}}_{\mathrm{AHE}}$ of Mo (2 nm)/$Co_{19}Fe_{56}B_{25}$ ($t_{\mathrm{CoFeB}} = 0.7 \sim 1.6$ nm)/$MgAl_2O_4$ (4 nm)/Ta (1 nm) multilayers subjected to annealing at 300°C for 30 minutes (sample A) and those with an additional 400°C annealing for 30 minutes (sample B).

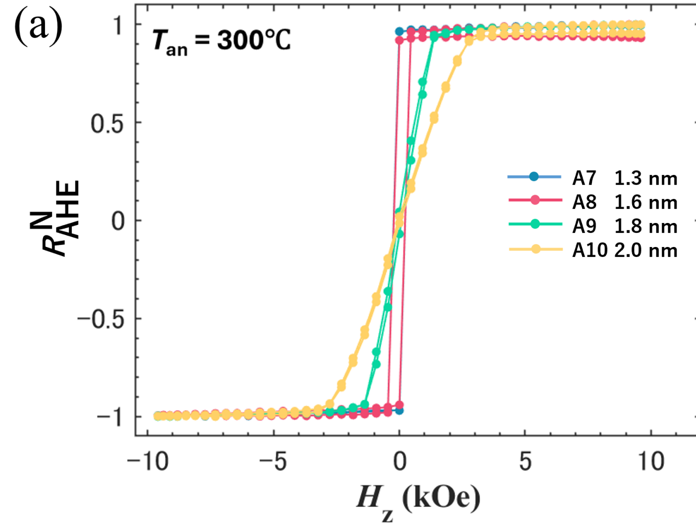

(a) Samples A7 ∼ A10 ($t_{\mathrm{CoFeB}} = 1.3 \sim 2.0$ nm) measured with an out of plane magnetic field H_z.

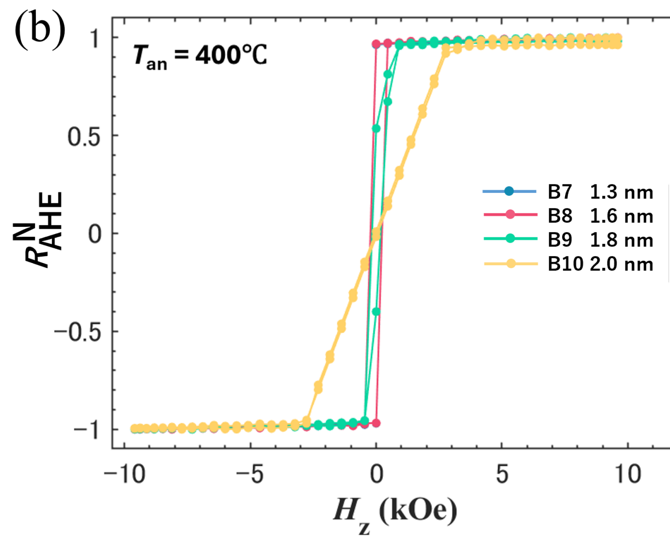

(b) Samples B7 ∼ B10 ($t_{\mathrm{CoFeB}} = 1.3 \sim 2.0$ nm) measured with an out of plane magnetic field H_z.

Figure 5.2: Normalized anomalous Hall resistance $R^{\mathrm{N}}_{\mathrm{AHE}}$ of Mo (2 nm)/$Co_{19}Fe_{56}B_{25}$ ($t_{\mathrm{CoFeB}} = 1.3 \sim 2.0$ nm)/$MgAl_2O_4$ (4 nm)/Ta (1 nm) multilayers subjected to annealing at 300°C for 30 minutes (sample A) and those with an additional 400°C annealing for 30 minutes (sample B).

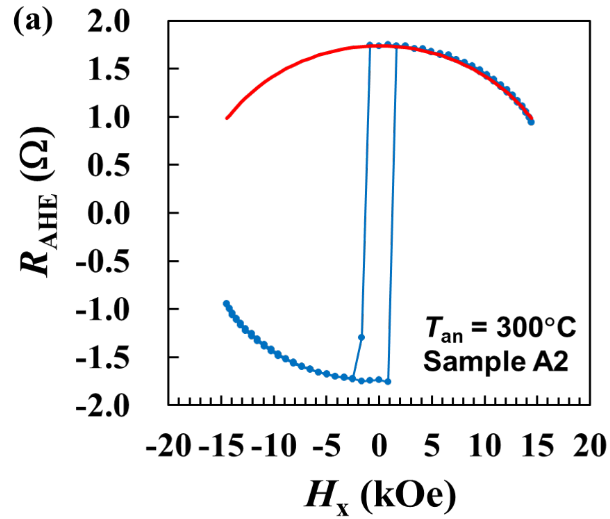

(a) Samples A2 ($t_{\text{CoFeB}} = 0.8$ nm) measured with an in-plane magnetic field H_{x}.

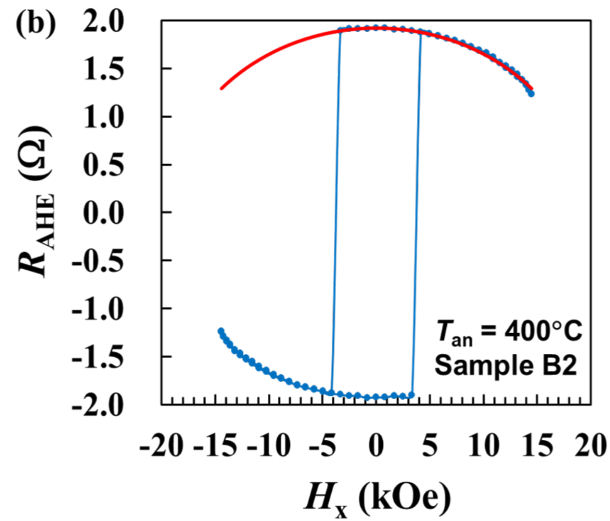

(b) Samples B2 ($t_{\text{CoFeB}} = 0.8$ nm) measured with an in-plane magnetic field H_{x}.

Figure 5.3: Anomalous Hall resistance R_{AHE} of Mo (2 nm)/$Co_{19}Fe_{56}B_{25}$ ($t_{\text{CoFeB}} = 0.8$ nm)/$MgAl_2O_4$ (4 nm)/Ta (1 nm) multilayers subjected to annealing at 300°C for 30 minutes (sample A2) and that with an additional 400°C annealing for 30 minutes (sample B) measured with an in-plane magnetic field in the range of -14.5 kOe to + 14.5 kOe. The red curves are fitting curves to precisely estimate H_{k}.

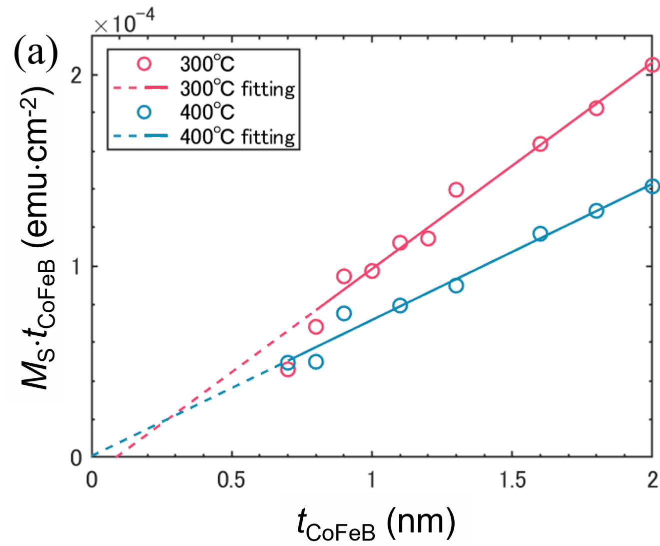

(a) Saturation magnetic moment per unit area $M_{\mathrm{S}} \cdot t_{\mathrm{CoFeB}}$ as a function of thickness of CoFeB for samples A and B.

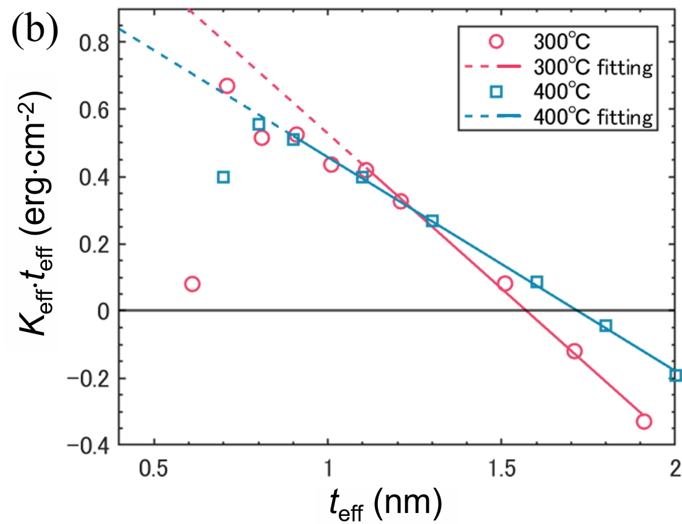

(b) Product of perpendicular anisotropy K_{eff} and effective thickness t_{eff} for samples A and B. Solid and dashed lines are linear fitting.

Figure 5.4: Linear fitting calculation for magnetic properties.

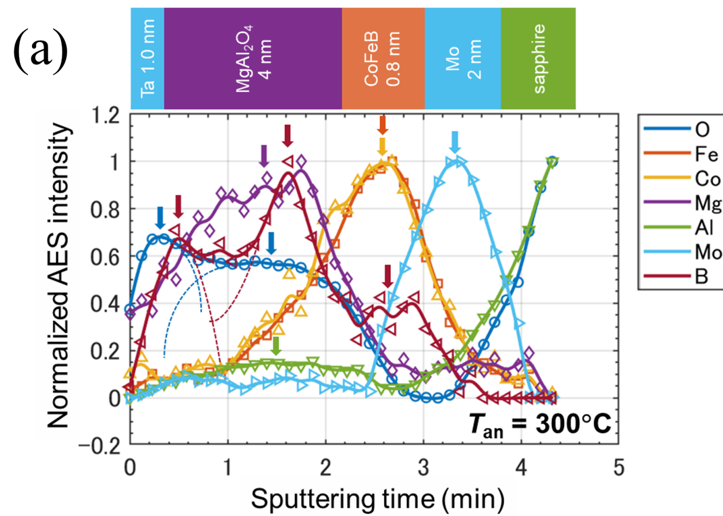

(a) sample A2, Mo (2 nm)/$Co_{19}Fe_{56}B_{25}$ (0.8 nm)/$MgAl_2O_4$($4nm$) /Ta (1 nm), $T_{an} = 300°C$

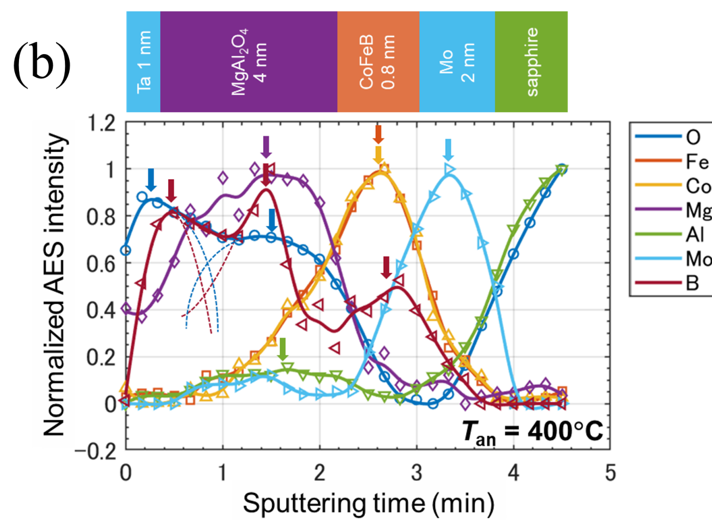

(b) sample B2, Mo (2 nm)/$Co_{19}Fe_{56}B_{25}$ (0.8 nm)/$MgAl_2O_4$(4nm) /Ta (1 nm), $T_{an} = 400°C$

Figure 5.5: Normalized AES intensity depth profile for samples A2 and B2. The arrows sharing same color with the AES intensity signals correspond to the central position of each element.

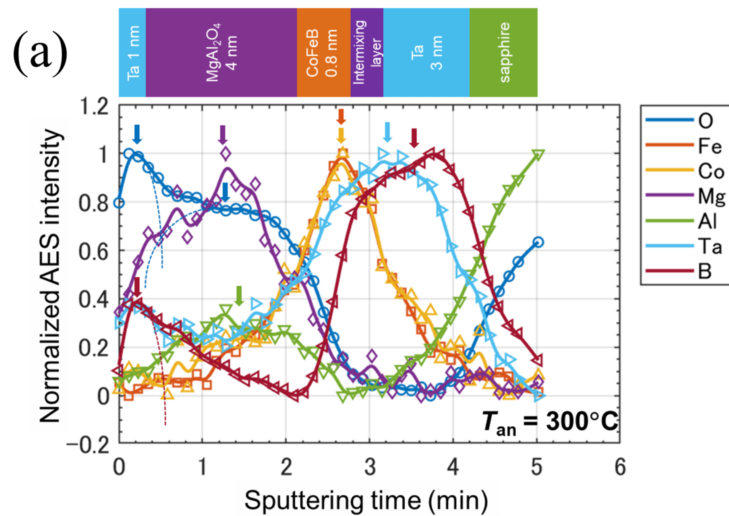

(a) sample C1, Ta (3 nm)/$Co_{19}Fe_{56}B_{25}$ (0.8 nm)/$MgAl_2O_4(4nm)$ /Ta (1 nm), $T_{an} = 300°C$

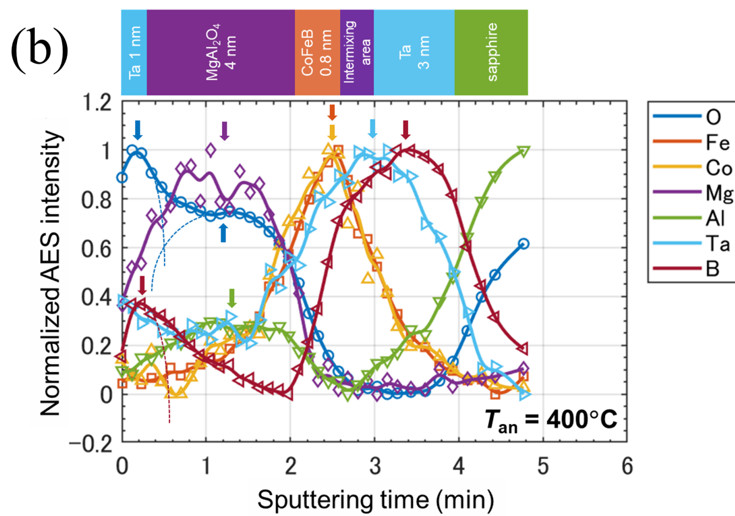

(b) sample C2, Ta (3 nm)/$Co_{19}Fe_{56}B_{25}$ (0.8 nm)/$MgAl_2O_4(4nm)$ /Ta (1 nm), $T_{an} = 400°C$

Figure 5.6: Normalized AES intensity depth profile for samples C1 and C2. The arrows sharing same color with the AES intensity signals correspond to the central position of each element.

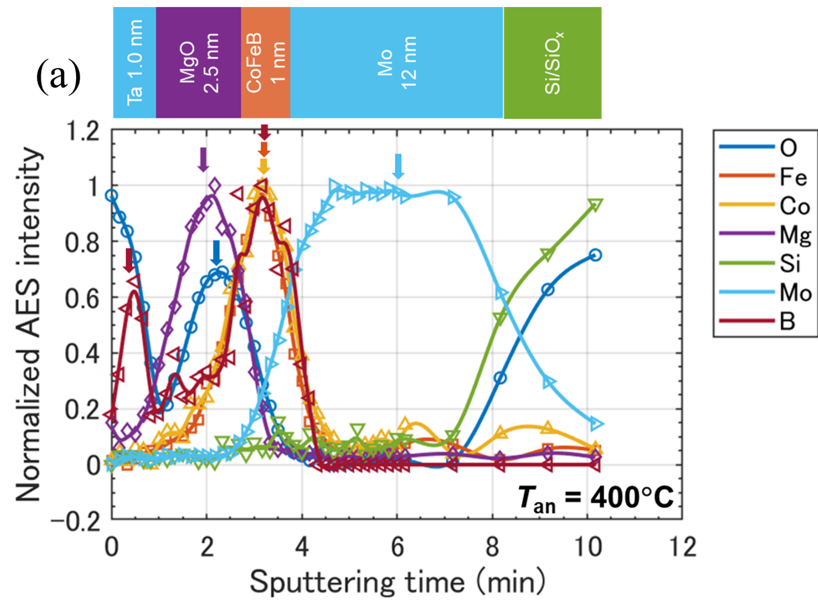

(a) Normalized AES intensity depth profile for a reference sample C3. A large amount of Boron (about 60% of the original Boron) remained in CoFeB.

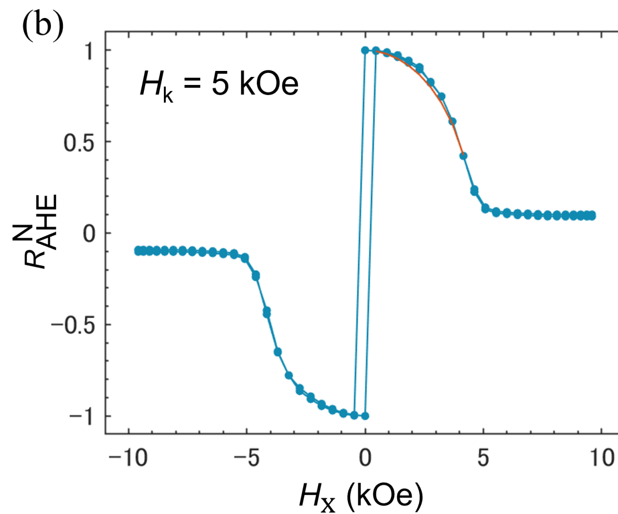

(b) Normalized anomalous Hall resistance of a Hall bar device of sample C3, measured with an in-plane magnetic field. No giant PMA was observed.

Figure 5.7: AES result and normalized anomalous Hall resistance result of sample C3 consisting of Mo (12 nm)/ $Co_{19}Fe_{56}B_{25}$ (1 nm) / MgO (2.5 nm) / Ta (1 nm) deposited on a Si/SiO_2 substrate.

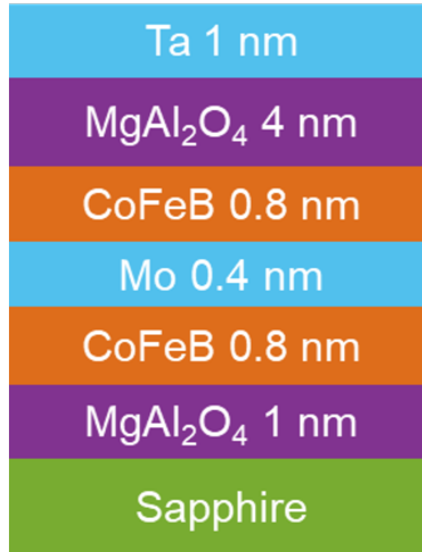

Figure 5.8: Schematic stacking structure of our double CoFeB layers.

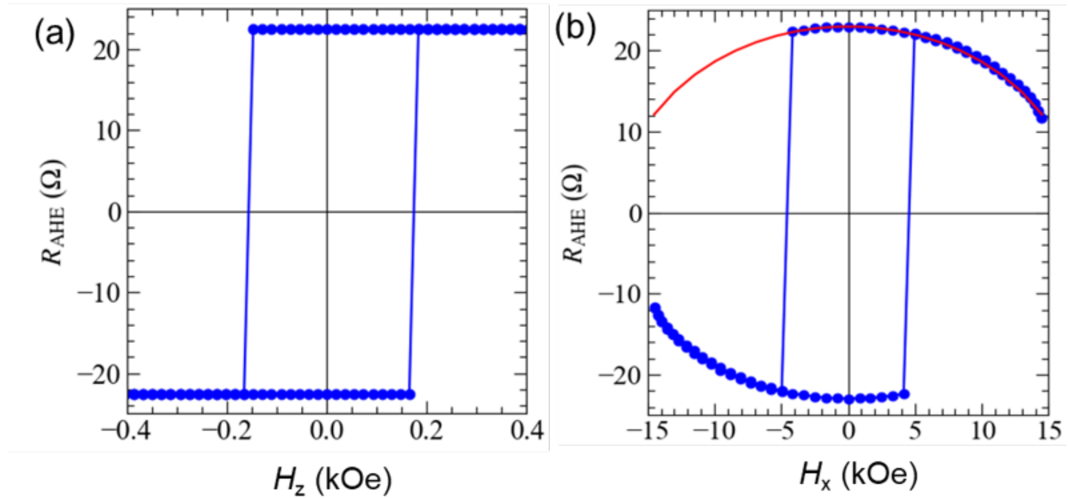

Figure 5.9: (a),(b) Anomalous Hall resistance of a Hall bar of stack with double CoFeB layers, measured with an out-of-plane and in-plane magnetic field, respectively. The red line in (b) is a fitting curve that reveals a giant H_k = 17 kOe in this stack.

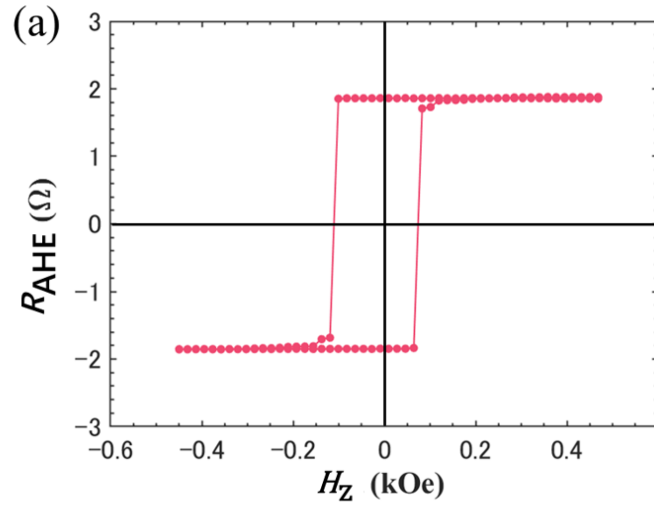

(a) Samples A2 (t_{CoFeB} = 0.8 nm) measured with an out of plane magnetic field H_z.

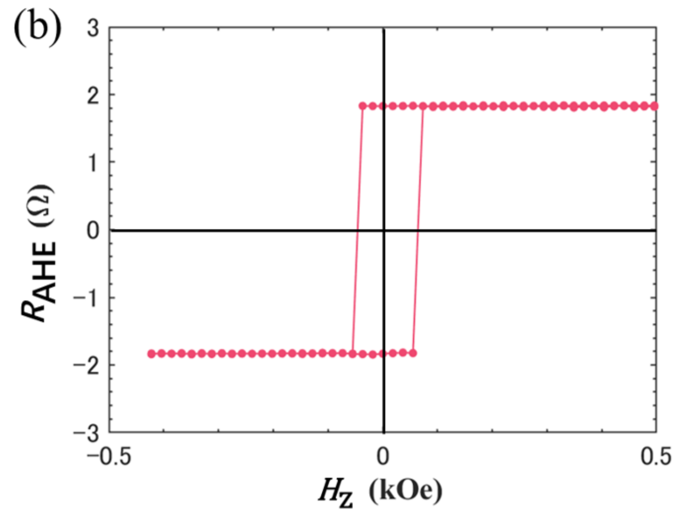

(b) Samples B2 (t_{CoFeB} = 0.8 nm) measured with an out of plane magnetic field H_z.

Figure 5.10: Anomalous Hall resistance R_{AHE} of Mo (2 nm)/$Co_{19}Fe_{56}B_{25}$ (t_{CoFeB} = 0.8 nm)/$MgAl_2O_4$ (4 nm)/Ta (1 nm) multilayers subjected to annealing at 300°C for 30 minutes (sample A2) and those with an additional 400°C annealing for 30 minutes (sample B2).

Chapter 6

Conclusions

In this dissertation, we have demonstrated 2 researches around the prerequisite technology of SOT-MRAM:

1. Integrate high performance BiSb topological insulator and perpendicularly magnetized CoFeB/MgO heterostructure to realize ultralow power SOT-MRAM in the future.

2. Improving PMA of CoFeB after 400°C annealing for further scaling beyond the 16 nm CMOS process.

Basing on the two results from this study, it is possible to realize the thermal-robust SOT-MRAM with low switching current and scalability in the future.

In Chapter 1, we overviewed the evolution of computing technology alongside the advent of memory technologies. We then discussed why STT-MRAM is insufficient to reduce the switching current and switching time. Then, we introduce the potential of SOT-MRAM as the next-generation ultralow power, ultrafast MRAM technology.

In Chapter 2, to comprehensively understand all the physical aspects in a SOT-MRAM cell, we overviewed important magnetic properties with focus on magnetic anisotropies. Then, we introduce the spin Hall effect, topological insulator, and BiSb as a conductive topological insulator with a giant spin Hall angle.

In Chapter 3, we introduced the sputtering technique and the Hall bar patterning process for device fabrication in this dissertation. We also explained

the second harmonic measurement for evaluating the $\theta_{\mathrm{SH}}^{\mathrm{eff}}$. Then we explained the SQUID, XRR and AES measurements that were used to characterize the samples.

In Chapter 4, we studied the PMA and SOT characteristics in $Bi_{0.85}Sb_{0.15}$ (001) (10 nm)/Ru(Ti) (1∼4 nm)/Ta (0.8 nm)/$Co_{20}Fe_{60}B_{20}$ (1 nm)/MgO (2.5 nm)/Ta (1 nm) deposited by magnetron sputtering on c-plane sapphire substrates. We found that the highest $\theta_{\mathrm{SH}}^{\mathrm{eff}}$ is obtained when Ru(Ti) buffer layer thickness is 3 nm. Furthermore, by depositing BiSb with a low power, we achieved $\theta_{\mathrm{SH}}^{\mathrm{eff}} = 6.0 \pm 0.1$, which is higher than that of MBE-grown $(BiSb)_2Te_3$. We then demonstrated the full SOT magnetization switching with a small zero Kelvin threshold switching current density of 1.5×10^6 A $\cdot$ cm^{-2}. Our benchmarking shows that the SOT magnetization power consumption in our stack is 2∼3 orders smaller than that in HMs or other TIs. Our results show that sputtered BiSb has the potential for ultrafast and ultralow power SOT-MRAM.

In Chapter 5, by using B-rich $Co_{19}Fe_{56}B_{25}$ in Mo/CoFeB/$MgAl_2O_4$, we realized giant PMA with H_{k} of 17.5 $\sim$ 19.5 kOe, and K_{eff} of $6.9 \times 10^6 \sim 9.4 \times 10^6$ erg $\cdot$ cm^{-3}. The giant PMA originates from the low demagnetization energy owing to the small M_{s} of B-rich $Co_{19}Fe_{56}B_{25}$ exposed to 300 °C and 400 °C annealing. The MDL in our samples is negligible (< 0.1 nm). AES measurements show that the Mo underlayer effectively blocks Boron diffusion and has clean and sharp interface with CoFeB, while $MgAl_2O_4$ provides a reasonable sink for Boron. The good balance between the Boron-blocking Mo layer and the Boron-sink $MgAl_2O_4$ layer results in about 20% of the origin Boron remaining in CoFeB, leading to a small M_{S} and giant PMA. We also demonstrated double CoFeB layers with giant PMA for use in more advanced CMOS process. Our results provide a recipe for designing MTJ with improved resistance against thermal and external magnetic field disturbance for further device size scaling.

Bibliography

[1] PrecedenceResearch. *Magnetoresistive Random Access Memory (MRAM) Market Surges Amid Rising Demand for High-Speed, Non-Volatile Storage.* Market Analysis, 2025, Retrieved from https://www.precedenceresearch. com/magnetoresistive-random-access-memory-market.

[2] Michael R Williams. The origins, uses, and fate of the edvac. *IEEE Annals of the History of Computing*, 15(1):22–38, 2002.

[3] Neetu Rathi, Anil Kumar, Neeraj Gupta, and Sanjay Kumar Singh. A review of low-power static random access memory (sram) designs. *2023 IEEE Devices for Integrated Circuit (DevIC)*, pages 455–459, 2023.

[4] R Preston. Register files and caches. *Design of High-Performance Microprocessor Circuits*, pages 285–308, 2001.

[5] John Crowe and Barrie Hayes-Gill. *Introduction to digital electronics*. Elsevier, 1998.

[6] Geumjong Bae, D-I Bae, M Kang, SM Hwang, SS Kim, B Seo, TY Kwon, TJ Lee, C Moon, and et al Choi, YM. 3nm gaa technology featuring multi-bridge-channel fet for low power and high performance applications. In *2018 IEEE international electron devices meeting (IEDM)*, pages 28–7. IEEE, 2018.

[7] Seung-Geun Jung, Dongwon Jang, Seong-Ji Min, Euyjin Park, and Hyun-Yong Yu. Performance analysis on complementary fet (cfet) relative to standard cmos with nanosheet fet. *IEEE Journal of the Electron Devices Society*, 10:78–82, 2021.

[8] Kwiwook Kim and Myeong-jae Park. Present and future, challenges of high bandwith memory (hbm). In *2024 IEEE International Memory Workshop (IMW)*, pages 1–4. IEEE, 2024.

[9] Rino Micheloni, Luca Crippa, and Cristian Zambelli. Introduction to 3d nand flash memories. In *Machine Learning and Non-volatile Memories*, pages 87–108. Springer, 2022.

[10] Mark H Kryder, Edward C Gage, Terry W McDaniel, William A Challener, Robert E Rottmayer, Ganping Ju, Yiao-Tee Hsia, and M Fatih Erden. Heat assisted magnetic recording. *Proceedings of the IEEE*, 96(11):1810–1835, 2008.

[11] R Wood. Shingled magnetic recording and two-dimensional magnetic recording acknowledgements. *IEEE Magnetics Society Santa Clara Valley*, pages 1–59, 2010.

[12] Michael Salo, Terry Olson, Richard Galbraith, Richard Brockie, Byron Lengsfield, Hiroyuki Katada, and Yasutaka Nishida. The structure of shingled magnetic recording tracks. *IEEE transactions on magnetics*, 50(3):18–23, 2014.

[13] Roger Wood, Rick Galbraith, and Jonathan Coker. 2-d magnetic recording: Progress and evolution. *IEEE Transactions on Magnetics*, 51(4):1–7, 2015.

[14] Harekrishna Kumar and VK Tomar. A review on performance evaluation of different low power sram cells in nano-scale era. *Wireless Personal Communications*, 117(3):1959–1984, 2021.

[15] Kyoung-Su Park, Young-Pil Park, and No-Cheol Park. Prospect of recording technologies for higher storage performance. *IEEE Transactions on magnetics*, 47(3):539–545, 2011.

[16] Evgeny Y Tsymbal and David G Pettifor. Perspectives of giant magnetoresistance. In *Solid state physics*, volume 56, pages 113–237. Elsevier, 2001.

[17] Shinji Yuasa. *Magnetic Properties of Materials for MRAM*, chapter 2, pages 29–54. Wiley Online Library, 2017.

[18] Michel Julliere. Tunneling between ferromagnetic films. *Physics letters A*, 54(3):225–226, 1975.

[19] Xiaobing Feng, O Bengone, M Alouani, I Rungger, and S Sanvito. Interface and transport properties of fe/v/mgo/fe and fe/v/fe/mgo/fe magnetic tunneling junctions. *Physical Review B—Condensed Matter and Materials Physics*, 79(21):214432, 2009.

[20] Atsufumi Hirohata, Keisuke Yamada, Yoshinobu Nakatani, Ioan-Lucian Prejbeanu, Bernard Diény, Philipp Pirro, and Burkard Hillebrands. Review on spintronics: Principles and device applications. *Journal of Magnetism and Magnetic Materials*, 509:166711, 2020.

[21] Stuart SP Parkin, Christian Kaiser, Alex Panchula, Philip M Rice, Brian Hughes, Mahesh Samant, and See-Hun Yang. Giant tunnelling magnetoresistance at room temperature with mgo (100) tunnel barriers. *Nature materials*, 3(12):862–867, 2004.

[22] WH Butler, X-G Zhang, TC Schulthess, and JM MacLaren. Spin-dependent tunneling conductance of fe— mgo— fe sandwiches. *Physical Review B*, 63(5):054416, 2001.

[23] Shinji Yuasa, Taro Nagahama, Akio Fukushima, Yoshishige Suzuki, and Koji Ando. Giant room-temperature magnetoresistance in single-crystal fe/mgo/fe magnetic tunnel junctions. *Nature materials*, 3(12):868–871, 2004.

[24] Thomas Scheike, Zhenchao Wen, Hiroaki Sukegawa, and Seiji Mitani. 631% room temperature tunnel magnetoresistance with large oscillation effect in cofe/mgo/cofe (001) junctions. *Applied Physics Letters*, 122(11), 2023.

[25] Luc Berger. Emission of spin waves by a magnetic multilayer traversed by a current. *Physical Review B*, 54(13):9353, 1996.

[26] John C Slonczewski. Current-driven excitation of magnetic multilayers. *Journal of Magnetism and Magnetic Materials*, 159(1-2):L1–L7, 1996.

[27] Sébastien Bandiera, Ricardo C Sousa, Y Dahmane, Clarisse Ducruet, C Portemont, Vincent Baltz, Stéphane Auffret, Ion Lucian Prejbeanu, and Bernard Dieny. Comparison of synthetic antiferromagnets and hard ferromagnets as reference layer in magnetic tunnel junctions with perpendicular magnetic anisotropy. *IEEE Magnetics Letters*, 1:3000204–3000204, 2010.

[28] Masanori Hosomi, H Yamagishi, T Yamamoto, Kazuhiro Bessho, Yutaka Higo, Kazutaka Yamane, H Yamada, M Shoji, Hiroaki Hachino, and et al Fukumoto, C. A novel nonvolatile memory with spin torque transfer magnetization switching: Spin-ram. In *IEEE InternationalElectron Devices Meeting, 2005. IEDM Technical Digest.*, pages 459–462. IEEE, 2005.

[29] S Aggarwal, H Almasi, M DeHerrera, B Hughes, S Ikegawa, J Janesky, HK Lee, H Lu, FB Mancoff, K Nagel, et al. Demonstration of a reliable 1 gb standalone spin-transfer torque mram for industrial applications. In *2019 IEEE International Electron Devices Meeting (IEDM)*, pages 2–1. IEEE, 2019.

[30] Sumio Ikegawa, Frederick B Mancoff, Jason Janesky, and Sanjeev Aggarwal. Magnetoresistive random access memory: Present and future. *IEEE Transactions on Electron Devices*, 67(4):1407–1419, 2020.

[31] VB Naik, K Lee, K Yamane, R Chao, J Kwon, N Thiyagarajah, NL Chung, SH Jang, B Behin-Aein, JH Lim, et al. Manufacturable 22nm fd-soi embedded mram technology for industrial-grade mcu and iot applications. In *2019 IEEE International Electron Devices Meeting (IEDM)*, pages 2–3. IEEE, 2019.

[32] Sumio Ikegawa, Frederick B Mancoff, and Sanjeev Aggarwal. Commercialization of mram–historical and future perspective. In *2021 IEEE International Interconnect Technology Conference (IITC)*, pages 1–3. IEEE, 2021.

[33] WS Zhao, Yue Zhang, Thibaut Devolder, Jacques-Olivier Klein, Dafine Ravelosona, Claude Chappert, and Pascale Mazoyer. Failure and reliability analysis of stt-mram. *Microelectronics Reliability*, 52(9-10):1848–1852, 2012.

[34] Yu-Der Chih, Chung-Cheng Chou, Yi-Chun Shih, Chia-Fu Lee, Win-San Khwa, Chun-Yu Wu, Kuei-Hung Shen, Wen-Ting Chu, Meng-Fan Chang, Harry Chuang, et al. Design challenges and solutions of emerging nonvolatile memory for embedded applications. In *2021 IEEE International Electron Devices Meeting (IEDM)*, pages 2–4. IEEE, 2021.

[35] Helia Naeimi, Charles Augustine, Arijit Raychowdhury, James Tschanz, et al. Sttram scaling and retention failure. *intel technology journal*, 17(1), 2013.

[36] Rajendra Bishnoi, Mojtaba Ebrahimi, Fabian Oboril, and Mehdi B Tahoori. Asynchronous asymmetrical write termination (aawt) for a low power stt-mram. In *2014 Design, Automation & Test in Europe Conference & Exhibition (DATE)*, pages 1–6. IEEE, 2014.

[37] Dongsoo Lee, Sumeet Kumar Gupta, and Kaushik Roy. High-performance low-energy stt mram based on balanced write scheme. In *Proceedings of the 2012 ACM/IEEE international symposium on Low power electronics and design*, pages 9–14, 2012.

[38] Fabian Oboril, Rajendra Bishnoi, Mojtaba Ebrahimi, and Mehdi B Tahoori. Evaluation of hybrid memory technologies using sot-mram for on-chip cache hierarchy. *IEEE Transactions on Computer-Aided Design of Integrated Circuits and Systems*, 34(3):367–380, 2015.

[39] K Jabeur, LD Buda-Prejbeanu, G Prenat, and G Di Pendina. Study of two writing schemes for a magnetic tunnel junction based on spin orbit torque. In *Proceedings of World Academy of Science, Engineering and Technology*, number 80, page 517. World Academy of Science, Engineering and Technology (WASET), 2013.

[40] Murat Cubukcu, Olivier Boulle, Marc Drouard, Kevin Garello, Can Onur Avci, Ioan Mihai Miron, Juergen Langer, Berthold Ocker, Pietro

Gambardella, and Gilles Gaudin. Spin-orbit torque magnetization switching of a three-terminal perpendicular magnetic tunnel junction. *Applied Physics Letters*, 104(4), 2014.

[41] Arno van den Brink, Stefan Cosemans, Sven Cornelissen, Mauricio Manfrini, Adrien Vaysset, Wim Van Roy, Tai Min, HJM Swagten, and Bert Koopmans. Spin-hall-assisted magnetic random access memory. *Applied Physics Letters*, 104(1), 2014.

[42] Nguyen Huynh Duy Khang, Yugo Ueda, and Pham Nam Hai. A conductive topological insulator with large spin hall effect for ultralow power spin–orbit torque switching. *Nature materials*, 17(9):808–813, 2018.

[43] Mahendra Dc, Roberto Grassi, Jun-Yang Chen, Mahdi Jamali, Danielle Reifsnyder Hickey, Delin Zhang, Zhengyang Zhao, Hongshi Li, P Quarterman, Yang Lv, et al. Room-temperature high spin–orbit torque due to quantum confinement in sputtered bi x se (1–x) films. *Nature materials*, 17(9):800–807, 2018.

[44] Tuo Fan, Nguyen Huynh Duy Khang, Takanori Shirokura, Ho Hoang Huy, and Pham Nam Hai. Low power spin–orbit torque switching in sputtered bisb topological insulator/perpendicularly magnetized copt/mgo multilayers on oxidized si substrate. *Applied Physics Letters*, 119(8), 2021.

[45] Takanori Shirokura and Pham Nam Hai. Giant spin hall effect in half-heusler alloy topological semimetal yptbi grown at low temperature. *AIP Advances*, 12(12), 2022.

[46] VD Nguyen, S Rao, K Wostyn, and S Couet. Recent progress in spin-orbit torque magnetic random-access memory. *npj Spintronics*, 2(1):48, 2024.

[47] S Ikeda, K Miura, H Yamamoto, K Mizunuma, HD Gan, M Endo, Sl Kanai, J Hayakawa, F Matsukura, and H Ohno. A perpendicular-anisotropy cofeb–mgo magnetic tunnel junction. *Nature materials*, 9(9):721–724, 2010.

[48] Ho Hoang Huy, Zhang Ruixian, Takanori Shirokura, Shigeki Takahashi, Yoshiyuki Hirayama, and Pham Nam Hai. Integration of bisb topological insulator and cofeb/mgo with perpendicular magnetic anisotropy using an oxide interfacial layer for ultralow power sot-mram cache memory. *IEEE Transactions on Magnetics*, 59(11):1–5, 2023.

[49] Ho Hoang Huy, Julian Sasaki, Nguyen Huynh Duy Khang, Shota Namba, Pham Nam Hai, Quang Le, Brian York, Cherngye Hwang, Xiaoyong Liu, and et al Gribelyuk, Michael. Large inverse spin hall effect in bisb topological insulator for 4 tb/in2 magnetic recording technology. *Applied Physics Letters*, 122(5), 2023.

[50] Hao Wu, Peng Zhang, Peng Deng, Qianqian Lan, Quanjun Pan, Seyed Armin Razavi, Xiaoyu Che, Li Huang, Bingqian Dai, and et al Wong, Kin. Room-temperature spin-orbit torque from topological surface states. *Physical review letters*, 123(20):207205, 2019.

[51] Wei-Gang Wang, Stephen Hageman, Mingen Li, Sunxiang Huang, Xiaoming Kou, Xin Fan, John Q Xiao, and CL Chien. Rapid thermal annealing study of magnetoresistance and perpendicular anisotropy in magnetic tunnel junctions based on mgo and cofeb. *Applied Physics Letters*, 99(10), 2011.

[52] H Meng, R Sbiaa, CC Wang, SYH Lua, and MAK Akhtar. Annealing temperature window for tunneling magnetoresistance and spin torque switching in cofeb/mgo/cofeb perpendicular magnetic tunnel junctions. *Journal of Applied Physics*, 110(10), 2011.

[53] HD Gan, H Sato, M Yamanouchi, S Ikeda, K Miura, R Koizumi, F Matsukura, and H Ohno. Origin of the collapse of tunnel magnetoresistance at high annealing temperature in cofeb/mgo perpendicular magnetic tunnel junctions. *Applied Physics Letters*, 99(25), 2011.

[54] Naruto Miyakawa, DC Worledge, and Koji Kita. Impact of ta diffusion on the perpendicular magnetic anisotropy of ta/cofeb/mgo. *IEEE Magnetics Letters*, 4:1000104–1000104, 2013.

[55] Jyotirmoy Chatterjee, Taiebeh Tahmasebi, Johan Swerts, Gouri Sankar Kar, and Jo De Boeck. Impact of seed layer on post-annealing behavior of transport and magnetic properties of co/pt multilayer-based bottom-pinned perpendicular magnetic tunnel junctions. *Applied Physics Express*, 8(6):063002, 2015.

[56] T Liu, Y Zhang, JW Cai, and HY Pan. Thermally robust mo/cofeb/mgo trilayers with strong perpendicular magnetic anisotropy. *Scientific reports*, 4(1):5895, 2014.

[57] T Liu, JW Cai, and Li Sun. Large enhanced perpendicular magnetic anisotropy in cofeb/mgo system with the typical ta buffer replaced by an hf layer. *Aip Advances*, 2(3), 2012.

[58] Zeyi Zhu, Bin Kang, Yafan Wan, Hehai Long, Xue Wang, Zhihao Liu, Xiaomeng Wang, Li Ma, and Fu Zheng. Modulation of perpendicular magnetic anisotropy in mgo/cofeb/hf structures via a mo insertion layer. *Journal of Alloys and Compounds*, page 182626, 2025.

[59] Nobuo Tanaka. Introduction to magnetic random-access memory. *MRS BULLETIN*, 43, 2018.

[60] D-X Chen, James A Brug, and Ronald B Goldfarb. Demagnetizing factors for cylinders. *IEEE Transactions on magnetics*, 27(4):3601–3619, 2002.

[61] N Perrissin, G Gregoire, S Lequeux, L Tillie, N Strelkov, S Auffret, LD Buda-Prejbeanu, RC Sousa, Laurent Vila, and et al Dieny, B. Perpendicular shape anisotropy spin transfer torque magnetic random-access memory: Towards sub-10 nm devices. *Journal of Physics D: Applied Physics*, 52(23):234001, 2019.

[62] Chun Feng, Qian Zhan, Baohe Li, Jiao Teng, Minghua Li, Yong Jiang, and Guanghua Yu. Magnetic properties and microstructure of fept/au multilayers with high perpendicular magnetocrystalline anisotropy. *Applied Physics Letters*, 93(15), 2008.

[63] B Dieny and M Chshiev. Perpendicular magnetic anisotropy at transition metal/oxide interfaces and applications. *Reviews of Modern Physics*, 89(2):025008, 2017.

[64] DC Worledge, G Hu, David W Abraham, Jonathan Z Sun, PL Trouilloud, J Nowak, S Brown, MC Gaidis, Eugene J O'Sullivan, and RP Robertazzi. Spin torque switching of perpendicular ta/cofeb/mgo based magnetic tunnel junctions. *Applied physics letters*, 98(2), 2011.

[65] Aurelien Manchon and Shufeng Zhang. Theory of nonequilibrium intrinsic spin torque in a single nanomagnet. *Physical Review B—Condensed Matter and Materials Physics*, 78(21):212405, 2008.

[66] Bernard Rodmacq, Aurélien Manchon, Clarisse Ducruet, Stéphane Auffret, and Bernard Dieny. Influence of thermal annealing on the perpendicular magnetic anisotropy of pt/co/alox trilayers. *Physical Review B—Condensed Matter and Materials Physics*, 79(2):024423, 2009.

[67] JB Yang, YB Yang, XG Chen, XB Ma, JZ Han, YC Yang, S Guo, AR Yan, QZ Huang, MM Wu, et al. Anisotropic nanocrystalline mnbi with high coercivity at high temperature. *Applied Physics Letters*, 99(8), 2011.

[68] SSP Parkin, N More, and KP Roche. Oscillations in exchange coupling and magnetoresistance in metallic superlattice structures: Co/ru, co/cr, and fe/cr. *Physical review letters*, 64(19):2304, 1990.

[69] Robin FC Farrow, Bernard Dieny, Markus Donath, Albert Fert, and BD Hermsmeier. *Magnetism and Structure in systems of Reduced Dimension*, volume 309. Springer Science & Business Media, 2013.

[70] eg P Bruno and Ch Chappert. Oscillatory coupling between ferromagnetic layers separated by a nonmagnetic metal spacer. *Physical review letters*, 67(12):1602, 1991.

[71] Jinwu Wei, Xiao Wang, Baoshan Cui, Chenyang Guo, Hongjun Xu, Yao Guang, Yuqiang Wang, Xuming Luo, Caihua Wan, and et al Feng, Jiafeng. Field-free spin–orbit torque switching in perpendicularly

magnetized synthetic antiferromagnets. *Advanced Functional Materials*, 32(10):2109455, 2022.

[72] P Bruno. Oscillations of interlayer exchange coupling vs. ferromagnetic-layers thickness. *Europhysics Letters*, 23(8):615, 1993.

[73] David N Lambeth, DE Laughlin, S Charap, L-L Lee, P Harllee, and L Tang. Present status and future magnetic data storage. In *Magnetic Hysteresis in Novel Magnetic Materials*, pages 767–780. Springer, 1997.

[74] SN Piramanayagam. Perpendicular recording media for hard disk drives. *Journal of applied physics*, 102(1), 2007.

[75] Shuichi Murakami, Naoto Nagaosa, and Shou-Cheng Zhang. Dissipationless quantum spin current at room temperature. *Science*, 301(5638):1348–1351, 2003.

[76] Jairo Sinova, Dimitrie Culcer, Qian Niu, NA Sinitsyn, T Jungwirth, and Allan H MacDonald. Universal intrinsic spin hall effect. *Physical review letters*, 92(12):126603, 2004.

[77] Sergio O Valenzuela and M Tinkham. Direct electronic measurement of the spin hall effect. *Nature*, 442(7099):176–179, 2006.

[78] Yasuhiro Fukuma, Le Wang, Hiroshi Idzuchi, Saburo Takahashi, Sadamichi Maekawa, and YoshiChika Otani. Giant enhancement of spin accumulation and long-distance spin precession in metallic lateral spin valves. *Nature materials*, 10(7):527–531, 2011.

[79] Tao Yang, Takashi Kimura, and Yoshichika Otani. Giant spin-accumulation signal and pure spin-current-induced reversible magnetization switching. *Nature Physics*, 4(11):851–854, 2008.

[80] Saburo Takahashi and Sadamichi Maekawa. Spin current, spin accumulation and spin hall effect. *Science and Technology of Advanced Materials*, 9(1):014105, 2008.

[81] M Tran, H Jaffrès, C Deranlot, J-M George, A Fert, A Miard, and A Lemaître. Enhancement of the spin accumulation at the interface

between a spin-polarized tunnel junction and a semiconductor. *Physical review letters*, 102(3):036601, 2009.

[82] Spin currents in metallic nanostructures.

[83] Di Xiao, Ming-Che Chang, and Qian Niu. Berry phase effects on electronic properties. *Reviews of modern physics*, 82(3):1959–2007, 2010.

[84] Luis Brey and HA Fertig. Electronic states of graphene nanoribbons studied with the dirac equation. *Physical Review B—Condensed Matter and Materials Physics*, 73(23):235411, 2006.

[85] Aaron Bostwick, Taisuke Ohta, Thomas Seyller, Karsten Horn, and Eli Rotenberg. Quasiparticle dynamics in graphene. *Nature physics*, 3(1):36–40, 2007.

[86] JR Williams, AJ Bestwick, P Gallagher, Seung Sae Hong, Y Cui, Andrew S Bleich, JG Analytis, IR Fisher, and D Goldhaber-Gordon. Unconventional josephson effect in hybrid superconductor-topological insulator devices. *Physical review letters*, 109(5):056803, 2012.

[87] David J Thouless, Mahito Kohmoto, M Peter Nightingale, and Marcel den Nijs. Quantized hall conductance in a two-dimensional periodic potential. *Physical review letters*, 49(6):405, 1982.

[88] K v Klitzing, Gerhard Dorda, and Michael Pepper. New method for high-accuracy determination of the fine-structure constant based on quantized hall resistance. *Physical review letters*, 45(6):494, 1980.

[89] Charles L Kane and Eugene J Mele. Quantum spin hall effect in graphene. *Physical review letters*, 95(22):226801, 2005.

[90] B Andrei Bernevig, Taylor L Hughes, and Shou-Cheng Zhang. Quantum spin hall effect and topological phase transition in hgte quantum wells. *science*, 314(5806):1757–1761, 2006.

[91] Markus Konig, Steffen Wiedmann, Christoph Brune, Andreas Roth, Hartmut Buhmann, Laurens W Molenkamp, Xiao-Liang Qi, and Shou-Cheng Zhang. Quantum spin hall insulator state in hgte quantum wells. *Science*, 318(5851):766–770, 2007.

[92] D. Hsieh, Y. Xia, L. Wray, D. Qian, A. Pal, J. H. Dil, J. Osterwalder, F. Meier, G. Bihlmayer, C. L. Kane, Y. S. Hor, R. J. Cava, and M. Z. Hasan. Observation of unconventional quantum spin textures in topological insulators. *Science*, 323(5916):919–922, 2009.

[93] Yoichi Ando. Topological insulator materials. *Journal of the Physical Society of Japan*, 82(10):102001, 2013.

[94] T Hirahara, Y Sakamoto, Y Saisyu, H Miyazaki, S Kimura, T Okuda, I Matsuda, S Murakami, and S Hasegawa. Topological metal at the surface of an ultrathin bi 1- x sb x alloy film. *Physical Review B—Condensed Matter and Materials Physics*, 81(16):165422, 2010.

[95] Haijun Zhang, Chao-Xing Liu, Xiao-Liang Qi, Xi Dai, Zhong Fang, and Shou-Cheng Zhang. Topological insulators in bi2se3, bi2te3 and sb2te3 with a single dirac cone on the surface. *Nature physics*, 5(6):438–442, 2009.

[96] Qiming Shao, Peng Li, Luqiao Liu, Hyunsoo Yang, Shunsuke Fukami, Armin Razavi, Hao Wu, Kang Wang, Frank Freimuth, Yuriy Mokrousov, Mark D. Stiles, Satoru Emori, Axel Hoffmann, Johan Åkerman, Kaushik Roy, Jian-Ping Wang, See-Hun Yang, Kevin Garello, and Wei Zhang. Roadmap of spin–orbit torques. *IEEE Transactions on Magnetics*, 57(7):1–39, 2021.

[97] B Lenoir, M Cassart, J-P Michenaud, H Scherrer, and S Scherrer. Transport properties of bi-rich bi-sb alloys. *Journal of Physics and Chemistry of Solids*, 57(1):89–99, 1996.

[98] Yugo Ueda, Nguyen Huynh Duy Khang, Kenichiro Yao, and Pham Nam Hai. Epitaxial growth and characterization of bi1-xsbx spin hall thin films on gaas(111)a substrates. *Applied Physics Letters*, 110(6):062401, 02 2017.

[99] Jeffrey CY Teo, Liang Fu, and CL Kane. Surface states and topological invariants in three-dimensional topological insulators: Application to bi 1- x sb x. *Physical Review B—Condensed Matter and Materials Physics*, 78(4):045426, 2008.

[100] H. Kitagawa, H. Noguchi, M. Itoh, and Y. Noda. Thermoelectric properties of semiconducting bi-rich bi-sb alloys. In *Proceedings ICT'03. 22nd International Conference on Thermoelectrics (IEEE Cat. No.03TH8726)*, pages 290–293, 2003.

[101] Xie-Gang Zhu, Malthe Stensgaard, Lucas Barreto, Wendell Simoes e Silva, Søren Ulstrup, Matteo Michiardi, Marco Bianchi, Maciej Dendzik, and Philip Hofmann. Three dirac points on the (110) surface of the topological insulator bi1-xsbx. *New Journal of Physics*, 15(10):103011, oct 2013.

[102] Donald M Mattox. *Handbook of physical vapor deposition (PVD) processing*. William Andrew, 2010.

[103] Philippe Mangin and et al. *SUPERCONDUCTING QUANTUM INTERFERENCE DEVICE*.

[104] Heinz Kiessig. Untersuchungen zur totalreflexion von röntgenstrahlen. *Annalen der Physik*, 402(6):715–768, 1931.

[105] A Ulyanenkov, K Omote, and J Harada. The genetic algorithm: refinement of x-ray reflectivity data from multilayers and thin films. *Physica B: Condensed Matter*, 283(1-3):237–241, 2000.

[106] Alvin Warren Czanderna. *Methods of surface analysis*, volume 1. Elsevier, 2012.

[107] Kevin Garello, Can Onur Avci, Ioan Mihai Miron, Manuel Baumgartner, Abhijit Ghosh, Stéphane Auffret, Olivier Boulle, Gilles Gaudin, and Pietro Gambardella. Ultrafast magnetization switching by spin-orbit torques. *Applied Physics Letters*, 105(21), 2014.

[108] C Zhang, S Fukami, H Sato, F Matsukura, and H Ohno. Spin-orbit torque induced magnetization switching in nano-scale ta/cofeb/mgo. *Applied Physics Letters*, 107(1), 2015.

[109] Eva Grimaldi, Viola Krizakova, Giacomo Sala, Farrukh Yasin, Sébastien Couet, Gouri Sankar Kar, Kevin Garello, and Pietro Gambardella.

Single-shot dynamics of spin–orbit torque and spin transfer torque switching in three-terminal magnetic tunnel junctions. *Nature nanotechnology*, 15(2):111–117, 2020.

[110] Masanori Natsui, Akira Tamakoshi, Hiroaki Honjo, Toshinari Watanabe, Takashi Nasuno, Chaoliang Zhang, Takaho Tanigawa, Hirofumi Inoue, Masaaki Niwa, and et al Yoshiduka, Toru. Dual-port sot-mram achieving 90-mhz read and 60-mhz write operations under field-assistance-free condition. *IEEE Journal of Solid-State Circuits*, 56(4):1116–1128, 2020.

[111] Kevin Garello, F. Yasin, H. Hody, S. Couet, L. Souriau, S. H Sharifi, J. Swerts, R. Carpenter, S. Rao, W. Kim, J. Wu, K. K V Sethu, M. Pak, N. Jossart, D. Crotti, A. Furnemont, and G. S Kar. Manufacturable 300mm platform solution for Field-Free Switching SOT-MRAM. In *2019 Symposium on VLSI Circuits*, pages T194–T195, Kyoto, France, June 2019. IEEE.

[112] Luqiao Liu, Chi-Feng Pai, Y Li, HW Tseng, DC Ralph, and RA Buhrman. Spin-torque switching with the giant spin hall effect of tantalum. *Science*, 336(6081):555–558, 2012.

[113] Chi-Feng Pai, Luqiao Liu, Y Li, HW Tseng, DC Ralph, and RA Buhrman. Spin transfer torque devices utilizing the giant spin hall effect of tungsten. *Applied Physics Letters*, 101(12), 2012.

[114] L. Thomas. Basic Principles and Challenges of STT-MRAM for Embedded Memory Applications. In *33rd International Conference on Massive Storage Systems and Technology*, Santa Clara, CA, United States, May 2017.

[115] Alex R Mellnik, JS Lee, Anthony Richardella, Jennifer L Grab, Peter J Mintun, Mark H Fischer, Abolhassan Vaezi, Aurelien Manchon, E-A Kim, and et al Samarth, Nitin. Spin-transfer torque generated by a topological insulator. *Nature*, 511(7510):449–451, 2014.

[116] Yi Wang, Dapeng Zhu, Yang Wu, Yumeng Yang, Jiawei Yu, Rajagopalan Ramaswamy, Rahul Mishra, Shuyuan Shi, Mehrdad Elyasi, and et al

Teo, Kie-Leong. Room temperature magnetization switching in topological insulator-ferromagnet heterostructures by spin-orbit torques. *Nature communications*, 8(1):1364, 2017.

[117] T Fan, NHD Khang, S Nakano, and PN Hai. Ultrahigh efficient spin orbit torque magnetization switching in fully sputtered topological insulator and ferromagnet multilayers. sci. rep. 12 (1), 2998, 2022.

[118] Julian Sasaki, Shota Namba, Shigeki Takahashi, Yoshiyuki Hirayama, and Pham Nam Hai. Highly efficient spin current source using bisb topological insulator/nio bilayers. *Japanese Journal of Applied Physics*, 62(SC):SC1005, 2022.

[119] Tuo Fan, Mustafa Tobah, Takanori Shirokura, Nguyen Huynh Duy Khang, and Pham Nam Hai. Crystal growth and characterization of topological insulator bisb thin films by sputtering deposition on sapphire substrates. *Japanese Journal of Applied Physics*, 59(6):063001, 2020.

[120] J Sasaki, HH Huy, NHD Khang, PN Hai, Q Le, B York, X Liu, S Le, C Hwang, and et al Ho, M. Improvement of the effective spin hall angle by inserting an interfacial layer in sputtered bisb topological insulator (bottom)/ferromagnet with in-plane magnetization. *IEEE Transactions on Magnetics*, 58(4):1–4, 2021.

[121] Hao Wu, Aitian Chen, Peng Zhang, Haoran He, John Nance, Chenyang Guo, Julian Sasaki, Takanori Shirokura, Pham Nam Hai, and et al Fang, Bin. Magnetic memory driven by topological insulators. *Nature communications*, 12(1):6251, 2021.

[122] Masamitsu Hayashi, Junyeon Kim, Michihiko Yamanouchi, and Hideo Ohno. Quantitative characterization of the spin-orbit torque using harmonic hall voltage measurements. *Physical Review B*, 89(14):144425, 2014.

[123] Satoshi Yakata, Yasuo Ando, Terunobu Miyazaki, and Shigemi Mizukami. Temperature dependences of spin-diffusion lengths of cu and ru layers. *Japanese journal of applied physics*, 45(5R):3892, 2006.

[124] RH Koch, JA Katine, and JZ Sun. Time-resolved reversal of spin-transfer switching in a nanomagnet. *Physical review letters*, 92(8):088302, 2004.

[125] H Sato, M Yamanouchi, K Miura, S Ikeda, HD Gan, K Mizunuma, R Koizumi, F Matsukura, and H Ohno. Junction size effect on switching current and thermal stability in cofeb/mgo perpendicular magnetic tunnel junctions. *Applied Physics Letters*, 99(4), 2011.

[126] H Sato, M Yamanouchi, K Miura, Shoji Ikeda, R Koizumi, F Matsukura, and H Ohno. Cofeb thickness dependence of thermal stability factor in cofeb/mgo perpendicular magnetic tunnel junctions. *IEEE Magnetics Letters*, 3:3000204–3000204, 2012.

[127] H Sato, M Yamanouchi, S Ikeda, S Fukami, F Matsukura, and H Ohno. Mgo/cofeb/ta/cofeb/mgo recording structure with low intrinsic critical current and high thermal stability. *Journal of the Magnetics Society of Japan*, 38(2-2):56–60, 2014.

[128] Soonha Cho, Seung-heon Chris Baek, Kyeong-Dong Lee, Younghun Jo, and Byong-Guk Park. Large spin hall magnetoresistance and its correlation to the spin-orbit torque in w/cofeb/mgo structures. *Scientific reports*, 5(1):14668, 2015.

[129] G Mihajlović, O Mosendz, L Wan, N Smith, Y Choi, Y Wang, and JA Katine. Pt thickness dependence of spin hall effect switching of in-plane magnetized cofeb free layers studied by differential planar hall effect. *Applied Physics Letters*, 109(19), 2016.

[130] Xie-Gang Zhu, Malthe Stensgaard, Lucas Barreto, Wendell Simoes e Silva, Søren Ulstrup, Matteo Michiardi, Marco Bianchi, Maciej Dendzik, and Philip Hofmann. Three dirac points on the (110) surface of the topological insulator bi1- xsbx. *New Journal of Physics*, 15(10):103011, 2013.

[131] York B.R., Le Q., Liu X., Okamura S., Hwang C., and et al. High Thermal Reliability and High Spin Hall Angle Observed in SOT-Reader Thin Films Using BiSbX Topological Insulators. In *The 34th Magnetic Recording Conference*, MN, United States, August 2023.

[132] N Nakajima, T Koide, T Shidara, H Miyauchi, H Fukutani, A Fujimori, K Iio, T Katayama, M Nỳvlt, and Y Suzuki. Perpendicular magnetic anisotropy caused by interfacial hybridization via enhanced orbital moment in co/pt multilayers: Magnetic circular x-ray dichroism study. *Physical Review Letters*, 81(23):5229, 1998.

[133] Y Fan, HB Zhao, G Lüpke, AT Hanbicki, CH Li, and BT Jonker. Anisotropic exchange coupling and stress-induced uniaxial magnetic anisotropy in fe/gaas (001). *Physical Review B—Condensed Matter and Materials Physics*, 85(16):165311, 2012.

[134] David D Djayaprawira, Koji Tsunekawa, Motonobu Nagai, Hiroki Maehara, Shinji Yamagata, Naoki Watanabe, Shinji Yuasa, Yoshishige Suzuki, and Koji Ando. 230% room-temperature magnetoresistance in cofeb/ mgo/ cofeb magnetic tunnel junctions. *Applied physics letters*, 86(9), 2005.

[135] Shinji Yuasa, Yoshishige Suzuki, Toshikazu Katayama, and Koji Ando. Characterization of growth and crystallization processes in cofeb/ mgo/ cofeb magnetic tunnel junction structure by reflective high-energy electron diffraction. *Applied Physics Letters*, 87(24), 2005.

[136] HX Yang, M Chshiev, B Dieny, JH Lee, Aurelien Manchon, and KH Shin. First-principles investigation of the very large perpendicular magnetic anisotropy at fe— mgo and co— mgo interfaces. *Physical Review B—Condensed Matter and Materials Physics*, 84(5):054401, 2011.

[137] S Yakata, H Kubota, Y Suzuki, K Yakushiji, A Fukushima, S Yuasa, and K Ando. Influence of perpendicular magnetic anisotropy on spin-transfer switching current in cofeb/ mgo/ cofeb magnetic tunnel junctions. *Journal of Applied Physics*, 105(7), 2009.

[138] Lavinia Elena Nistor, Bernard Rodmacq, Clarisse Ducruet, Céline Portemont, I Lucian Prejbeanu, and Bernard Dieny. Correlation between perpendicular anisotropy and magnetoresistance in magnetic tunnel junctions. *IEEE Transactions on Magnetics*, 46(6):1412–1415, 2010.

[139] Anabil Gayen, Gobinda Kumar Prasad, Srijani Mallik, Subhankar Bedanta, and Alagarsamy Perumal. Effects of composition, thickness and temperature on the magnetic properties of amorphous cofeb thin films. *Journal of Alloys and Compounds*, 694:823–832, 2017.

[140] M Kodzuka, T Ohkubo, K Hono, S Ikeda, HD Gan, and H Ohno. Effects of boron composition on tunneling magnetoresistance ratio and microstructure of cofeb/mgo/cofeb pseudo-spin-valve magnetic tunnel junctions. *Journal of Applied Physics*, 111(4), 2012.

[141] Mustafa Akyol. Origin of interfacial magnetic anisotropy in ta/cofeb/mgo and pt/cofeb/mgo multilayer thin film stacks. *Journal of Superconductivity and Novel Magnetism*, 32(3):457–462, 2019.

[142] K Watanabe, B Jinnai, S Fukami, H Sato, and H Ohno. Shape anisotropy revisited in single-digit nanometer magnetic tunnel junctions. *Nature communications*, 9(1):663, 2018.

[143] Nicolas Perrissin, Steven Lequeux, Nikita Strelkov, Antoine Chavent, Laurent Vila, Liliana D Buda-Prejbeanu, Stéphane Auffret, Ricardo C Sousa, Ioan L Prejbeanu, and Bernard Dieny. A highly thermally stable sub-20 nm magnetic random-access memory based on perpendicular shape anisotropy. *Nanoscale*, 10(25):12187–12195, 2018.

[144] Zhongchang Wang, Mitsuhiro Saito, Keith P McKenna, Shunsuke Fukami, Hideo Sato, Shoji Ikeda, Hideo Ohno, and Yuichi Ikuhara. Atomic-scale structure and local chemistry of cofeb–mgo magnetic tunnel junctions. *Nano letters*, 16(3):1530–1536, 2016.

[145] Jun Hayakawa, Shoji Ikeda, Young Min Lee, Fumihiro Matsukura, and Hideo Ohno. Effect of high annealing temperature on giant tunnel magnetoresistance ratio of cofeb/ mgo/ cofeb magnetic tunnel junctions. *Applied Physics Letters*, 89(23), 2006.

[146] H Almasi, D Reifsnyder Hickey, T Newhouse-Illige, M Xu, MR Rosales, S Nahar, JT Held, KA Mkhoyan, and WG Wang. Enhanced tunneling magnetoresistance and perpendicular magnetic anisotropy in

mo/cofeb/mgo magnetic tunnel junctions. *Applied Physics Letters*, 106(18), 2015.

[147] Kotaro Mizunuma, Michihiko Yamanouchi, Shoji Ikeda, Hideo Sato, Hiroyuki Yamamoto, Hua-Dong Gan, Katsuya Miura, Jun Hayakawa, Fumihiro Matsukura, and Hideo Ohno. Pd layer thickness dependence of tunnel magnetoresistance properties in cofeb/mgo-based magnetic tunnel junctions with perpendicular anisotropy cofe/pd multilayers. *Applied physics express*, 4(2):023002, 2011.

[148] Yung-Hung Wang, Wei-Chuan Chen, Shan-Yi Yang, Kuei-Hung Shen, Chando Park, Ming-Jer Kao, and Ming-Jinn Tsai. Interfacial and annealing effects on magnetic properties of cofeb thin films. *Journal of applied physics*, 99(8), 2006.

[149] XD Xu, K Mukaiyama, S Kasai, T Ohkubo, and K Hono. Impact of boron diffusion at mgo grain boundaries on magneto-transport properties of mgo/cofeb/w magnetic tunnel junctions. *Acta Materialia*, 161:360–366, 2018.

[150] Junta Igarashi, Butsurin Jinnai, Kyota Watanabe, Takanobu Shinoda, Takuya Funatsu, Hideo Sato, Shunsuke Fukami, and Hideo Ohno. Single-nanometer cofeb/mgo magnetic tunnel junctions with high-retention and high-speed capabilities. *npj Spintronics*, 2(1):1, 2024.

[151] BS Tao, DL Li, ZH Yuan, HF Liu, SS Ali, JF Feng, HX Wei, XF Han, Y Liu, and et al Zhao, YG. Perpendicular magnetic anisotropy in ta— co40fe40b20— mgal2o4 structures and perpendicular cofeb— mgal2o4— cofeb magnetic tunnel junction. *Applied Physics Letters*, 105(10), 2014.

[152] Bingshan Tao, Dalai Li, Houfang Liu, Hongxiang Wei, Jia-Feng Feng, Shouguo Wang, and Xiufeng Han. Transport properties in sputtered cofeb/mgal 2 o 4/cofeb magnetic tunnel junctions. *IEEE Transactions on Magnetics*, 50(11):1–4, 2014.

[153] Pravin Khanal, Bowei Zhou, Magda Andrade, Christopher Mastrangelo, Ali Habiboglu, Arthur Enriquez, Daulton Fox, Kennedy Warrilow, and

Wei-Gang Wang. Enhanced magnetoresistance in perpendicular magnetic tunneling junctions with mgal2o4 barrier. *Journal of Magnetism and Magnetic Materials*, 563:169914, 2022.

[154] Hiroaki Sukegawa, Xiandong Xu, Mohamed Belmoubarik, Hwachol Lee, Shinya Kasai, and et al Hono, Kazuhiro. Giant tunnel magnetoresistance in polycrystalline magnetic tunnel junctions with highly textured mgal2o4 (001) based barriers. *Applied Physics Letters*, 112(2), 2018.

[155] Hiroaki Sukegawa, Yoshio Miura, Shingo Muramoto, Seiji Mitani, Tomohiko Niizeki, Tadakatsu Ohkubo, Kazutaka Abe, Masafumi Shirai, Koichiro Inomata, and Kazuhiro Hono. Enhanced tunnel magnetoresistance in a spinel oxide barrier with cation-site disorder. *Physical Review B—Condensed Matter and Materials Physics*, 86(18):184401, 2012.

[156] Hiroaki Sukegawa, Huixin Xiu, Tadakatsu Ohkubo, Takao Furubayashi, Tomohiko Niizeki, Wenhong Wang, Shinya Kasai, Seiji Mitani, Koichiro Inomata, and Kazuhiro Hono. Tunnel magnetoresistance with improved bias voltage dependence in lattice-matched fe/spinel mgal2o4/fe (001) junctions. *Applied Physics Letters*, 96(21), 2010.

[157] Susann Liedtke-Grüner, Christoph Grüner, Andriy Lotnyk, Jürgen W Gerlach, Michael Mensing, Philipp Schumacher, and Bernd Rauschenbach. Crystallinity and texture of molybdenum thin films obliquely deposited at room temperature. *Thin Solid Films*, 685:8–16, 2019.

[158] Jonathan J Bean, Mitsuhiro Saito, Shunsuke Fukami, Hideo Sato, Shoji Ikeda, Hideo Ohno, Yuichi Ikuhara, and Keith P McKenna. Atomic structure and electronic properties of mgo grain boundaries in tunnelling magnetoresistive devices. *Scientific reports*, 7(1):45594, 2017.

[159] Sanjay Mathur, Michael Veith, Thomas Ruegamer, Eva Hemmer, and Hao Shen. Chemical vapor deposition of mgal2o4 thin films using different mg- al alkoxides: role of precursor chemistry. *Chemistry of materials*, 16(7):1304–1312, 2004.

[160] Zhang Ruixian, Ho Hoang Huy, Takanori Shirokura, Pham Nam Hai, Quang Le, Brian York, Cherngye Hwang, Xiaoyong Liu, Michael Gri-

belyuk, and et al Xu, Xiaoyu. High spin hall angle in bisb topological insulator and perpendicularly magnetized cofeb/mgo multilayers with metallic interfacial layers. *Applied Physics Letters*, 124(7), 2024.

[161] Takanori Shirokura, Tuo Fan, Nguyen Huynh Duy Khang, Tsuyoshi Kondo, and Pham Nam Hai. Efficient spin current source using a half-heusler alloy topological semimetal with back end of line compatibility. *Scientific Reports*, 12(1):2426, 2022.

[162] Sho Kagami, Takanori Shirokura, and Pham Nam Hai. Effects of post-growth annealing in yptbi topological semimetal and co/pt perpendicular magnetization multilayers. *Japanese Journal of Applied Physics*, 63(2):02SP98, 2024.

[163] Min Liu, Zhang Ruixian, Quang Le, Brian York, Cherngye Hwang, Xiaoyong Liu, Michael Gribelyuk, Xiaoyu Xu, Son Le, and et al Maeda, Maki. Spin hall magnetic field sensing device using topological insulator. *Applied Physics Letters*, 125(24), 2024.

List of publications

Journal Publications

1. Zhang Ruixian, Sho Kagami, Daiki Ito, Quang Le, Brian York, Cherngye Hwang, Xiaoyong Liu, Son Le, Maki Maeda, Tuo Fan, Yu Tao, Hisashi Takano, Pham Nam Hai. Giant perpendicular magnetic anisotropy in Mo/Boron-rich CoFeB/$MgAl_2O_4$ structure, Applied Physics Letters, Vol. 127, pp. 232403, Dec. 2025.

2. Zhang Ruixian, Ho Hoang Huy, Takanori Shirokura, Pham Nam Hai, Quang Le, Brian York, Cherngye Hwang, Xiaoyong Liu, Michael Gribelyuk, Xiaoyu Xu, Son Le, Maki Maeda, Tuo Fan, Yu Tao, Hisashi Takano. High spin Hall angle in BiSb topological insulator and perpendicularly magnetized CoFeB/MgO multilayers with metallic interfacial layers, Applied Physics Letters, Vol. 124, pp. 072402, Feb. 2024.

Other Journal Publications

1. Sho Kagami, Reo Yamamoto, Zhang Ruixian, Ken Ishida, Quang Le, Brian York, Cherngye Hwang, Xiaoyong Liu, Son Le, Maki Maeda, Tuo Fan, Yu Tao, Hisashi Takano, Pham Nam Hai. Realization of perpendicular magnetic anisotropy and high spin Hall angle in topological semimetal YPtBi/Ta/CoFeB junctions, Japanese Journal of Applied Physics, vol. 64, pp. 12SP07, Dec. 2025.

2. Min Liu, Zhang Ruixian, Quang Le, Brian York, Cherngye Hwang, Xiaoyong Liu, Xiaoyu Xu, Son Le, Maki Maeda, Tuo Fan, Yu Tao, Hisashi Takano, Pham Nam Hai. Comparison of spin Hall angles measured by spin accumulation, spin–orbit torque, and spin Hall magnetoresistance, Japanese Journal of Applied Physics, Vol. 64, pp. 103001, Oct. 2025.

3. Quang Le, Brian R. York, Cherngye Hwang, Xiaoyong Liu, Lei Xu, Son Le, Maki Maeda, Tuo Fan, Yu Tao, Hisashi Takano, Min Liu, Zhang Ruixian, Shota Namba, Pham Nam Hai. Thermal reliability and spin Hall angle of highly textured and epitaxial $Bi_{0.9}Sb_{0.1}$(012) topologi-

cal insulator, Japanese Journal of Applied Physics, Vol. 64, pp. 043001, Apr. 2025.

4. Quang Le, Xiaoyong Liu, Lei Xu, Brian R. York, Cherngye Hwang, Son Le, Maki Maeda, Tuo Fan, Yu Tao, Hisashi Takano, Min Liu, Zhang Ruixian, Shota Namba, Pham Nam Hai. Effects of metal, oxide, and hybrid metal-oxide interlayers on spin–orbit torque in BiSb topological insulator and magnetic interfaces, Journal of Applied Physics, AIP Publishing, Vol. 137, pp. 123903, Mar. 2025.

5. Min Liu, Zhang Ruixian, Quang Le, Brian York, Cherngye Hwang, Xiaoyong Liu, Michael Gribelyuk, Xiaoyu Xu, Son Le, Maki Maeda, Tuo Fan, Yu Tao, Hisashi Takano, Pham Nam Hai. Spin Hall magnetic field sensing device using topological insulator, Applied Physics Letters, Vol. 125, pp. 242401, Dec. 2024.

6. Quang Le, Brian R. York, Cherngye Hwang, Xiaoyong Liu, Michael A. Gribelyuk, Son Le, Lei Xu, Jason James, Jose Ortega, Maki Maeda, Tuo Fan, Hisashi Takano, Min Liu, Zhang Ruixian, Shota Namba, Pham Nam Hai. Transport and material properties of doped BiSbX topological insulator films grown by physical vapor deposition, Japanese Journal of Applied Physics, Vol. 63, pp. 123001, Dec. 2024.

7. Ho Hoang Huy, Zhang Ruixian, Takanori Shirokura, Shigeki Takahashi, Yoshiyuki Hirayama, Pham Nam Hai. Integration of BiSb Topological Insulator and CoFeB/MgO With Perpendicular Magnetic Anisotropy Using an Oxide Interfacial Layer for Ultralow Power SOT-MRAM Cache Memory, IEEE Transactions on Magnetics, Vol. 59, No. 11, pp. 3400905, May 2023.

International Conference (Reviewed)

1. Zhang Ruixian, Quang Le, XiaoYong Liu, Lei Xu, Brian R.York, Cherngye Hwang, Son Le, Maki Maeda, Tuo Fan, Yu Tao, Hisashi Takano, Min Liu, Shota Namba, Pham Nam Hai. Impact of Metal, Oxide, and Hybrid Metal-Oxide Interlayers on Spin Hall Effect in BiSb Topological Insulator

and Magnetic Interfaces, The Magnetic Recording Conference (TMRC 2025), Aug. 2025.

2. Z. Ruixian, H. H. Huy, Q. Le, B. York, C. Hwang, X. Liu, M. Gribelyuk, X. Xu, S. Le, M. Maeda, F. Tuo, Y. Tao, H. Takano, T. Shirokura, P. N. Hai. High spin Hall angle in heterostructures of BiSb topological insulator and perpendicularly magnetized CoFeB/MgO multilayers with metallic interfacial layers, The 22nd International Conference on Magnetism (ICM2024), June 2024.

3. Zhang Ruixian, Takanori Shirokura, Tuo Fan, Pham Nam Hai. Fabrication and evaluation of fully sputtered topological insulator/perpendicularly magnetized CoFeB/MgO multilayers for SOT-MRAM application, Intermag 2023, May 2023.

Other International Conference (Reviewed)

1. Sho Kagami, Reo Yamamoto, Zhang Ruixian, Ken Ishida, Quang Le, Brian York, Cherngye Hwang, Xiaoyong Liu, Son Le, Maki Maeda, Tuo Fan, Yu Tao, Hisashi Takano, Pham Nam Hai. Fabrication and Evaluation of Topological Semimetal YPtBi/Ta/CoFeB Junctions with High Spin Hall Angle for SOT-MRAM, SSDM 2025, Sept. 2025.

2. M. Liu, R. Zhang, Q. Le, B. York, C. Hwang, X. Liu, M. Gribelyuk, X. Xu, S. Le, M. Maeda, F. Tuo, Y. Tao, H. Takano, P. N. Hai. Spin Hall sensor using topological insulator, International Conference of Asian Union of Magnetics Societies (IcAUMS 2025), Feb. 2025.

3. F. Tuo, Q. Le, B. R. York, C. Hwang, X. Liu, M. A. Gribelyuk, S. Le, L. Xu, J. James, J. Ortega, M. Maeda, Y. Tao, H. Takano, M. Liu, R. Zhang, S. Namba, P. N. Hai. Doped BiSbX Topological Insulator For Spin-Orbit Torque Devices, International Conference of Asian Union of Magnetics Societies (IcAUMS 2025), Feb. 2025.

4. Y. Hu, K. Sato, R. Zhang, K. Ishida, P. N. Hai. Growth of Co thin Films with Low Roughness by ALD for 3D Magnetic Memory, International

Conference of Asian Union of Magnetics Societies (IcAUMS 2025), Feb. 2025.

5. Ho Hoang Huy, Zhang Ruixian, Takanori Shirokura, Shigeki Takahashi, Yoshiyuki Hirayama, Pham Nam Hai. Large spin Hall effect in BiSb topological insulator/CrO_x/CoFeB/MgO with perpendicular magnetic anisotropy for ultralow power SOT-MRAM, The 8th International Conference on Applied & Engineering Physics (CAEP-8), Oct. 2023.

6. Ho Hoang Huy, Zhang Ruixian, Takanori Shirokura, Shigeki Takahashi, Yoshiyuki Hirayama, Pham Nam Hai. Integration of BiSb topological insulator and CoFeB/MgO with perpendicular magnetic anisotropy using an oxide interfacial layer for ultralow power spin-orbit torque magnetic memory, Intermag 2023, May 2023.

Domestic Conference (Not reviewed)

1. Ruixian Zhang, Quang Le, Xiaoyong Liu, Lei Xu, Brian R. York, Cherngye Hwang, Son Le, Maki Maeda, Fan Tuo, Hisashi Takano, Min Liu, Shota Namba, Pham Nam Hai. Study of Metal, Oxide, and Hybrid Metal-Oxide Interlayers for optimizing Spin-Orbit torque in BiSb Topological Insulator and Magnetic Interfaces, The 72nd JSAP Spring meeting 2025, Mar. 2025.

2. Ruixian Zhang, Ho Hoang Huy, Takanori Shirokura, Pham Nam Hai, Quang Le, Brian R. York, Cherngye Hwang, Xiaoyong Liu, Xiaoyu Xu, Son Le, Michael Gribelyuk, Hisashi Takano, Maki Maeda, Fan Tuo, Yu Tao. High spin Hall angle in BiSb topological insulator and perpendicularly magnetized CoFeB/MgO multilayers with metallic interfacial layers, The 71th JSAP Spring Meeting 2024, Mar. 2024.

3. Ruixian Zhang, Shirokura Takanori, Tuo Fan, Pham Nam Hai. Fabrication and evaluation of BiSb topological insulator / perpendicular magnetization CoFeB multilayer film for SOT-MRAM application, 83rd JSAP Autumn meeting, Sept. 2022.

Other Domestic Conference (Not reviewed)

1. Min Liu, Ruixian Zhang, Quang Le, Brian York, Cherngye Hwang, Xiaoyong Liu, Michael Gribelyuk, Xiaoyu Xu, Son Le, Maki Maeda, Tuo Fan, Yu Tao, Hisashi Takano, Pham Nam Hai. High performance spin Hall sensing device using BiSb topological insulator, The 72nd JSAP Spring meeting 2025, Mar. 2025.

2. Ho Hoang Huy, R. Zhang, T. Shirokura, S. Takahashi, Y. Hirayama, Pham Nam Hai. Integration of BiSb topological insulator and CoFeB/MgO with perpendicular magnetic anisotropy using an oxide interfacial layer for ultralow power SOT-MRAM cache memory, 84th JSAP Autumn meeting, Sept. 2023.

Acknowledgement

During five years in Japan, I have received tremendous love and support from everyone around me. I want to dedicate this part to acknowledge the support I have received.

- First, I would like to express my deep gratitude towards my academic advisor-Prof. Pham Nam Hai. What you have done to me inside and outside of research is difficult to express by words. I have been learning from you not only how to do research but also the way of thinking and experience. Thanks to your dedicated guidance, truth and the opportunities you have been awarding me, I could earn the full scholarships to pursuit my studies, and obtain fundings. I still remember vividly every time you discussing each experiment, paper, or conference report with you. You always guide my thinking, clarifying the details of my next steps with unparalleled and incredibly approachable leadership. This kind of guidance, both verbal and intangible, is like a torch I will cherish and carry with me throughout my life. Thank you from the bottom of my heart with best regards.

- I would like to thank Dr. Nguyen Huynh Duy Khang, Dr. Shirokura, Dr. Tuo Fan, Mr. Sasaki who helped me so much with the intial training. Your guidance is precious to me so that I could catch up with the research within shortest time. It is also grateful to share and dicuss with you anything from research, career to daily life in Japan.

- I would like to thank Dr. Ho Hoang Huy, Mr. Kagami, Ms. Liu, Mr. Hu, Ito-san, Mr.Namba, Sato-san, Hujie-san, Tsureo-san who helped me so much with the collaborative research projects. Thank you for your hard work in ensuring the project's steady progress, allowing me to experience and participate in solving more interesting problems. We encouraged each other, discussed the topics seriously, and created many pleasant memories.

- I would like to thank all former and current members Pham Lab for your support and effort. The facilities and techniques I have used today are the collective contribution from all of you.

- I would like to thank Mr. Quang, Mr. Son, Mr. Cherngye Hwang, Mr. Brian York, Mr. Xiaoyong Liu, Mr. Michael Gribelyuk, Dr. Tuo Fan and Ms. Xiaoyu Xu, Ms. Maeda, Mr. Michael Ho, Mr. Hisashi Takano, Mr. Tao at Western Digital for your collaboration and fruitful discussion on the SOT MRAM technology. Our research could not reach this far without your effort.

- I would like to thank SPRING (previously known as Cross the border! Tokyo-Tech pioneering doctoral research project) from Tokyo Tech, and WISE-SSS program for their financial support during my studies.

- I would like to thank Mr. Iida Yu at Materials Analysis Division Open Facility Center for your training and advice on X-ray tools. I also acknowledge Nakagawa Lab for the support from SQUID and XRD measurements.

- I would like to thank Goertek Japan company who provide me chance to have a constructive internship.

Finally, I feel truly grateful to always have my family stay by my side. Thank you for taking good care of yourselves. The greatest gift to me is that you are healthy. Many things have changed since the day I left China and there are some I could not meet again. I guess at somewhere, you feel happy for me and I am always happy with the time we spent together. And thank my little family for taking good care of me, especially for your unwavering support in helping me complete my doctoral degree.

Japan, Tokyo, February 9, 2026
Author
Zhang Ruixian